Fresh Mix Properties and Flexural Analysis with Digital Image Correlation of Additively Manufactured Cementitious Materials

Morgan C. Jenkins

Thesis submitted to the faculty of the Virginia Polytechnic Institute and State University in partial fulfillment of the requirements for the degree of

Master of Science
In
Civil Engineering

Alexander S. Brand, Chair
Matthew R. Eatherton
Maryam Shakiba

December 18, 2019
Blacksburg, VA

Keywords: additive manufacturing, material extrusion, 3DCP, concrete, mortar, cementitious materials, rheology, fresh mix, flexure, three-point bending, anisotropy, anisotropic

Fresh Mix Properties and Flexural Analysis with Digital Image Correlation of Additively Manufactured Cementitious Materials

Morgan C. Jenkins

ACADEMIC ABSTRACT

Recently, additive manufacturing (AM), or "3D printing," is expanding into civil infrastructure applications, particularly cementitious materials. To ensure the safety, health, and welfare of the public, quality assurance and quality control (QA/QC) methods via standardized testing procedures are of the upmost importance. However, QA/QC methods for these applications have yet to be established. This thesis aims to implement existing ASTM standards to characterize additive manufactured cementitious composites and to gather better information on how to tackle the challenges that are inherent when printing with cementitious materials. In this work, fresh mix properties and hardened concrete properties were investigated using current ASTM standards as a starting point for applying or adapting them for AM applications.

Specifically, this project applied existing ASTM standards for fresh mix mortars to measure setting time, flow, and early compressive strength as qualitative indicators of printability, pumpability, and buildability. The fresh mix properties were investigated for 12 different mortar mixes to demonstrate the effect that moisture content, absorption, and sand type can have on these fresh mix properties. The results for setting time and compressive strength demonstrated that there was less variability in the properties when the moisture condition of the aggregate was measured and accounted. Flow was shown to be strongly influenced by the sand type.

Additively manufactured mortars were used to print a box in a layer-by-layer process. To evaluate the effect of layering on the flexural strength, three-point bending tests were implemented using four different loading orientations to explore the anisotropic mechanical properties. The observed anisotropic behavior was corroborated with stereo-digital image correlation data showing the stress-strain and load-deflection relationships. Two orientations (A and B) demonstrated brittle behavior while the other two orientations (C and D) experienced quasi-brittle behavior. In addition, setting a minimum unit weight of 132 pcf enabled an analysis of the effect that defects had on the mechanical performance: specimens greater than 132 pcf demonstrated greater and less variable strengths than the specimens less than 132 pcf. The discussion of how defects impacted performance of the different orientations can be valuable when determining how to effectively model, design, and inspect 3D printed structures in the future.

The findings of this thesis confirm that existing ASTM standards for mortars can be modified and applied to AM cementitious composites for QA/QC. It is recommended that mixtures used in 3D printing of cementitious composites should design and accommodate the moisture condition of the aggregate to optimize the predictability of the fresh and early-age properties. For the hardened properties, it is recommended that testing procedures such as flexural testing account for anisotropic behavior. Furthermore, for implementation of 3D printed concrete structures, it is highly recommended that design is a function of loading orientation due to the anisotropic properties of the composite.

Fresh Mix Properties and Flexural Analysis with Digital Image Correlation of Additively Manufactured Cementitious Materials

Morgan C. Jenkins

GENERAL AUDIENCE ABSTRACT

Recently, additive manufacturing (AM), or "3D printing," is expanding into civil infrastructure applications, specifically cementitious materials such as mortar and concrete. Understanding and predicting the behavior of the materials when using this new technique is vital for quality assurance and quality control (QA/QC). However, standard test methods have yet to be established for this new construction technique. This thesis aims to use existing testing standards to characterize AM cementitious composites and to gather better information on how to tackle the challenges of printing with these materials. In this work, properties before and after the materials hardened were studied by adapting current testing standards.

Specifically, this project applied existing testing standards for fresh mix mortars to measure setting time, flow, and early compressive strength. These properties can serve as indicators of specific printing requirements. The fresh mix properties were studied for 12 different mortar mixes to show the effect of moisture content, absorption, and sand type. The results suggest that there was less variability in the properties when the moisture condition and type of the aggregate was accounted. The fresh mix materials were printed in a layer-by-layer process and then hardened in place. The effects of the layers were explored by performing flexure tests using four orientations with respect to how the load was applied to the layers. The observed difference in behavior for the different orientations was supported by digital image correlation data. In addition, an analysis of the effect defects had on the performance was included. Understanding how defects impacted performance can be valuable for effectively designing 3D printed structures in the future.

The results of this thesis confirm that existing testing standards for mortars can be adapted and applied to AM cementitious materials for QA/QC. It is recommended that mixtures used in 3D printing of cementitious materials should account for the moisture condition of the aggregate to improve the predictability of the fresh and early-age properties. For the hardened properties, it is recommended that the design is a function of loading orientation due to the difference in behavior for the different orientations of the material.

Acknowledgements

A special thanks to my committee chair, Dr. Alexander Brand, for his support, encouragement, and mentorship throughout my research experience and graduate studies at Virginia Tech. In addition, thanks to Dr. Matthew Eatherton and Dr. Maryam Shakiba for serving on my thesis committee.

I extend my gratitude to the rest of the faculty, staff, and my peers at Virginia Tech who played a role in helping me during this project. Thank you to David Mokarem and Brett Farmer for making the structures lab an enjoyable place to work and for their technical assistance. Thank you to Samuel Sherry for his patience and help with the digital image correlation system and software.

I would like to acknowledge the Institute for Advanced Composites Manufacturing Innovation (IACMI) summer internship program and Oak Ridge National Laboratory (ORNL) for the opportunity to learn about additive manufacturing at the Manufacturing Demonstration Facility. I would like to thank Dr. Brian Post and Dr. Yann Le Pape for their mentorship, and Debalina Ghosh for her collaboration on the preliminary flexural strength measurements.

Above all, I want to thank my mother and father who have been my examples of how to strive for excellence and a source of constant encouragement.

Contents

Abbreviations

- **3DCP** – 3D concrete printing
- **AD** – air dried
- **AM** – additive manufacturing
- **ASTM** – American Society for Testing and Materials
- **BAAM –** big area additive manufacturing
- **BFS –** blast furnace slag
- **C3DP –** construction 3D printing
- **DIC** – digital image correlation
- **FRC** – fiber reinforced concrete
- **FRP** – fiber reinforced polymer
- **GGBFS** – ground granulated blast furnace slag
- **LSAM** – large scale additive manufacturing
- **MDF** – manufacturing demonstration facility
- **OD** – oven dried
- **ORNL** – Oak Ridge National Laboratory
- **RH** – relative humidity
- **s/c –** sand to cement
- **SCC –** self-consolidating concrete
- **SCM** – supplementary cementitious material
- **SkyBAAM –** Sky big area additive manufacturing
- **SSD –** saturated surface dry

- **STL –** stereolithography
- **TPBT –** three-point bending test
- **UTK –** University of Tennessee, Knoxville
- **QA/QC** – quality assurance and quality control
- **VT** – Virginia Tech
- **w/c –** water to cement

1. INTRODUCTION

This chapter provides the objective and scope of the testing and analysis performed and the general organization of this thesis.

1.1. Objectives and scope

Within the last decade additive manufacturing (AM) has started to expand its applications to include construction materials such as cementitious materials, metals, and composites. Within the context of civil engineering, AM with cementitious materials is a step towards automating the construction process. Since AM, or "3D printing" as it is commonly called, with cementitious materials is in the initial stages of research and development, there is a strong need for quality assurance and quality control (QA/QC) via standard test methods for both the fresh mix properties and the mechanical properties of the hardened material. However, QA/QC methods for these applications have yet to be established. The objective of this project was to determine whether existing ASTM test methods could be applied to the fresh mix cementitious materials as well as mechanical testing to determine the hardened properties.

Currently, using AM techniques in the context of civil engineering involves printing structures without much knowledge of the long-term durability, structural design, or structural capacity; indeed, many projects appear to have a focus on demonstrability only. Therefore, implementing standard test methods would ensure the safety, capacity, and durability of the 3D-printed structures while allowing the civil engineering field to take full advantage of what AM can offer the industry. Advantages to using AM in construction include reducing waste and cost of formwork, reducing manual labor and the risk of worksite injuries, decreasing build time, and potentially reducing construction errors. Alternatively, there are existing challenges of using AM,

which include contrasting requirements for the fresh mix material performance, undefined testing standards for quality control of a printed structure, potentially weakened mechanical properties due to layer interface bond, and more as discussed further within this work.

This thesis aims to better implement existing ASTM standards to characterize 3D concrete printing (3DCP) and to gather better information on how to tackle these challenges. In this work, fresh mix properties and hardened concrete properties were investigated using current ASTM standards as a starting point for applying or adapting them for AM applications.

The fresh mix properties were investigated using flow, setting time, and early compressive strength tests. These were investigated using 12 different mortar mixes to demonstrate the effect that moisture content, absorption, and sand type can have on these fresh mix properties. Controlling and predicting fresh mix properties is very important for 3D printing with cementitious materials, so that the mix design can consistently achieve the specific requirements needed.

The hardened properties of 3D printed specimens were also investigated by saw-cutting beams from 3D printed parts created by researchers at Oak Ridge National Laboratory (ORNL). The beams were tested in flexure using a center-point loading setup in different orientations to explore the anisotropic behavior of the cementitious materials. Preliminary tests using two different beam orientations were performed at the University of Tennessee, Knoxville, which is near the ORNL facilities. Further flexure tests were performed using a total of four beam orientations at Virginia Polytechnic Institute and State University.

Stereo-digital image correlation was used during the flexure tests to measure strains and displacements. Those results were used to compare the stress-strain relationships of the four different orientations. The stress-strain relationships can be very important for assessing potential for sudden, brittle failures, especially since inclusion of tensile reinforcement in 3D printed

concrete is a challenge that needs to be addressed as well. Some of the specimens also had noticeable defects induced by the printing process, so an analysis of the effect defects had on the mechanical performance was included. This is also important because the printing process can induce voids and defects which could reduce the capacity of the structure. The discussion of how defects impacted performance of the different orientations can be valuable when determining how to effectively model, design, and inspect 3D printed structures in the future.

1.2. Organization of the thesis

This thesis discusses the applicability of current ASTM test methods for mortars and concretes to fresh mix properties and hardened material properties for 3D printing with cementitious materials. The organization of the thesis is detailed as follows:

Chapter 2 introduces the concepts of additive manufacturing, additive manufacturing within civil engineering, the associated challenges of applying AM techniques to cementitious materials, and other topics related to the fresh mix and hardened properties of cementitious materials for AM applications.

Chapter 3 covers Phase I of this project which involved discussion on the Sky Big Area Additive Manufacturing (SkyBAAM) system used to print the specimens at ORNL. The mix design developed at ORNL for printing with SkyBAAM is discussed in materials and mix design section. Specimen preparation is then detailed prior to outlining the test method for flexural testing using two different orientations, results, and conclusions from these preliminary tests.

Chapter 4 covers Phase II of this project. The flexural test procedure was revised based on the tests from Phase I, and two additional orientations were added to further explore the potential for anisotropic behavior. Strains and displacements were measured using digital image correlation

system. The stress-strain relationship for the different orientations were compared. The effect of defects was discussed in this chapter as well.

Chapters 5 summarizes the information from Phase I and Phase II to make comparisons, discuss the results of both phases, and summarize conclusions. Chapter 6 expands on that by making final recommendations and discussing the direction of future work. The attached appendices include photos and relevant information to the flexural testing performed in Phases I and II.

2. LITERATURE REVIEW

2.1. Additive manufacturing introduction

Within the manufacturing industry there are general categories in which almost every existing manufacturing process falls into. These include: casting, molding, forming, machining, joining, additive manufacturing, etc. Additive manufacturing (AM), also commonly referred to as "3D printing," is a process that has become increasingly common within the last several decades. Significant progress has been made in AM with materials such as metals, polymers, and composites, although cementitious materials have also been gaining popularity. Due to the increasing interest in AM, it has become clear that specific terminology is essential to effectively communicate about the concepts and new ideas related to this manufacturing process.

Due to lack of proper and consistent descriptive language preventing effective communication, ASTM International has published standards for additive manufacturing that define specific terminology to guide and aid the discussion of AM with different materials and processes. The first attempt, ASTM F2792 – 12a [1], was withdrawn in 2015 and defined seven general AM processes: binder jetting, directed energy deposition, material extrusion, material jetting, powder bed fusion, sheet lamination, and vat photopolymerization. ASTM International expanded and refined the language used to describe AM processes within ISO/ASTM 52900 [2], which was adopted in 2015. ISO/ASTM 52900 expanded the general terminology used to include terms related to general AM language, process categories (as previously described in ASTM F2792), general processing, data processing, material processing, applications, and properties. This terminology was meant to be applicable to all materials, including cementitious materials. This work will discuss the role of AM in the context of civil engineering and construction, specifically with cementitious materials using extrusion AM processes.

2.2. AM with cementitious materials

There have been a wide variety of names used for this developing technology such as digital concrete, 3D concrete printing (3DCP), construction 3D printing (C3DP), large scale additive manufacturing (LSAM), contour crafting, and more (e.g., [3–10]). Moreover, there have been a wide variety of approaches through the system development and printing parameters involved for each project based on the AM process selected. For example, material extrusion and binder jetting (also known as particle bed fusion) are two of the AM processes used for 3DCP. The difference between which process is used can change what parameters need to be considered during QA/QC. However, material extrusion processes have been the most common AM approach for 3DCP.

2.2.1. Brief history and developments

Buswell et al. [5] details a "roadmap" for the progression of AM using cementitious materials. The research thus far has been largely focused on demonstrability of product production. Figure 2.1 shows a timeline of the increasing interest and involvement in AM with cementitious materials over the past two decades. Figure 2.1 suggests that the number of projects is increasing at an exponential rate.

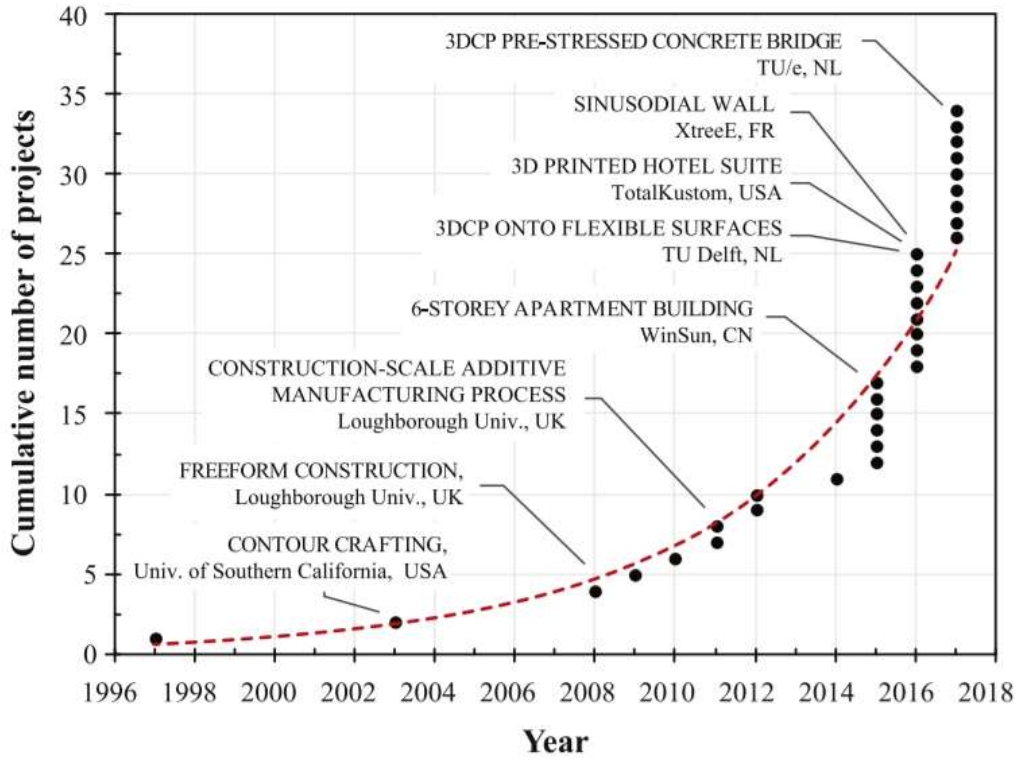

Figure 2.1: Timeline of the increasing projects related to AM with cementitious materials since 1997. From Buswell et al. [5]

Detailed below are a few examples of early development of AM applied to construction with cementitious materials:

- The introduction of applying additive manufacturing to construction applications came from Joseph Penga at Rensselaer Polytechnic Institute in 1997 exploring solid freeform construction [11]. Solid freeform construction in this context involved deposition of sand and then cement followed by application of binder and steam.
- Contour Crafting, a concept devised at the University of Southern California (USC) around 1999 by Behrokh Khoshnevis, capitalized on computer aided design and computer aided manufacturing [12, 13]. In the beginning of its development, ceramics and clays were used. Through continued research since 1999, the concept was physically developed and refined.

- Freeform Construction, developed by researchers at Loughborough University, used a robot and crane system and included Ultra High Performance Concrete yielding high material properties for use in more complex AM structures [14–16].

The first three main pioneers for AM with cementitious material discussed dominated the initial research, and then around 2008, the number of groups involved in this research began to rapidly rise (Figure 2.1). Now there are many groups developing their own AM robots and systems (*e.g.*, ETH Zurich, Eindhoven University of Technology, National Institute of Standards and Technology, Oak Ridge National Laboratory, Tongji University). Since there is a large focus on demonstrability, many companies are now printing large-scale structures; however, there is little knowledge on the structural capacity, design, and durability. Several examples are included of examples of recent demonstrations of large scale 3DCP (Figure 2.2 to Figure 2.3).

f) vertically printed, in-situ walls and columns.
Image: courtesy of Andrey Rudenko, Total Kustom, USA

Figure 2.2: 3D printed concrete walls and columns (from Buswell et al. [5], original source in photo description)

As mentioned in Lim et al. [8], 3DCP is a material extrusion AM technique using mortars. An example of a part that can be 3D printed is shown in Figure 2.3.

Figure 2.3: Example of Concrete Printing (from Lim et al. [8])

Unlike material extrusion, there is the D-Shape process which is a binder jetting process. This can create complex structures such as the architectural piece, “Radiolaria,” as seen in Figure 2.4 [8].

Figure 2.4: Example of D-Shape (from Lim et al. [8])

It is important to note a limitation of this literature review as a whole: the literature regarding 3DCP is being published at an apparent exponential rate (Figure 2.1) and the technology is still new. Any literature review on this topic becomes outdated almost as soon as it is published. This limitation highlights an important gap in the research that is vital for moving forward: there is not a common source database that compiles all the recent data and testing methods. This need is reinforced in subsequent sections of this work. Compiling the data is essential for understanding what testing methods are being employed by researchers and analyzing the data. This would make comparing raw data and test results for 3DCP easier for all researchers and could inform future testing standards.

2.2.2. Sustainability

Since concrete is the most widely used construction material by volume in the world [17] – with an estimated 4 billion tons and 28 billion tons of portland cement and concrete, respectively, produced worldwide every year – reducing the waste produced during the construction process is important, both economically and environmentally, and is a benefit of 3DCP. All manufacturing processes create a finished product as well as scraps and waste, including additive manufacturing;

however, AM can minimize waste in a few ways. Regardless of the AM process employed for cementitious materials, a commonality between them all is that they are free of formwork throughout the process [18]. Plywood formwork used for traditionally cast concrete has a short service life and can only be reused a handful of times before it is disposed.

In addition, portland cement production accounts for around 5 to 8 percent of global carbon dioxide emissions [19, 20]. Some research suggests that 3DCP has potential to reduce carbon dioxide emissions by reducing cement consumption and utilizing supplementary cementitious materials (SCMs) within the highly specialized mix designs [21]. Chen et al. [22] investigated 3DCP comprehensively as a potential low carbon dioxide approach but notes that the literature is limited and thus not conclusive. There is little literature available regarding the life-cycle analysis comparison between traditionally cast concrete versus 3DCP; this comparison is needed in order to assess the viability of 3DCP in the future.

2.3. Challenges of AM with cementitious materials

Although there is increasing interest in this research topic, there is little consistency between AM systems, mix designs, test methods, documentation, etc. Documenting the processes, materials, test methods, etc. from past, present, and future research can inform the continued development of AM with cementitious materials by helping solve the current challenges.

Reviews of the state-of-the-art research and literature are being compiled and published yearly [4–6, 18, 21, 23–36], and this literature outlines some of the challenges encountered while working with cementitious materials for AM. A major hurdle for comparing results between different research groups stems from the wide variety of parameters for each AM system. For example, parameters that could drastically vary and alter the results include the AM process used

(e.g., extrusion, binder jetting), the type of extrusion method (e.g. using vibration or not), rate of extrusion, nozzle size and shape, curing method, concrete mix design, variability in raw materials from mix design, etc. Even if all involved parameters were held constant, there are still challenges for AM with cementitious materials as shown in Figure 2.5. These challenges relate to the fresh mix concrete properties, hardened concrete properties, and geometric tolerances between the computer and physical models [5]. In addition, no testing standards currently exist to specify quality assurance or quality control procedures for measuring those properties.

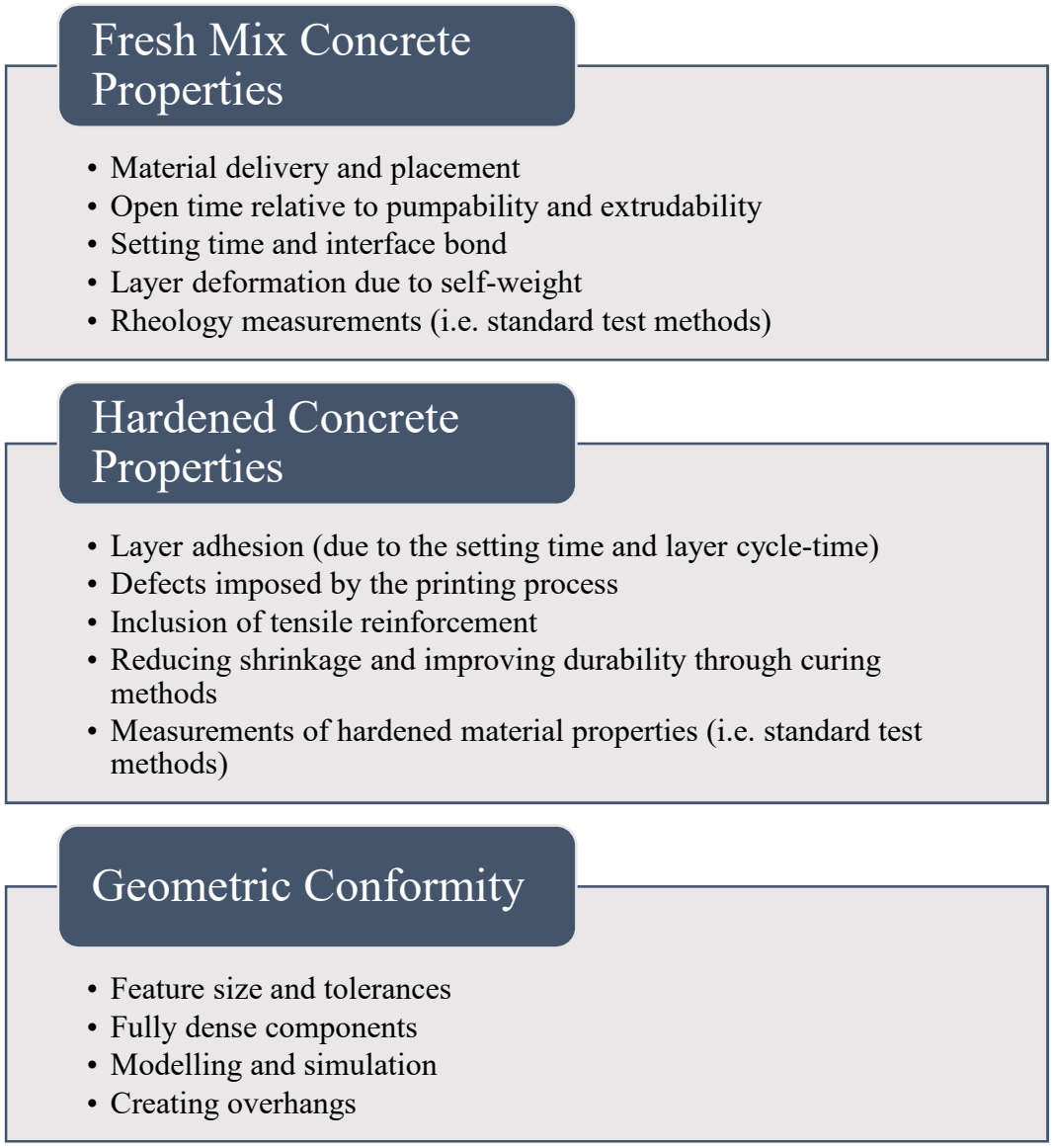

Figure 2.5: Summary of 3DCP challenges. Summarized from [5, 6, 18].

Some of the challenges presented in Figure 2.5 stem from contrasting requirements of the mix design: the fresh mix material must be fluid enough to be extruded from a nozzle, yet viscous or stiff enough to hold its shape once cast. The solutions presented must satisfy *both* requirements to be successful. Other material properties separate cementitious materials from other popular additive manufacturing materials like polymers and metals; cement undergoes an exothermic chemical reaction during the hydration process and requires proper curing to reach full

compressive strength. Furthermore, concrete is a quasi-brittle material that is weak in tension, which presents the question of how to integrate tensile reinforcement in printed parts. Figure 2.6 depicts the progression of AM material design from raw materials all the way to structural performance while addressing the sequence of aforementioned challenges along the way.

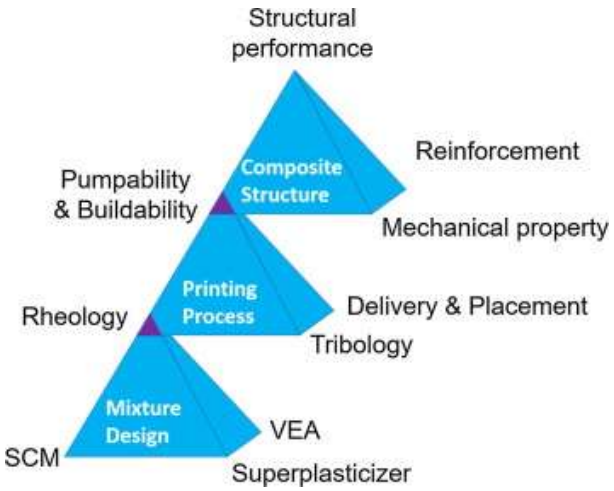

Figure 2.6: Multi-level approach to 3DCP material design. From Lu et al. [30]

2.3.1. Fresh mix concrete properties

The first challenge to address is achieving a concrete mix design that meets all the specific requirements listed under "Fresh Mix Concrete Properties" in Figure 2.5. Material delivery and placement partly refer to the seven different AM processes discussed in Section 2.1. Two typical processes for AM with cementitious materials are binder jetting and material extrusion [18]. However, the most common process of AM with cementitious materials surveyed is material extrusion, which is defined by ISO/ASTM 52900 [2] as an AM process in which "material is selectively dispensed through a nozzle or orifice."

For the material extrusion AM process, another concern with material delivery and placement can be workability, extrudability, and buildability which are defined in [8, 16, 37] as:

i. **Pumpability** is being able to move through the AM deposition system without segregation of materials
    a. **Extrudability:** ability to be extruded through a nozzle to form a continuous filament of material.
    b. **Workability:** the consistency of the concrete
ii. **Printability:** ability to deposit material in a continuous filament without tearing
iii. **Buildability:** ability to support subsequent layers without layer deformation

The fresh mix material properties for extrudability, workability, and buildability must balance between the contradicting requirements to find an open time zone. Open time for conventionally cast concrete is related to slump loss. However, for AM concrete, **open time** takes a broader definition as "the period where the above properties are consistent within acceptable tolerances." The overlap between the sections in Figure 2.7 provides the printable, pumpable, and buildable properties for a concrete mix for additive manufacturing based on the conclusions from Bentz et al. [37].

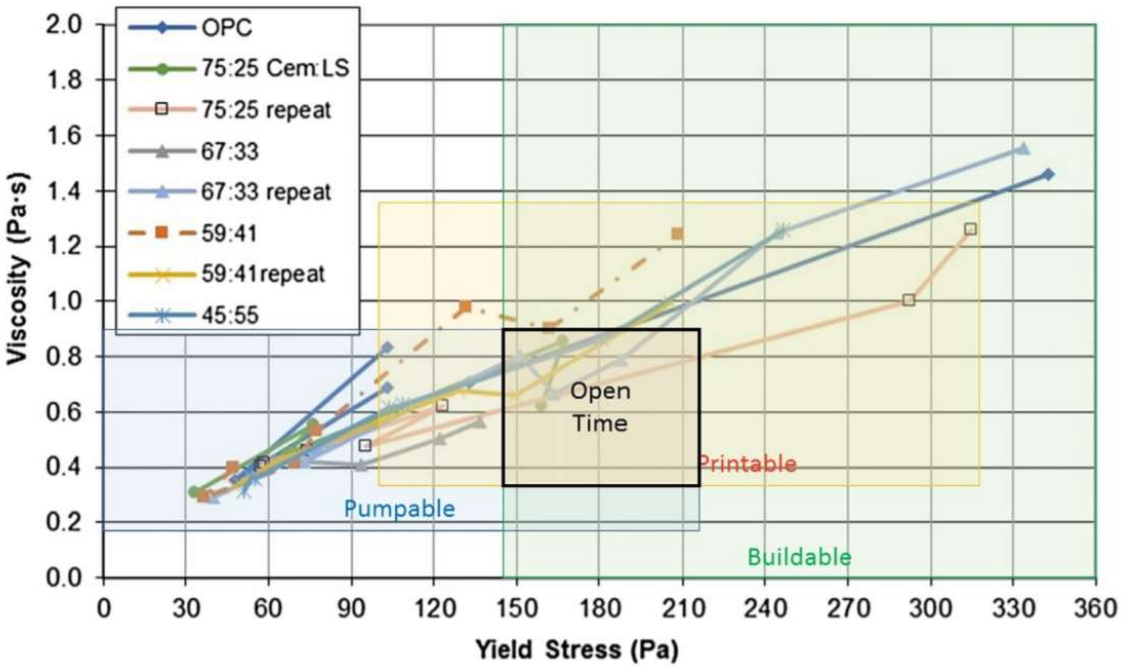

Figure 2.7: Graphical depiction of different fresh mix requirements relative to the ideal open time zone. (From Bentz et al. [37])

Another challenge of the fresh mix concrete properties is the setting time of the mix versus the cycle-time, or the total time elapsed between layers. The setting time and cycle-time affect the interface bond, or interlayer adhesion. If the setting time is much faster than the cycle-time, then the deposited layer of concrete will form a cold joint between the two layers and weaken the AM part or structure. Alternatively, if the cycle-time is much faster than the setting time, then it can cause layer deformation making structure potentially unstable.

Finally, the issue facing both the fresh mix properties and the hardened concrete properties is developing or adopting test methods that give useful data to implement quality control and quality assurance procedures. Understanding what test procedures can give representative and useful data in assessing AM cementitious structures is critical in progressing the research.

2.3.2. Hardened concrete properties

The second challenge to address after a mix design satisfies the fresh mix requirements is to consider the requirements listed under "Hardened Concrete Properties" in Figure 2.5. Recall that these challenges include layer interface bond; voids in filament and part geometry; implementation of tensile reinforcement; curing methods, shrinkage, and durability; and mechanical testing.

Several variables can affect the layer adhesion [5, 15, 38–40]. Specifically, the two parameters that affecting the interface bond the most are elapsed print time and material setting time. If the elapsed print time exceeds the setting time of the material by too long, then a cold joint could form. If the elapsed print time is much faster than the setting time of the material, the structure could have layer deformations or become unstable during the print. Therefore, the balance between these two properties is very important; the formation of cold joints can reduce the overall performance of the concrete. However, the effect of the cold joint could potentially be reduced as the concrete hydrates and strengthens.

Related to the issue of setting time and cold joints is being able to produce fully dense parts. AM concrete is more prone to voids and defects than traditionally cast concrete. The ability for the concrete to support subsequent layers requires a certain amount of stiffness from the material. This property is most readily achieved when the concrete is close to its initial setting time. Printing close to that initial set time can cause tearing in the filament and produce voids in the material. The AM part printed with a less-dense filament would thus be weaker than traditionally cast concrete that has a higher slump and is consolidated [5, 15, 21, 41].

Since concrete is a quasi-brittle material that is weak in tension, the implementation of tensile reinforcement is vital to the viability of AM concrete for large scale construction applications [5]. The printed structures and parts need to be able to withstand tensile stresses due

to various loads. Traditionally cast concrete is commonly reinforced with steel rebar; however, other tensile reinforcement can be employed such as steel-concrete composite sections, fiber reinforced polymer (FRP) bars or panels, steel cables like in post-tensioned concrete, and various fibers mixed into the concrete matrix. Likewise, there are various options for material selection and method of implementation for the tension reinforcement could be [42–44]. Traditional steel rebar is possible but difficult to achieve as an integral part of the printing process. For the AM structure to be fully automated, other options such as the inclusion of textiles or fibers [45–49] can be incorporated more easily into the fresh mix or between layers. The literature suggests that fiber reinforced concrete (FRC) can improve the ductility, toughness, and flexural capacity of concrete, and, within the context of AM, FRC has shown two significant results thus far: material extrusion can provide preferential fiber alignment and flexural strength can be improved when fibers are preferentially aligned with the applied stress [45, 48, 50–55].

The role of curing for concrete is crucial for the cement to properly hydrate and gain strength. For traditionally cast concrete, the formwork usually acts as a mold to cure the concrete for about three days before being stripped. There are other methods of curing such as covering with wet burlap or spraying a curing compound on the concrete. However, this step is crucial for concrete performance. AM concrete boasts of the reduction of waste by eliminating the formwork; likewise, it also poses the question of what methods will be best suited to prevent the evaporation of surface moisture in order to prevent shrinkage and improve durability of the concrete [5, 56, 57].

Traditional methods of mechanical testing for hardened concrete properties are not entirely sufficient when measuring hardened properties of AM concrete because the anisotropic nature of the AM concrete needs to be acknowledged within these test methods. While some researchers

have begun to comment on the anisotropic behavior of 3DCP [45, 49, 58], there has not been a comprehensive analysis on this topic. This is expanded in Section 2.5.

2.3.3. Geometric tolerances

Behind almost every physically printed AM part, there is a computer-based model. The model can be drawn with different 3D modeling software and then exported as a stereolithography (STL) file and "sliced" into layers. These layers collectively represent what the physical part will look like. This becomes an issue when the dimensions of the deposited filament do not directly align with the computer-based model and the part loses its essence or overall concept. Park et al. [59] provides a good description of the challenges with geometric tolerances for AM materials and while this is important to address, it is outside of the scope of this thesis.

2.4. Rheology and specialty mix designs for 3DCP

Concrete is a heterogeneous composite material that is composed of four base components: portland cement, fine aggregates, coarse aggregates, and water. Creating specialized mix designs can include other elements such as chemical admixtures (e.g., accelerators, retarders, water reducers, viscosity modifiers), supplementary cementitious materials (SCMs), specialty aggregates, topical compounds such as curing compounds, and more. Creating a specialty mix design is usually dictated by what specific performance requirements the concrete needs to fulfill.

For example, self-consolidating concrete (SCC) was devised in 1988 at Kochi University in Japan by Dr. H. Okamura [60], who recognized a lack of availability of skilled labor. SCC does not require applied vibration in order to properly compact which lowers labor costs and requirements. A high fineness modulus coupled with superplasticizers are key to achieving SCC

properties of a highly flowable yet segregation resistant mix design. Similarly, 3DCP demands specific performance requirements of the concrete mix design to address the challenges previously presented. To reiterate, the performance requirements can be summarized by the pumpability, printability, and buildability of the mix.

To address the challenges and performance requirements, 3DCP requires highly specialized mix designs. There are several studies [3, 4, 16, 24, 61–66] that have tried to address the specific requirements that this new form of concrete construction requires. Currently, most mix designs for 3DCP are limited to mixes with only fine aggregates (*i.e.* mortars); research using larger aggregates is still in development [67]. The water to cement (w/c) and sand to cement (s/c) ratios can vary based on the admixtures, cementitious materials, and aggregates to achieve the desired properties.

A successful mix design is achieved through an iterative process that can largely depend on the AM (*e.g.* material extrusion) and the chosen materials. For example, Kazemian et al. [3] proposed an approach to refining a mix design to reach the specific performance requirements for material extrusion as shown in Figure 2.8. This proposed framework emphasizes the properties of the printed layers such as print quality and shape stability.

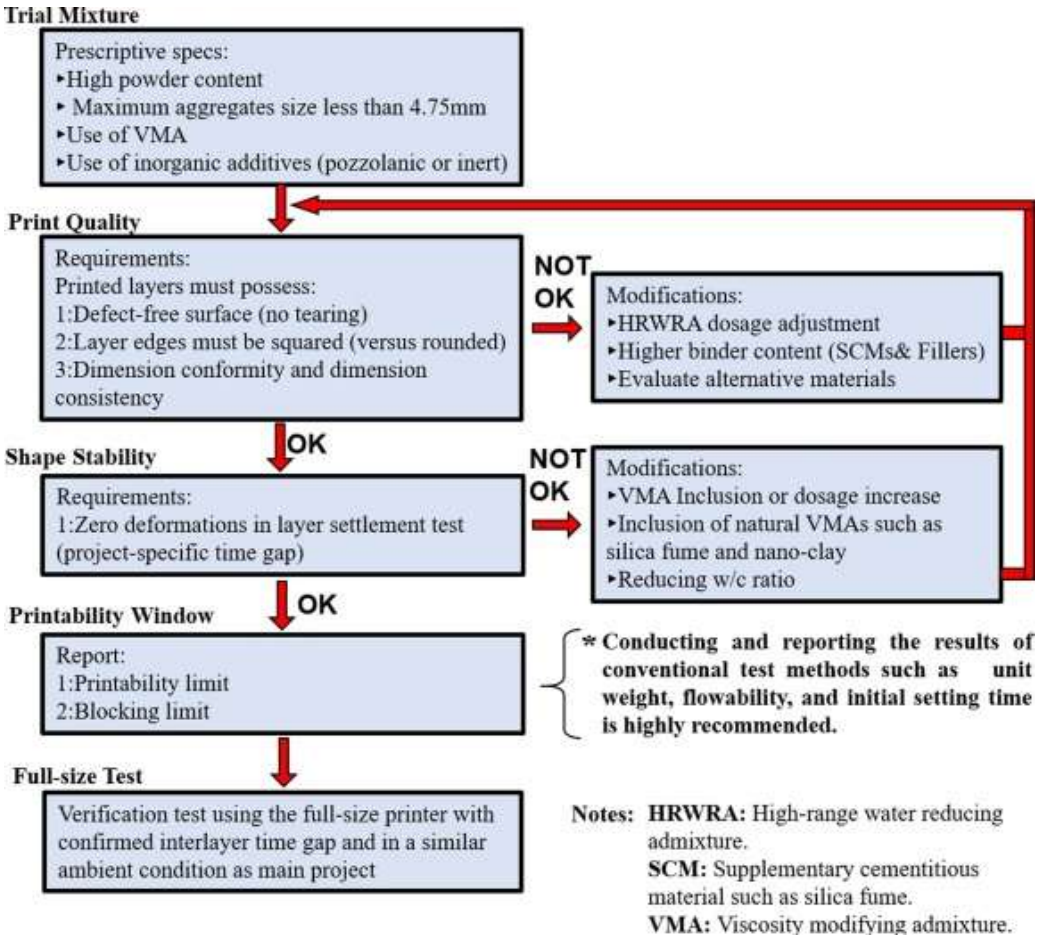

Figure 2.8: Iterative process for refining a mix design to meet desired AM performance properties. (From Zhang et al. [24] (adapted from Kazemian et al. [3]))

Rheology measurement is one of the challenges for fresh mix mortars as previously mentioned (Figure 2.5). Yield stress and viscosity are two material properties that have been measured to help define open time [37]. Setting time for cement pastes can be correlated to yield stress for simplicity and ease [68]. Similarly, viscosity could be correlated to the mini-slump-flow test for cement pastes [69]. Therefore, existing standards for concrete and mortars for setting time and flow could be useful for characterizing fresh mix properties for 3DCP relating to printability, pumpability, and buildability.

2.5. Mechanical properties of hardened concrete

For traditionally cast and molded mortar and concrete specimens, standard ASTM test methods exist for measuring hardened material properties including flexural and compressive strength [70–75]. However, they do not properly account for the anisotropic nature of 3D printed cementitious materials. There are not provisions that consider the orientation of the specimens being tested because for traditionally cast cementitious materials, the orientation should have little to no effect on performance since concrete and mortar are designed as isotropic materials.

Other materials such as metals and polymers face the same challenges in evaluating and characterizing mechanical properties of AM produced parts. Progress has already been made in applying current standards to polymers such as tensile testing with dog-bones for AM specimens [76].

Likewise, studies have begun to investigate the mechanical properties and behavior of 3DCP through various methods [15, 38–40, 45, 48–50, 58, 77–80]. A large focus of the mechanical testing in the literature includes the effect of the layer interface bond on the strength of the materials and how that is affected by different parameters. For example, Sanjyan et al. [77] studied the effect of surface moisture on the interface bond by testing workability, compressive strength, flexural strength, and inter-layer strength. However, these studies are difficult to compare due to differences in materials (e.g. mortars versus concrete), inclusion of fibers (material, length), admixtures, test setup, specimen preparation, loading rate and method (force controlled versus displacement controlled), etc. This, again, highlights the need to develop standard test methods for 3DCP.

2.6. Digital image correlation

Stereo-digital image correlation is a tool that can be used for measuring strains and displacements. This is a non-contact method that is used by optically comparing photos captured over a span of time [81]. In order to be able to use the digital image correlation (DIC) method, a speckle pattern such as in Figure 2.9 needs to be applied to the surface of the material being analyzed.

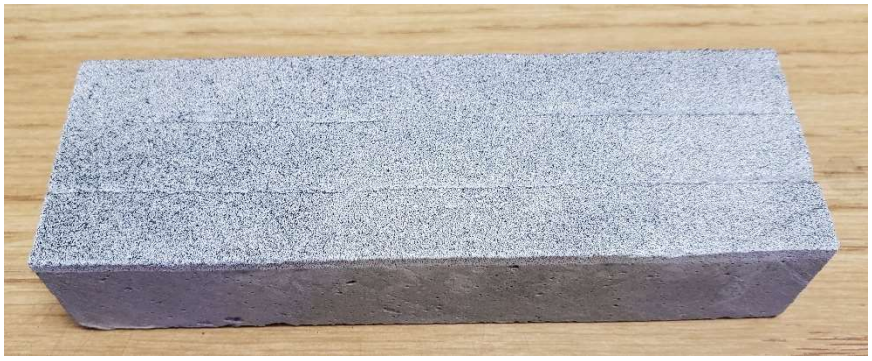

Figure 2.9: Speckle pattern applied to a beam

DIC can be used for to measure plastic deformations or detecting and monitoring crack initiation and propagation [82]. The speckles can be tracked over time using stereo-DIC to determine the strains at any location on the identified surface, or region of interest; the strains are determined by the displacement of the speckles from a defined reference stage [83] as shown in Figure 2.10.

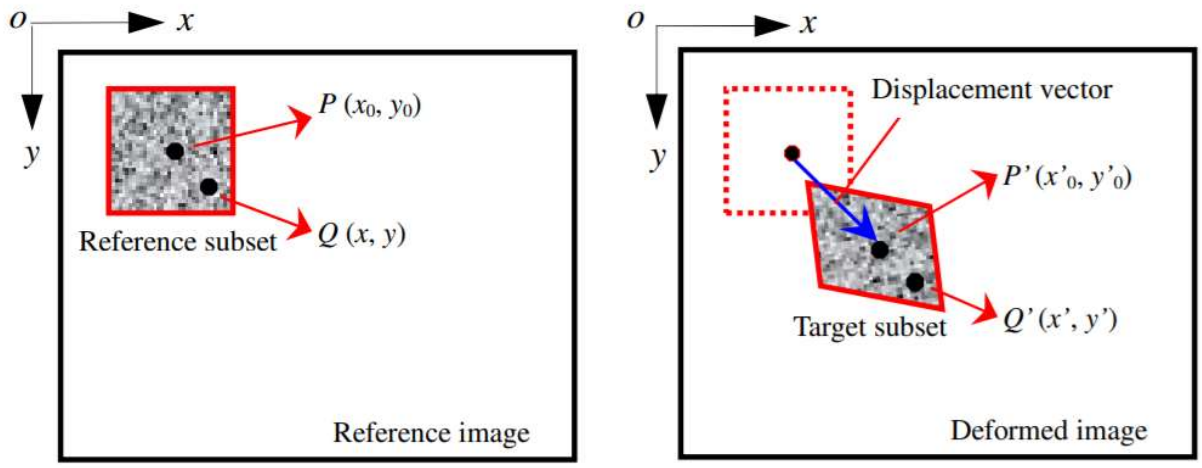

Figure 2.10: DIC speckle pattern displacement (from Pan et al. [83])

The captured photos can be post-processed to analyze the strains at a more localized or global level by changing the pixel size and point distance. While DIC is a powerful non-contact method, there is potential for error to be introduced through the resolution and angle of the cameras, lighting, and preparation of the test surface (smoothness, speckle pattern) [84].

3. PHASE I TESTING

Oak Ridge National Laboratory's (ORNL) Manufacturing Demonstration Facility (MDF) developed the Sky Big Area Additive Manufacturing (SkyBAAM) system that was used to print the AM specimens within this study. Both fresh mix properties and hardened properties were investigated within this study within two phases of testing: Phase 1 testing was performed at the University of Tennessee (UTK) facilities, and Phase 2 testing performed at Virginia Tech (VT) facilities. Testing performed at UTK consisted of three-point bending tests (TPBT). Testing performed at VT consisted of fresh mix testing as well as flexure testing with a TPBT setup using digital image correlation (DIC).

3.1. SkyBAAM setup

SkyBAAM is a large-scale, concrete deposition system which employs the material extrusion AM process [85]. However, SkyBAAM is different from many other material extrusion systems because it is not based on a gantry, or robotic arm, system. SkyBAAM is a cable-driven robot with four stations creating a printing area within the x-axis and y-axis and a crane controlling the z-axis as shown in Figure 3.1.

Figure 3.1: One of the SkyBAAM stations controlling xy-plane (left) and z-axis cable controlled by overhead crane (right)

Since the stations can be moved, the print area has potential for expansion; this is one of the major differences between SkyBAAM and other existing systems. The white build sheet seen in Figure 3.1 (right) covers an approximately 64 ft^2 (5.9 m^2) build platform. Although SkyBAAM is still being adjusted for smaller scale printing within the controlled environmental conditions inside at ORNL, in the future this machine will be able to be taken to a jobsite to print much larger structures.

Within the scope of this project, the only aggregate used was sand; therefore, the nozzle sizes stayed relatively small with a 1.5-inch diameter nozzle used for the printed specimens. The cross-sectional height and width of the extruded filament, or bead, for each layer is mostly dictated

by the size, shape, and directionality of the nozzle. Figure 3.2 depicts how the cementitious material was extruded vertically out of the nozzle. This extrusion technique applies some pressure to existing layers and does not create a finished surface; instead, it creates an oval-like cross-section for each layer causing there to be overhanging, unbonded material on the sides.

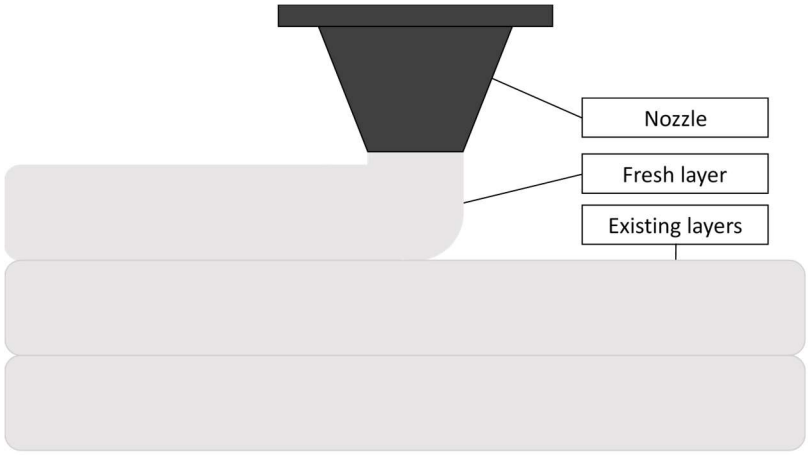

Figure 3.2: Diagram of nozzle extrusion

Current literature suggests that the filaments extruded should have squared layer edges (Figure 2.8) as opposed to rounded ones [3] like the ones produced using this technique. Therefore, the excess bead width was removed from the printed specimens prior to testing.

3.2. Materials and mix design

Due to the complexity of the SkyBAAM parameters, coupled with the variability of cementitious materials, the quality of the print is challenging to consistently repeat. Several parameters affect print quality such as materials, mix design, print head speed, extrusion speed, ambient temperature, processing time, etc.

ORNL previously developed a printable mix design for internal use with SkyBAAM described in Table 3.1. Assuming typical specific gravity values (3.15 for cement, 2.9 for slag, 2.2 for silica fume, 2.65 for sand, and 1 for water) for this mix design, the predicted unit weight

(without air) was 140 pcf, which is reasonable since a typical mortar unit weight is 135 pcf. All the parts printed and tested within the context of the preliminary work used the same mix. A prebagged mortar mix was used for trial prints prior to using the stated mix design because the prebagged mortar was easier to prepare and allowed print parameters to be adjusted in advance to ensure quality of print. Once the parameters were adequately adjusted, the mix design above was prepared. A standup mixer was used which limited the volume of the batches for a print.

Mix Design Materials		
Type III Portland Cement	22.4	*lbs*
Blast Furnace Slag	11.2	*lbs*
Silica Fume	3.75	*lbs*
Sand	56	*lbs*
Glenium	91	*mL*
Water	14	*lbs*

Table 3.1: Mix proportions for standard batch of 0.75 ft^3 mortar

The materials included Type III portland cement, SCMs, sand (fine aggregate), water reducer, and water. Type III cement is used for high early strength development; in the context of additive manufacturing, this can provide the early strength required to prevent layer deformation. However, it could also accelerate the setting time which can reduce the open time window for layer bonding. If the designed print is large, this could become an issue if the elapsed layer print time exceeds the open time. Ground Granulated Blast Furnace Slag (GGBFS or BFS) and silica fume are both SCMs. The use of SCMs can improve the durability of concrete; this is important since 3DCP faces challenges related to curing due to the lack of formwork. Furthermore, the incorporation of these SCMs promotes sustainability through the repurposing of industrial by-products. The inclusion of a superplasticizer allows for a lower w/c ratio while maintaining the necessary level of pumpability and printability; this can increase the strength of the concrete and improve durability as well.

The materials were stored in containers indoors with relatively controlled temperature and humidity. Neither the densities of the materials nor the absorption of the aggregate used in the preliminary work were measured at the time of printing; however, in Section 4.1.1 later in this work, fresh mix and material properties are recorded of a similar, reproduced mix.

The mortar mix was designed to have zero slump. The ideal consistency was empirically determined by being able to hold the material without it slipping through spread fingers; however, once hand vibrated, then the material liquefied enough to slip through. This allowed SkyBAAM to more effectively extrude material by simulating the vibration applied to the hopper during a print. Once the mixture was prepared, it had to be manually transported via wheelbarrow or bucket and loaded into the hopper. In the future, this process would be automated through a pump system and a continuous mixer. Once the material was loaded into the hopper, the extruder was turned on to allow material to pass through and build up enough pressure for consistent flow. Extruded material from this process was placed back into the hopper to reduce waste. After SkyBAAM was continuously extruding material, the print would start.

3.3. Quality of print

The system required closed-loop designs, so single-bead boxes were designed and printed. In order to effectively test for mechanical properties, the printed part had to pass a visual standard of the print. Layers had to have roughly the same filament height and width, demonstrate no tearing of the filament, and show minimal deformation due to applied stresses of preceding layers. An example of an unacceptable print using the prebagged mortar is shown in Figure 3.3.

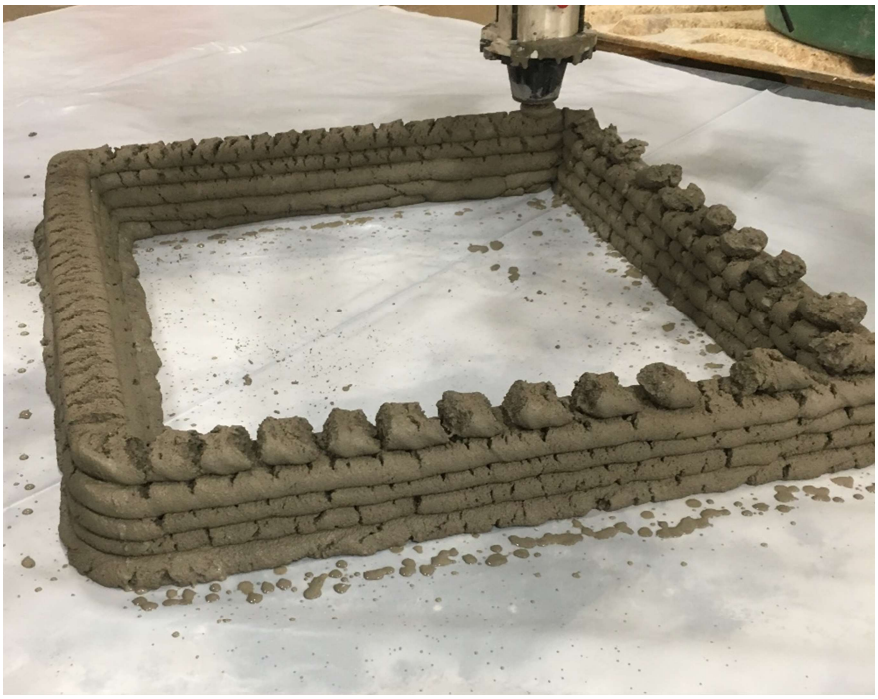

Figure 3.3: Visually unacceptable print with noncontinuous filament

The bottom layer showed excessive spreading on one side, there was major cracking due to poor extrusion consistency, the layers were much thicker than the designed layer height, and after the fourth layer the filament began tearing and clumping with no continuity.

The issues shown in Figure 3.3 were mostly resolved by altering the software as well as the mechanical and electrical hardware of the system which were out of the scope of this project report. Ultimately, using a different extruder and hopper made the printing process much smoother. The mortar mix design was also less susceptible to clumping than the prebagged mortar. An example of a print that passed the visual inspection is shown below in Figure 3.4.

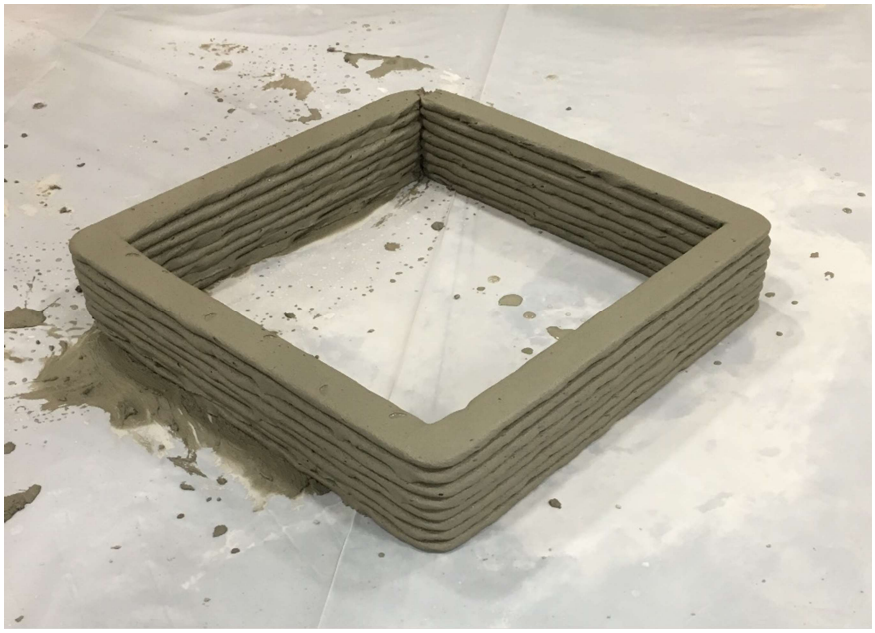

Figure 3.4: Visually acceptable print

Within reason, the filament height and width appeared to be consistent between layers, there was no clumping with only minor imperfections from extrusion, and the part stood erect with little layer deformation. After a printed part passed the visual inspection, it was covered and sealed with plastic to prevent evaporation and allow curing (Figure 3.5). The printed components were sealed with plastic throughout the entire curing process (unless they were being cut or photographed) until they were tested. Curing techniques are critical for allowing the cement to hydrate.

Figure 3.5: Sealed curing of the printed boxes

Without proper curing, a potential issue is differential shrinkage as shown in Figure 3.6. Shrinkage cracking can be caused by ineffective curing methods which leads to the evaporation of water in the mortar. Shrinkage cracking could be prevented by implementing better curing methods, allowing the cement to properly hydrate. For large-scale structures, sealing with plastic is not a realistic method; however, other curing methods such as application of a concrete curing compound could be employed.

Figure 3.6: Differential shrinkage cracking in a printed part

3.4. Flexure testing (Three Point Bending Setup)

3.4.1. Specimen preparation

The printed parts used in this test were printed with a 1.5-inch diameter nozzle. They had 8 layers and were roughly 5 inches tall (Figure 3.7). According to the g-code, the minimum layer time was 1 minute and 37 seconds, and the maximum layer time was 1 minute and 40 seconds. The total expected build time was approximately 13 minutes for the entire box which is much shorter than what could be expected in larger scale projects. There was only 1 inset which means there was

only a single closed loop printed; there was not a fill pattern of any kind or other insets. A single bead width was investigated since many demonstrations thus far have printed structures with single insets; therefore, proposed future testing should be applicable to those cases.

After a minimum of 12 hours, the sample could be moved off the build platform since the mix design used type III cement which is fast setting for early strength gain. The corners of the printed box were then sawcut off leaving 4 sides. From those sides, smaller specimens were extracted (Figure 3.7) using a tile saw since the mix design did not contain any large aggregates and the blade was thin. Only the vertically cut specimens were used for the initial flexural testing, and they were further trimmed to get rid of the excess overhanging bead width in order to have flat, planar surfaces for testing. Once the specimens were prepared, the average width, height, and depth of each specimen was measured with a digital caliper.

Figure 3.7: Side sawcut from printed box with the pieces all stacked in their original place

Once the specimens were extracted as in Figure 3.7, they could be further trimmed down to obtain a rectangular cross-section (Figure 3.8).

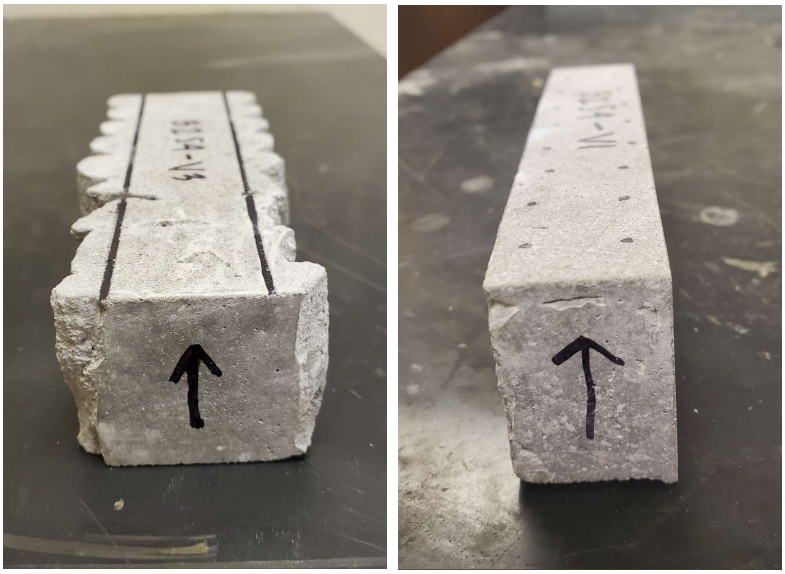

Figure 3.8: Trimmed specimens with rectangular cross-sections

The naming convention used for the 'Specimen ID' indicated the box (or print) number, the side number once the corners were cut off, and the number and direction the specimen was cut. For example, B1S1-V3 was from box (or print) number 1, side number 1, and was the third beam vertically extracted. Similarly, B2S3-H2 was from box number 2, side number 3, and was the second beam horizontally extracted. Using this naming convention helped the bookkeeping process when making visual observations.

3.4.2. Procedure

The first round of testing as a proof of concept was performed during the summer at the University of Tennessee, Knoxville, (UTK) by modifying ASTM C348 [74]. The specimen preparation deviated from the standard since they were not cast, and the materials proportioning was not done in accordance with ASTM C109 [75] as required by the standard. Furthermore, ASTM C348 does not consider anisotropic behavior being explored for the 3D printed cementitious materials.

Three-point bending was used for testing the specimens; Figure 3.9 shows the idealized loading and actual setup using a universal testing machine to apply the load. The center to center span length between supports was 4 inches. The span length was dictated by the length of specimens extracted from the printed part. For example, the length for a vertically extracted specimen was dictated by the maximum height of the printed layers. Based on the ASTM C348 test program at UTK, the loading rate was 593.5 lbf/min for all specimens. However, this ASTM in general does not provide a clear equation for loading rate. The specimens were tested after 28 days of sealed curing (*i.e.*, specimens were wrapped with plastic after they were printed and stored until testing). Peak load and the crosshead displacement were recorded.

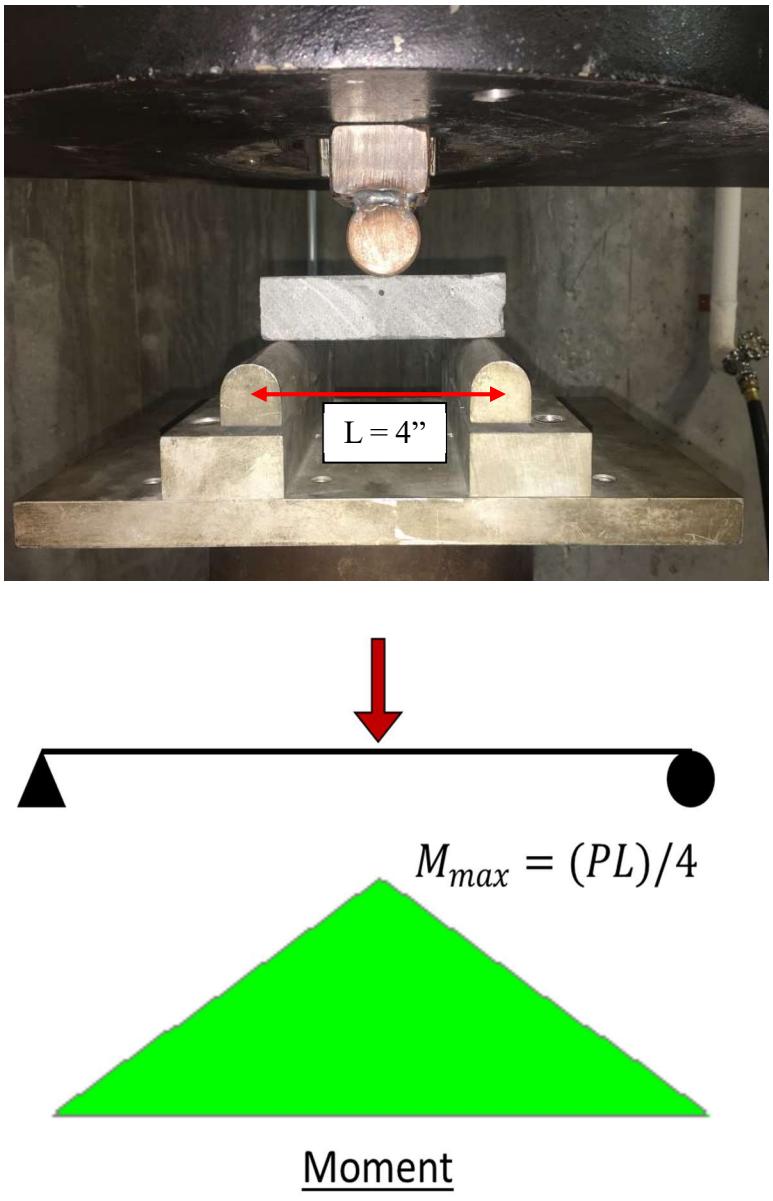

Figure 3.9: Three-point bending test setup at UTK

The specimens were tested in two different orientations: A) load parallel to layer interface and nozzle print direction and B) load parallel to layer interface and perpendicular to nozzle print direction. Figure 3.10 shows the two different orientations with untrimmed specimens prior to cutting the excess material off. The specimens had 8 layers and were tested in the middle approximately at the interface between two of the layers. The other specimens extracted were not trimmed in time for testing and remained in the possession of ORNL.

Figure 3.10: Orientations of the two different loading setups relative to the applied load and print path. Orientation A (left) and orientation B (right)

Rectangular filament edges were recommended by Kazemian et al. [3] and Zhang et al. [24] as shown in the flowchart from Figure 2.8; however, the SkyBAAM system used a round nozzle at the time the specimens were printed. Therefore, trimming the specimens down to a rectangular cross section allowed for two things: 1) flat, planar surfaces for testing and 2) calculation of the modulus of rupture based on a rectangular cross section.

The theoretical flexural stress (modulus of rupture) from Euler-Bernoulli beam theory is expressed by the equation:

$$\sigma_f = -\frac{My}{I} \tag{1}$$

where M is the moment, y is the distance from the neutral axis, and I is the moment of inertia of the cross section. As previously shown in Figure 3.9, the theoretical maximum moment at the center of the beam for center point loading is represented by the equation:

$$M = \frac{PL}{4} \tag{2}$$

where P is the peak load, and L is the span length. That calculated maximum moment, moment of inertia for a rectangular cross section, and the distance from the neutral axis to the extreme tensile fibers can be substituted into the equation:

$$\sigma_f = -\left(\frac{PL}{4}\right)\left(-\frac{d}{2}\right)\left(\frac{12}{bd^3}\right) \tag{3}$$

which can be simplified. Therefore, the equation becomes:

$$\sigma_f = \frac{3PL}{2bd^2} \quad (4)$$

where b is the width, and d is the depth of the cross section. Equation 4 was used to calculate the modulus of rupture for the center point bending flexural tests.

3.4.3. Results

For the Phase I testing, the peak load and crosshead displacement were recorded for each specimen. There were 8 total specimens tested – four in each orientation. A summary including specimen ID, testing orientation, peak load, respective dimensions, and calculated modulus of rupture are presented in Table 3.2 below. The specimens all failed quickly within 1-2 minutes of loading, so it was determined that the loading rate was too high and needed to be revised for future testing.

Table 3.2: Summary of Phase I flexural results

Specimen ID	**Testing Orientation/ Loading Direction**	**Peak Load**	**Support Span (L)**	**Width (b)**	**Depth (d)**	**Modulus of Rupture**
		lbf	*in*	*in*	*in*	*psi*
B1S1 - V1	B	383	4	1.190	1.201	1340
B1S1 - V2	A	481	4	1.254	1.614	884
B1S1 - V3	B	419	4	1.458	1.207	1184
B1S1 - V4	B	411	4	1.463	1.220	1133
B1S1 - V5	B	315	4	1.395	1.208	928
B1S1 - V6	A	222	4	1.184	1.457	530
B1S1 - V7	A	468	4	1.184	1.411	1191
B1S1 - V8	A	261	4	1.214	1.414	645

In order to neatly distill the raw data, a box and whisker plot was prepared (Figure 3.11) to compare the two different orientations. There were four specimens each for orientation A and orientation B. The mean modulus of rupture for orientation A and B was 813 psi and 1146 psi, respectively, and is indicated with an x in the shaded regions. The median is indicated by the center bar in the shaded regions. The extreme values that are depicted as bars are the maximum and minimum datapoints. The standard deviation for orientation A and B was 253 psi and 147 psi, respectively. However, a two sample one-tailed t-test with unequal variances yielded $p = 0.054$, so the means are not statistically different at 95% confidence, which is not necessarily a surprising result given the large standard deviations.

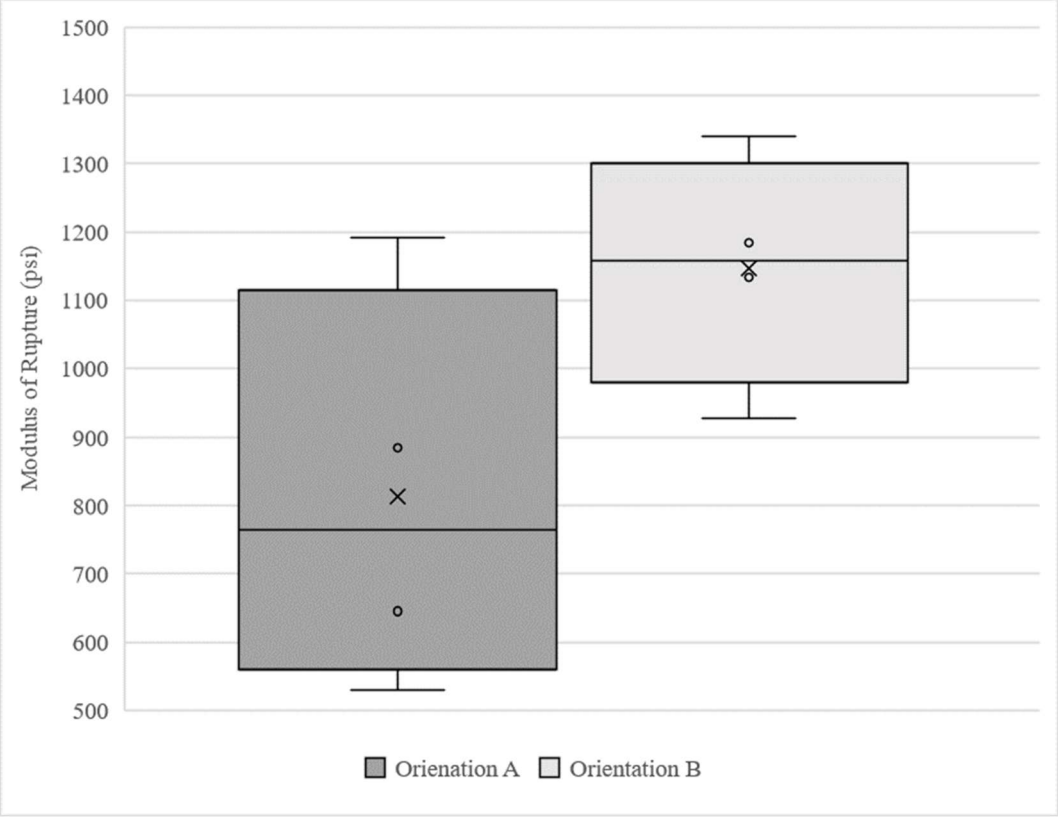

Figure 3.11: Statistical comparison of Phase I raw data

Photos before and after failure were captured (Figure A-1 to Figure A-17), and observations were noted for each specimen. These notes and photos included in Appendix A were

intended to serve as visual documentation of any layer defects in the printed specimens, internal defects at the failure surface, failure patterns, and any other relevant visual information.

As seen in Figure 3.12, there is a defect in specimen B1S1-V6 at the failure surface that looks to be a conglomerated piece of unhydrated cementitious material. In order to better understand the relationship between the two different orientations, specimen B1S1-V6 was considered an anomaly and removed from the statistical data. However, it is important to note that these types of defects are not uncommon in concrete, so 3DCP systems should address similar conglomerates when printing by somehow removing larger pieces of cementitious materials. It should also be investigated whether specific orientations are more susceptible to failure in the presence of defects such as the one noted.

Figure 3.12: Detailed view of defect in B1S1-V6

By removing the B1S1-V6 data point, there were three specimens for orientation A and three specimens for orientation B. The mean modulus of rupture for orientation A and B was 907 psi and 1146 psi, respectively. The standard deviation for orientation A and B was 223 psi and 147 psi, respectively. The mean increased and the standard deviation decreased for orientation A, but orientation B still appeared to outperform orientation A as shown in an updated box and whisker plot in Figure 3.13. The x in the shaded regions indicates the mean value. The median is indicated by the center bar in the shaded regions. The extreme values that are depicted as bars are the

maximum and minimum datapoints. Another two sample one-tailed t-test with unequal variances yielded p = 0.135, so the means are not statistically different at 95% confidence. Again, this was expected since removing the data point with a visible defect brought the means closer together by removing the low anomaly.

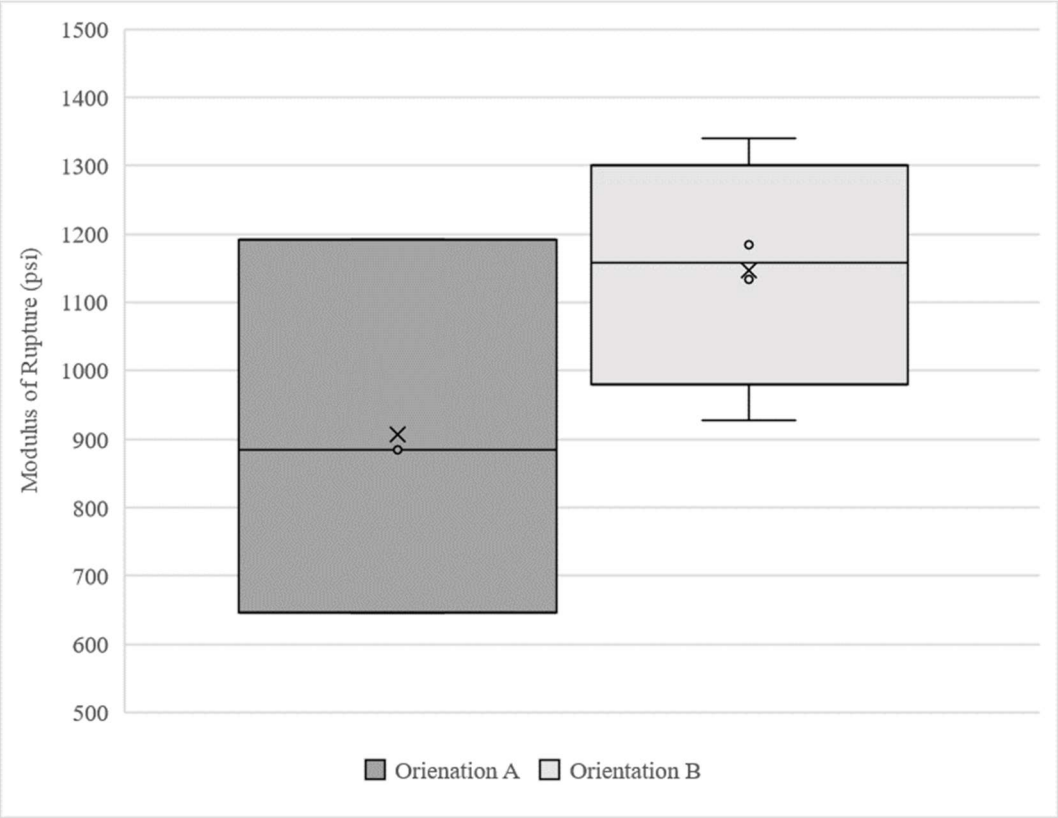

Figure 3.13: Statistical comparison between Phase I adjusted data

3.4.4. Conclusions

Based on the preliminary results from Phase I, the specimen preparation worked; however, the load rate was extremely high and not adjusted based on the width and height for each beam. Furthermore, simply finding the modulus of rupture did not provide much information about how the load was distributed or transferred between layers. Orientation B initially appeared to outperform orientation A, but the means were not statistically different due to high standard

deviations. Because of the high loading rate and inconclusive results, further investigation was required. Specifically, further investigation including how defects affect performance for each orientation was of interest.

4. PHASE II TESTING

4.1. Fresh mix testing and early strength development

Fresh mix properties are extremely important for understanding three of the main aspects relating to 3DCP material delivery and placement (previously mentioned in Section 2.3.1 and Figure 2.7): pumpability, printability, and buildability. The fresh mix properties investigated within this study included mortar flow and setting time. Flow provides information relating to concrete pumpability and printability whereas setting time provides information relating to printability and buildability by looking at initial set and final set. If the concrete sets too quickly, it could affect printability by "tearing" or "clumping" during extrusion, as was shown in Figure 3.3. If the concrete sets too slowly, it could affect buildability through excess layer deformation. Additionally, 1-day compressive tests were performed to complement the fresh mix tests by providing more information about early strength development, also relating to buildability.

4.1.1. Materials

The starting point for the materials for the fresh mix testing was the ORNL developed mix design from Table 3.1 in Section 3.2 since this mix was empirically proven to be printable, pumpable, and buildable with the SkyBAAM system. However, the sand source was different for the fresh mix testing than for the hardened concrete testing since the specimens were printed at ORNL. The hardened concrete used a natural sand (local to ORNL) whereas the fresh mix testing used both natural sand (local to VT) and manufactured sand. The sands used in the Phase II fresh mix testing were limited to a nominal maximum aggregate size of 2.38 mm due to observed SkyBAAM issues when using larger aggregates. Then a sieve analysis was performed per ASTM C136 [86] and the results are presented in Figure 4.1.

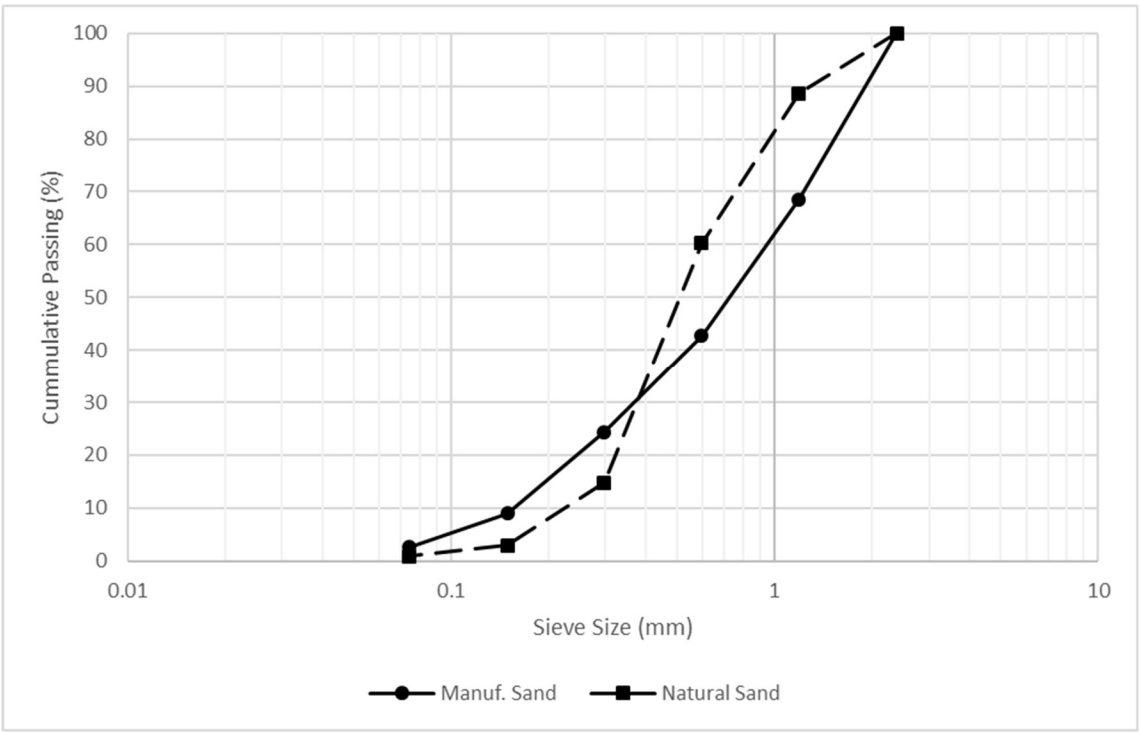

Figure 4.1: Sieve analysis of both fine aggregates

Other material properties such as specific gravity, absorption, and moisture content at "air dry" (AD) conditions were found for both sands prior to investigating the fresh mortar properties. The bulk specific gravity, apparent specific gravity, and absorption were found according to ASTM C128 [87]. Moisture content was found per ASTM C566 [88]. These properties are summarized in Table 4.1 below.

Table 4.1: Material properties of the Phase II fresh mix sands

	Natural Sand	**Manufactured Sand**
Bulk Specific Gravity	2.61	2.82
Apparent Specific Gravity	2.66	2.84
Absorption, %	1.08	0.47
Moisture Content, %	0.15	0.03

The sands were considered with different moisture states: oven dried (OD), "air dry" (AD), and saturated surface dry (SSD). Where OD was dried in an oven overnight to remove water from the pores such that the moisture content is zero. AD was taken from the current condition in the

stockpile where the pores are partially filled with water. SSD condition was when the absorption capacity was met by the moisture content by adding that percent of water by mass to OD sand and allowed to sit for several hours in a sealed container. The moisture condition of the aggregate can become a critical factor in the performance of cementitious materials. Moisture condition of the fine aggregate affects the batched volume of sand, and at various moisture conditions, this can affect the w/c ratio and s/c ratio. Not accounting for the moisture condition of the aggregate can affect slump loss, setting time, strength gain and ultimate strength, development of the interfacial transition zone, etc. [89–91]. Therefore, for AM applications, the moisture condition of the aggregate may influence the predictability and reliability of the fresh properties.

For the fresh mix and early strength testing, a variety of cement mortars were investigated as shown in Table 4.2 to demonstrate the need for quality control and quality assurance methods for 3DCP raw materials. Group 1 refers to mortars that did not properly account for the moisture content and absorption of the aggregates in the mix design while Group 2 refers to mixes that did account for changes in absorption and moisture content differences.

Table 4.2: Matrix of mix types for fresh mix testing with varying sand types and hydration states

GROUP 1	**Natural Sand**	**Manufactured Sand**
OD	Mortar 1	Mortar 4
AD	Mortar 2	Mortar 5
SSD	Mortar 3	Mortar 6
GROUP 2	**Natural Sand**	**Manufactured Sand**
OD	Mortar 7	Mortar 10
AD	Mortar 8	Mortar 11
SSD	Mortar 9	Mortar 12

The mortars were prepared using the procedure for mixing mortars from ASTM C305 [92], although the materials were not batched based on the standard ratios given in ASTM C305. Group 1 mix designs were inspired by ORNL's original mix design. There was significant research prior to this project to determine the ideal mix design; however, once it was determined, the intention of the mix design was distorted since the moisture content of sand can fluctuate and was not measured prior to printing. SkyBAAM is still in development and focused on demonstration of the concept of large-scale 3DCP. Improving the mechanical performance and robotics of SkyBAAM were the priorities; therefore, the ratios of mass of each material in the mix design were held constant for ease and to save time.

The Group 1 mix designs stayed the same by mass as in Table 3.1 for all 6 mortars which means the water to cement (w/c) ratio and the sand to cement (s/c) ratio were both changing. Group 2 mix designs are standard mix designs that incorporate the specific gravities of the materials and the absorption and moisture content of the fine aggregates. The w/c ratio was 0.375, and the s/c ratio was 1.5 for all Group 2 mortars. Those mix designs are presented in Appendix B (Table B-1 through Table B-6).

4.1.2. Procedures

Flow was tested for each mortar per ASTM C1437 [93] and is defined as the percent increase of the base diameter. This is an important unit of measurement for 3DCP since flow relates to concrete pumpability and printability.

Setting time was performed by modifying ASTM C807 [94]. The molded specimen was sealed cured between dropping the needle instead of being placed in an environmental chamber.

Setting time can play a significant role in addressing the challenges of open time in fresh mix concrete in 3DCP as previously discussed in Section 2.3.

Finally, early compressive strength was determined for the different mortars to investigate how the setting time and flow related to the strength development per ASTM C109. The compression tests were performed after 1 day. Three specimens were molded and tested for each mortar. This is an important measurement to monitor early compressive strength as it relates to buildability for 3DCP. While this test is not directly representative of the in-situ material for printed concrete, it can still provide valuable information about the relationships between flow, setting time, and early compressive strength.

4.1.3. Results

This section presents results from flow, setting time, and early compressive strength testing.

4.1.3.1. Flow

The flow for each mortar was recorded and presented in Table 4.3.

Table 4.3: Summary of flow for each mortar

Mortar No.	Flow
1	44%
2	53%
3	67%
4	81%
5	74%
6	81%
7	61%
8	47%
9	57%
10	72%
11	76%
12	82%

Table 4.4 and Figure 4.2 summarize the differences between the natural sand versus the manufactured sand in Groups 1 and 2. There were three data points in each set. Average and standard deviation were calculated for each category; in addition, range was calculated since this is a common measurement for ASTM standards. In Figure 4.2, the x in the shaded regions indicates the mean value. The median is indicated by the center bar in the shaded regions. The extreme values that are depicted as bars are the maximum and minimum datapoints.

Table 4.4: Comparing flow results by sand type for Group 1 and Group 2

Category	Group 1			Group 2		
	Average	Standard Deviation	Range	Average	Standard Deviation	Range
Natural Sand	55%	9%	42%	55%	6%	25%
Manuf. Sand	79%	3%	9%	77%	4%	12%

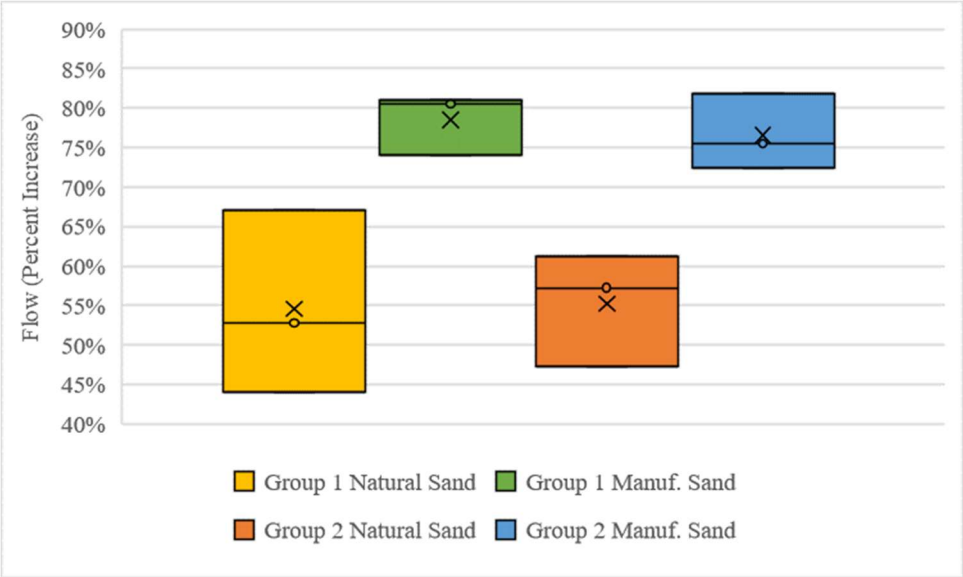

Figure 4.2: Box and whisker plot comparing flow results by sand type

Interestingly, the average for each sand type did not significantly change between Group 1 and 2 results. Overall, the manufactured sand had less variability than the natural sand and demonstrated greater flow increase than the natural sand in all cases. This was likely due to absorption content as well as gradation, fineness, and particle shape differences between the sands.

The absorption was 0.47% for the manufactured sand whereas the natural sand had an absorption of 1.08%. Because the manufactured sand had a lower absorption, the potential for variation in the flow was reduced. This is highlighted in the fact that the standard deviations for manufactured sand were 3% for Group 1 and 4% for Group 2. Since the natural sand had a larger absorption, it had a higher standard deviation for Group 1 than Group 2 which were 9% and 6%, respectively. As these two sand sources had relatively low absorption capacities, it is likely that fine aggregates with high absorption capacities would yield significantly greater variability between OD and SSD conditions, such as the slump loss behavior shown in concretes with highly absorptive recycled concrete aggregates [90].

When comparing the flow results for the 12 different mortars, the moisture condition was investigated to determine which performed the most consistently between the different sand types. The average, standard deviation, and range for the three different moisture conditions regardless of whether water adjustments were made are reported in Table 4.5. There were four data points in each set.

Table 4.5: Comparing flow results by moisture condition overall

Category	Average	Standard Deviation	Range
OD	65%	14%	57%
AD	62%	13%	45%
SSD	72%	10%	34%

However, upon further inspection the range between the two different sand types changed significantly based on the moisture condition and the way absorption and moisture content were accounted within the mix design. Each set had only two data points; therefore, standard deviation was not calculated, only range for this comparison. For Group 1 where water was not properly

adjusted, the OD sands showed the largest range between results as presented in Table 4.6. Alternatively, the OD sands showed the smallest range for Group 2 and overall.

Table 4.6: Comparing flow results by moisture condition for Group 1 and Group 2

Category	Group 1		Group 2	
	Average	Range	Average	Range
OD	63%	59%	67%	17%
AD	63%	34%	61%	46%
SSD	74%	18%	70%	35%

It should be noted that there was only one data point for each of the 12 unique mortars. More data points would increase the confidence in any conclusions drawn from these trends.

4.1.3.2. Setting time

The setting time as defined by ASTM C807 for each mortar was recorded and presented in Table 4.7.

Table 4.7: Summary of setting time for each mortar

Mortar No.	Setting Time *(minutes)*
1	145
2	153
3	199
4	120
5	164
6	196
7	189
8	169
9	183
10	171
11	191
12	188

As expected, the standard deviation and range for setting time were larger for Group 1 than for Group 2 as shown in Table 4.8. There were three data points in each set. The setting times for Group 2 are higher than Group 1 likely due to the established w/c ratio.

Table 4.8: Comparing setting time results by sand type for Group 1 and Group 2

Category	Group 1			Group 2		
	Average Setting Time *(minutes)*	Standard Deviation *(minutes)*	Range	Average Setting Time *(minutes)*	Standard Deviation *(minutes)*	Range
Natural Sand	166	24	33%	180	8	11%
Manuf. Sand	160	31	47%	184	9	11%

As previously shown in Figure 4.2, flow was heavily influenced by the sand type rather than the moisture condition. Unlike for flow, the setting time was not as affected by sand type since the natural sand and the manufactured sand both experienced a similar reduction in standard deviation and increase in average setting time between Group 1 and Group 2 results. This can be seen in Figure 4.3, where the x in the shaded regions indicates the mean value. The median is indicated by the center bar in the shaded regions. The extreme values that are depicted as bars are the maximum and minimum datapoints.

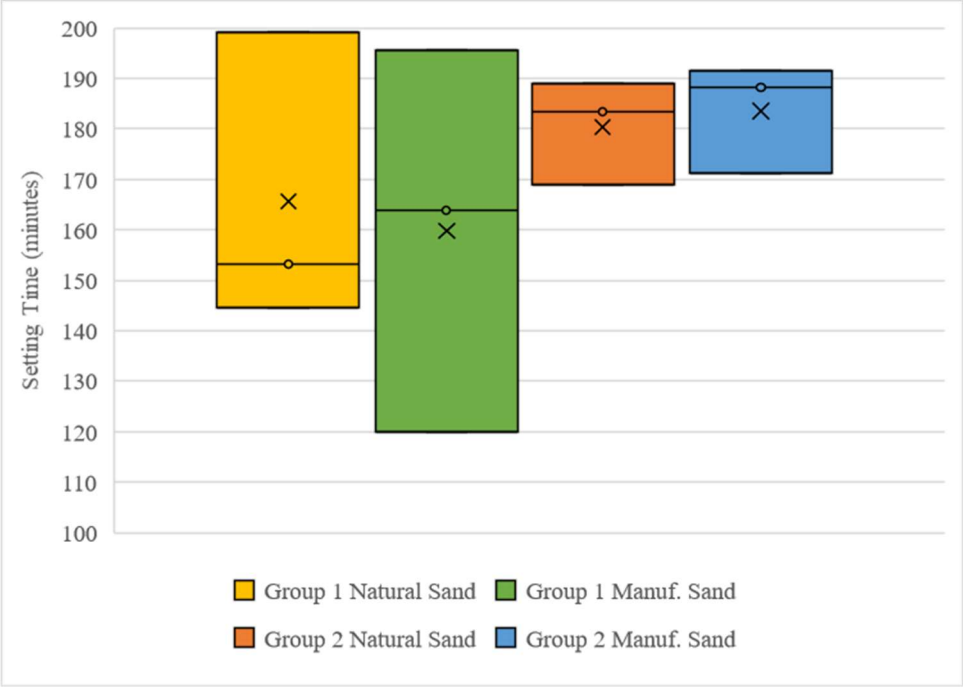

Figure 4.3: Box and whisker plot comparing setting time results by sand type

Although the setting time was not heavily influenced by the sand type, the differences in the standard deviations and ranges between Group 1 and Group 2 indicated that it was affected by the moisture condition of the sands and how those were accounted for within the mix designs. This was confirmed in Table 4.9 where the OD sand has the highest standard deviation and SSD has the lowest at 26 minutes and 6 minutes, respectively. There were four data points in each set.

Table 4.9: Comparing setting time results by moisture condition overall

Category	Average Setting Time *(minutes)*	Standard Deviation *(minutes)*	Range
OD	156	26	44%
AD	169	14	23%
SSD	192	6	8%

When looking at the performance between Group 1 and Group 2 based on moisture condition in Table 4.10, the trends were similar. For both groups, the SSD sand performed the most consistently with the highest setting times; this is expected since the sand will theoretically

neither give nor remove water from the cement paste. This means the cement hydration process is not as influenced by the sand. For Group 2, the average setting time and range for OD and AD were very similar. The result that the OD sand performed slightly better than the AD sand was expected since the AD sand can have varying moisture content based on the depth of sand in a pile or the relative humidity (RH) in the environment. There were two data points in each set.

Table 4.10: Comparing setting time results by moisture condition for Group 1 and Group 2

Category	Group 1		Group 2	
	Average Setting Time *(minutes)*	Range	Average Setting Time *(minutes)*	Range
OD	132	19%	180	10%
AD	159	7%	180	13%
SSD	197	2%	186	3%

The Group 1 results agree with the literature. For instance, Sri Ravindrarajah et al. [95] demonstrated than the setting time of a mortar with a highly absorptive fine aggregate (6.20%) was less than the setting time of conventional sand (0.63%) even though both fine aggregates were in an air-dry condition. Sri Ravindrarajah et al. argued that this result was attributable to the significant moisture absorption of the highly absorptive aggregate.

None of the pairs from Table 4.10 exceeded the maximum multilaboratory standard deviation of 15.2 minutes per ASTM C807. However, clearly the Group 2 mixes produced more consistent, predictable behavior. For 3D printed concrete, this becomes a very important quality control issue, since there is limited open time (Figure 2.7). From a production perspective, it is highly desirable to have a predictable open time that can be designed and accommodated.

4.1.3.3. Early Compressive Strength

The compression testing was performed on three specimens for each of the 12 mortars. The results are summarized in Table 4.11.

Table 4.11: 1-day compressive strength results for each mortar

	1-day Compressive Strength (*psi*)					
Sample No.	Mortar 1	Mortar 2	Mortar 3	Mortar 4	Mortar 5	Mortar 6
1	3053	3069	2190	2516	3675	2446
2	2631	3066	2068	2386	3955	2340
3	2834	3024	2182	2522	3444	2472
Average	2839	3053	2147	2475	3691	2419
Range	14.87%	1.47%	5.72%	5.48%	13.84%	5.45%
Sample No.	Mortar 7	Mortar 8	Mortar 9	Mortar 10	Mortar 11	Mortar 12
1	2383	2845	2467	2710	3083	2528
2	2421	2854	2625	2797	3133	2539
3	2415	2776	2630	2750	3003	2558
Average	2406	2825	2574	2752	3073	2541
Range	1.57%	2.77%	6.32%	3.17%	4.22%	1.20%

The same results from Table 4.11 are plotted in Figure 4.4 to show the trends between the averages of each mortar.

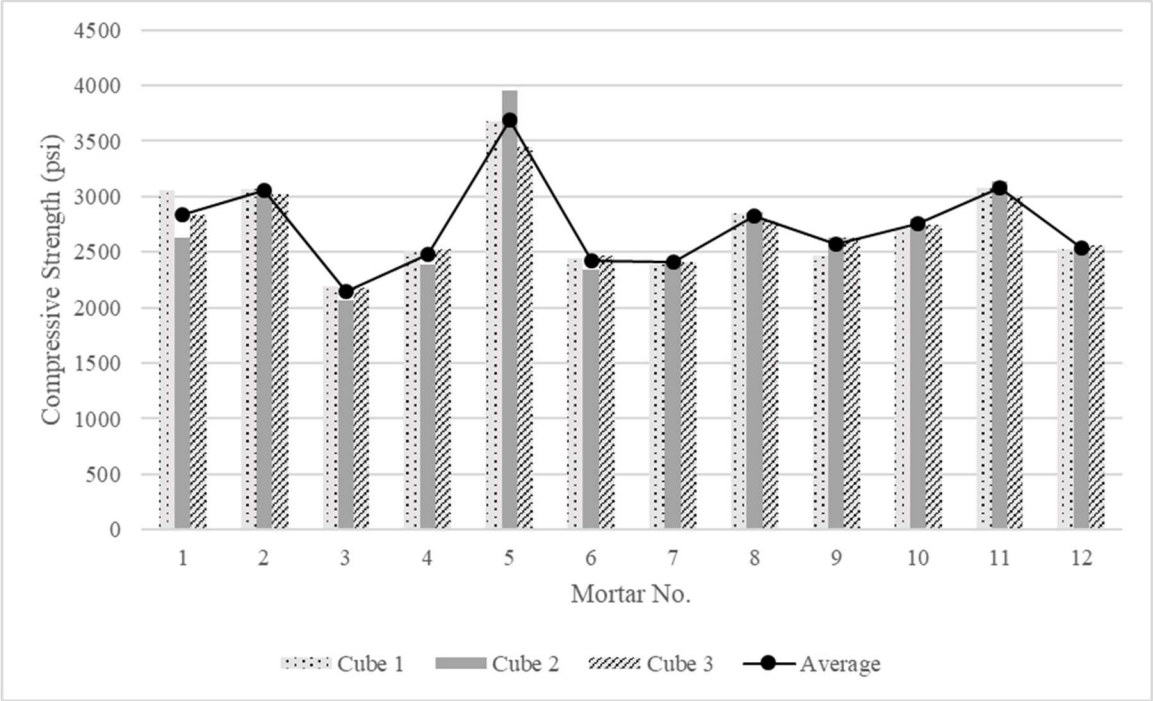

Figure 4.4: 1-day compressive strength results with average trend

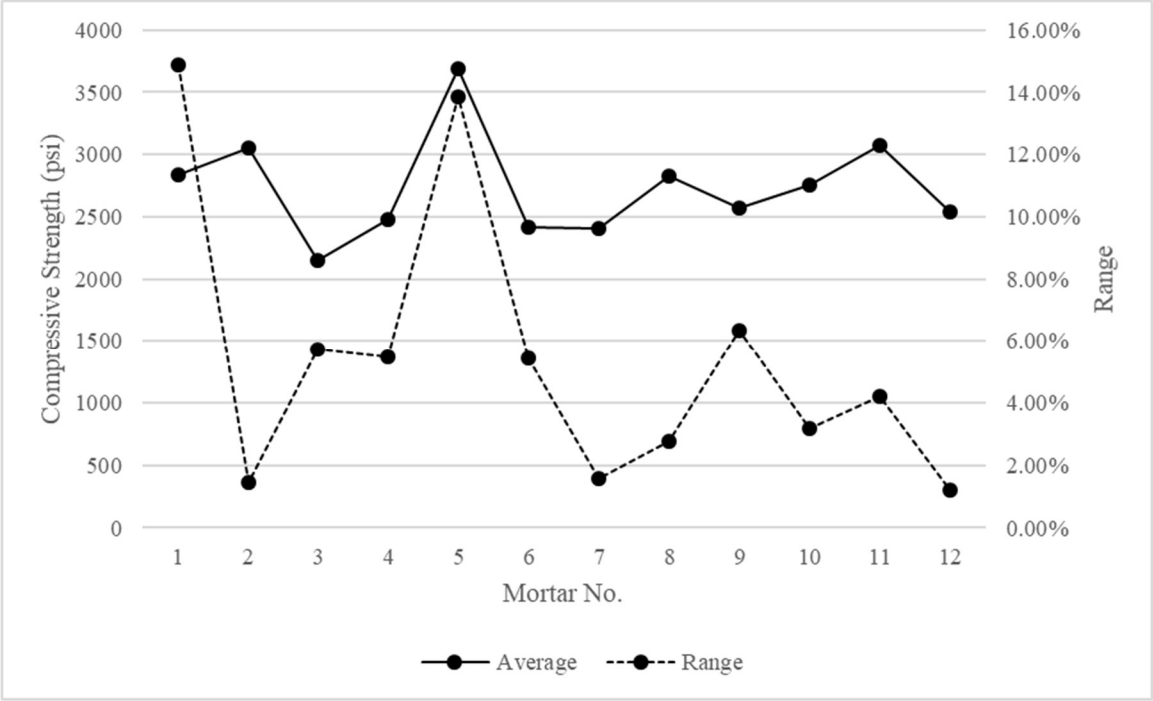

Figure 4.5: Comparing the average and range for 1-day compressive strengths for each mortar

When calculating the average, standard deviation, and range for the subsequent comparisons, all three specimens for each mortar were included rather than only reporting on the average for each mortar. This was to provide a more inclusive comparison and demonstrate which comparisons were the most or least consistent overall. As with flow and setting time, the first comparison made was comparing the early compressive strength results for each sand type in Groups 1 and 2 as shown in Table 4.12. There were nine data points for each set. Similarly to the setting time results, the range was reduced for both sands between Group 1 and Group 2 results.

Table 4.12: Early compressive strength results by sand type for Group 1 and Group 2

Category	Group 1			Group 2		
	Average Compressive Stress *(psi)*	Standard Deviation *(psi)*	Range	Average Compressive Stress *(psi)*	Standard Deviation *(psi)*	Range
Natural Sand	2679	401	37%	2602	179	18%
Manuf. Sand	2862	601	56%	2789	222	22%

However, as shown in Figure 4.6, the compressive strength was slightly reduced for both sand types between Group 1 and Group 2. Inversely, the results for setting time had shown an increase between Group 1 and Group 2. This demonstrates the concept of the conflicting fresh mix design requirements for a printable, pumpable, and buildable mix. In Figure 4.6, the x in the shaded regions indicates the mean value. The median is indicated by the center bar in the shaded regions. The extreme values that are depicted as bars are the maximum and minimum datapoints.

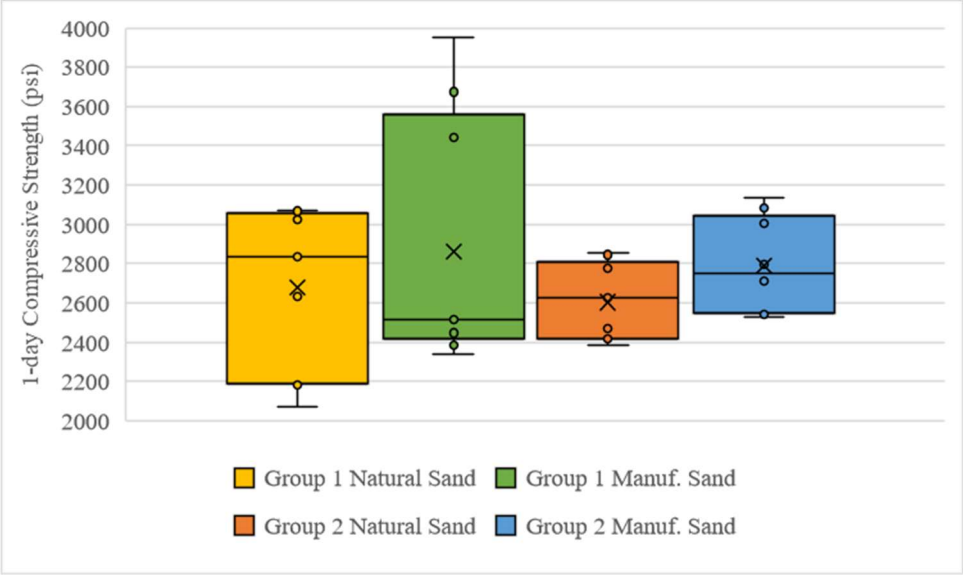

Figure 4.6: Box and whisker plot comparing early compressive strength results by sand type

The manufactured sand obtained a slightly higher compressive strength for both groups indicating that sand type had a slight influence on performance likely due to the particle shape and gradation of manufactured sand. Manufactured sand is typically crushed stone to meet certain gradation requirements; however, the process of crushing leads to more jagged particle shapes. Natural sand has a more rounded shape due to gradual and more even wearing of the sand. Therefore, the roughness of the manufactured sand results in greater mechanical interlock and surface area for bonding, thereby yielding greater compressive strengths than the natural sand in Figure 4.6.

Compressive strength is known to be influenced by the w/c ratio as well. So, again, the different moisture conditions were compared, and the results are presented in Table 4.13. There were 12 data points in each set.

Table 4.13: Early compressive strength results by moisture condition overall

Category	Average Compressive Stress *(psi)*	Standard Deviation *(psi)*	Range
OD	2618	205	26%
AD	3160	340	37%
SSD	2420	177	23%

In general, all the standard deviations and ranges were fairly high. As shown in both Table 4.13 and Figure 4.7, the OD and SSD sands performed the most consistently. In Figure 4.7, the x in the shaded regions indicates the mean value. The median is indicated by the center bar in the shaded regions. The extreme values that are depicted as bars are the maximum and minimum datapoints. The mortars with AD sands were able to achieve the highest average 1-day compressive strength but also had the highest standard deviation and range. The results in Figure 4.7 agree with the literature: concretes with highly absorptive aggregates, such as recycled concrete aggregates, have been shown to achieve the greatest compressive strength when the moisture condition is in between OD and SSD [89, 96].

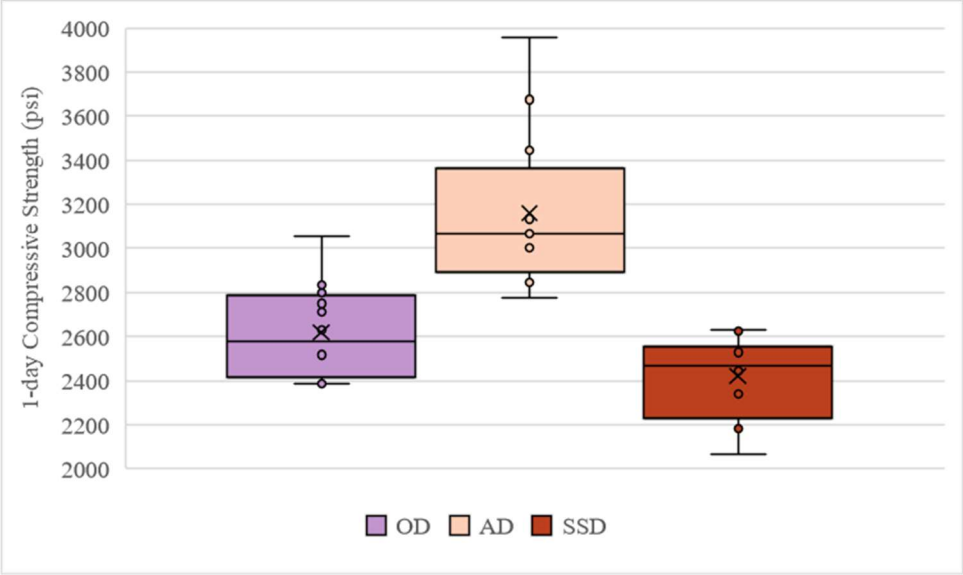

Figure 4.7: Box and whisker plot comparing 1-day compressive strength results by moisture condition overall

As expected, Group 1 had higher variability for each moisture condition than its Group 2 counterpart as shown in Table 4.14. There are 6 data points in each set. The mortars with SSD sands once again were the most consistent among the three different moisture conditions for both groups, but they achieved lower average compressive strengths overall. For Group 1, the lower average compressive strength was expected as well due to the higher w/c ratio. The s/c ratio being reduced may have also led to this reduced strength. As aggregates absorb water while the mortar is still fresh, the local w/c ratio surrounding the aggregate is affected, which has been shown to detrimentally impact the development of the interfacial transition zone and strength development [91].

Table 4.14: Comparing 1-day compressive strength results by moisture condition for Group 1 and Group 2

Category	Group 1		Group 2	
	Average Compressive Stress *(psi)*	Range	Average Compressive Stress *(psi)*	Range
OD	2657	25%	2579	16%
AD	3372	28%	2949	12%
SSD	2283	18%	2558	6%

Based on the precision requirements from ASTM C109, the maximum acceptable range of results for a single laboratory using blended cements with a constant flow is 10.7%. It should be noted that the mortars compared within Table 4.14 were not prepared with constant flow or constant w/c ratios. However, only the mortars with SSD sands in Group 2 were within that requirement.

4.1.4. Conclusions

Although the three test methods (flow, setting time, and early compressive strength) used are not direct measures of printability, pumpability, and buildability, they can serve as qualitative indicators as to how different mortars will perform for potential 3D printing applications. Furthermore, these tests are relatively affordable, are not labor-intensive, and are fairly straightforward to complete.

For 3D printed concrete, control of the fresh properties is very important to ensure that the mixture is printable, pumpable, and buildable; more importantly, these properties need to be designed such that the behavior and performance of the mixture can be predicted and accommodated. The need for properly accounting for the moisture content, absorption, and sand type in the mix design was shown in the differences between results for Group 1 and Group 2.

Clearly the results for setting time and compressive strength demonstrated that there was less variability in the properties when the moisture condition of the aggregate was measured and accounted. For example, this was demonstrated by through a 55 percent decrease in the standard deviation for early compressive strength for natural sand and a 63 percent decrease for manufactured sand after properly accounting for moisture. Similarly, the setting time for natural sand had a 67 percent reduction in the standard deviation between Groups 1 and 2, and the manufactured sand had a 71 percent reduction. Therefore, it is recommended that mixtures used in 3D printing of cementitious composites should design and accommodate the moisture condition of the aggregate to optimize the predictability of the fresh and early-age properties.

4.2. Flexure testing (Three Point Bending Setup) with digital image correlation

After the preliminary testing in Phase I was completed, more testing was needed to draw conclusions about the anisotropic behavior when loading the 3D printed specimens in different orientations. That prompted more flexural testing to be performed but with several changes implemented. Instead of using ASTM C348 as a guide for the loading rate, the ASTM C293 lower loading rates seemed more appropriate. In addition, it was desired to gain more information about how the strains were developing within the specimens, so digital image correlation (DIC) was performed with the flexural testing. This section details the specimen preparation, procedure, results and conclusions of the Phase II flexural testing with DIC.

4.2.1. Specimen preparation

The specimens for the Phase II tests were prepared similarly to Phase I flexural tests. The box (e.g., Figure 3.4) that the specimens for the Phase II tests were extracted from was printed on June

19, 2019 using the same mix design and g-code as the one printed for the Phase I tests on June 18, 2019. The print from June 19 had more visual defects for the bottom four layers though due to mechanical irregularities with SkyBAAM. The effect that these defects had were included in the discussion within the results section.

In Phase I, the two orientations that were tested were A and B as shown in Figure 4.8. Recalling from Section 3.4.1, orientation A was tested with the load parallel to the layer interface and the print path direction, and orientation B was tested with the load parallel to the layer interface and perpendicular to the print path direction.

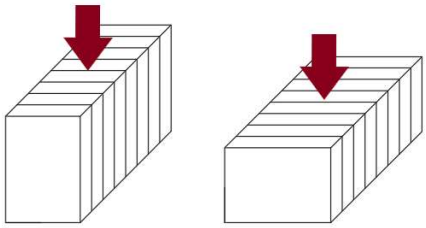

Figure 4.8: Orientation A (left) and orientation B (right) with respect to loading

In Phase II testing, two more orientations were added to orientations A and B to further investigate the anisotropic properties of 3DCP: orientations C and D as shown in Figure 4.9.

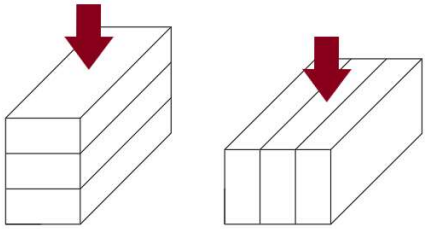

Figure 4.9: Orientation C (right) and orientation D (left) with respect to loading

Orientation C was tested with the load perpendicular to the layer interfaces and the print path. Orientation D was tested with the load parallel to the layer interfaces and perpendicular to the print path.

4.2.2. Procedure

As previously noted, there were several changes implemented in Phase II flexural testing. These changes improved and refined the testing procedure such that more information could be collected from the flexural tests.

After the specimens were prepared, the average width, height, and length were measured and recorded. In addition, the mass was recorded for each specimen. This was to investigate the relationship between the unit weight and performance.

The loading rate was adjusted to follow ASTM C293 loading rate requirements using the equation:

$$r = \frac{2Sbd^2}{3L} \tag{5}$$

where r is the loading rate, S is the rate of increase in the maximum stress on the tension face, b is the average width, d is the average depth, and L is the span length. For all 29 tests, S was 150 psi/minute and L was 4 inches.

The equation for modulus of rupture remained the same as used in Phase II for a rectangular cross section based on Euler-Bernoulli beam theory. However, it should be noted that Euler-Bernoulli beam theory is applicable to isotropic, linear elastic materials, and it neglects shear effects. When the span to depth ratio of a beam is sufficiently large, then the shear effects may need to be considered. The equation for modulus of rupture used in ASTM C293 does not account for shear effects since the standard requires a span to depth ratio of 3. However, that was not achieved for the tested specimens within this project.

A test setup was fabricated for TPBT with a span length of 4 inches to test the specimens at the Thomas M. Murray Structures and Materials Laboratory at VT. It is important to note that

the age of specimens, testing location, testing machine, and the program used to run the Phase I and Phase II tests were different. The specimens were securely sealed with plastic and remained indoors at a controlled temperature once transported from ORNL.

There were 29 total specimens tested: 7 for orientation A, 7 for orientation B, 8 for orientation C, and 7 for orientation D. The specimens with orientations A and B were tested after 155 days of sealed curing. The specimens with orientations C and D were tested the next day after 156 days of sealed curing. Even though testing was performed on two different days, the results were comparable since the specimens were well past 28 days old and all tests were completed within 38 hours total. Peak load and the crosshead displacement were recorded using the program that controls the MTS machine.

The DIC system, with ARAMIS sensors and software, also recorded the load for every stage through an analog input going from the MTS machine to the laptop controlling the DIC sensors and cameras. In addition, the DIC captured and recorded several photos to analyze the strains and displacements. After testing, these photos were post-processed using the ARAMIS software. Due to the size of the specimen and the nature of the testing, the facet size and point distance used to analyze the speckle pattern was kept low for more localized results.

4.2.3. Results

The peak load from the MTS machine were used to calculate the modulus of rupture for all specimens. The flexural testing results based on the theoretical equation for modulus of rupture are presented in Table 4.15. Photos were captured (Figure C-1 to Figure C-29), and observations were noted before and after failure for each specimen in Appendix C. These notes and photos were intended to serve as visual documentation of any layer defects in the printed specimens and any

other relevant visual information. Additional photos (Figure D-1 to Figure D-31) at the peak load were included in Appendix D

Table 4.15: Phase II modulus of rupture results

Specimen ID	Testing Orientation	Unit Weight	Support Span (L)	Avg. Width (b)	Avg. Depth (d)	Load rate (S)	Load Rate	Peak Load	Modulus of Rupture
		pcf	*in.*	*in.*	*in.*	*psi/min*	*lbf/min*	*lbf*	*psi*
B2S1-V1	A	131.36	4	1.15	1.43	150	58.60	229.73	588
B2S1-V2	A	131.19	4	1.12	1.35	150	50.96	280.07	824
B2S2-V1	A	131.56	4	1.15	1.44	150	59.74	595.35	1495
B2S2-V2	A	134.61	4	1.16	1.39	150	55.90	585.68	1572
B2S2-V3	A	135.42	4	1.17	1.43	150	59.62	617.31	1553
B2S3-V1	A	133.72	4	1.16	1.31	150	49.49	535.14	1622
B2S3-V2	A	133.37	4	1.13	1.42	150	56.83	522.20	1378
B2S1-V3	B	129.17	4	1.47	1.12	150	45.85	235.80	771
B2S1-V4	B	131.07	4	1.44	1.11	150	44.68	350.42	1176
B2S1-V5	B	127.75	4	1.48	1.10	150	44.93	96.76	323
B2S2-V4	B	133.49	4	1.43	1.15	150	47.39	453.80	1436
B2S2-V5	B	130.43	4	1.07	1.12	150	33.54	155.14	694
B2S3-V3	B	134.05	4	1.44	1.13	150	45.88	446.00	1458
B2S3-V4	B	134.80	4	1.48	1.08	150	43.64	361.35	1242
B2S1 - H4	C	134.51	4	1.09	1.88	150	96.79	831.63	1289
B2S1 - H6	C	126.05	4	1.05	1.90	150	94.95	552.48	873
B2S3 - H1	C	133.63	4	1.09	1.92	150	100.33	1041.92	1558
B2S3 - H2	C	136.03	4	1.01	1.80	150	81.97	728.08	1332
B2S3 - H3	C	132.40	4	1.09	1.74	150	81.77	646.60	1186
B2S3 - H4	C	134.67	4	1.20	1.92	150	109.97	1071.81	1462
B2S3 - H5	C	134.29	4	1.19	1.81	150	96.79	1007.17	1561
B2S3 - H6	C	131.38	4	1.13	1.77	150	88.21	600.21	1021
B2S1 - H5	D	127.52	4	1.80	1.02	150	46.85	335.41	1074
B2S2 - H1	D	134.83	4	1.92	1.03	150	50.47	432.22	1285
B2S2 - H2	D	134.56	4	1.84	1.20	150	66.06	461.32	1047
B2S2 - H3	D	127.89	4	1.82	1.12	150	57.27	491.60	1288
B2S2 - H4	D	133.60	4	1.91	1.09	150	56.61	498.07	1320
B2S2 - H5	D	134.42	4	1.85	1.09	150	54.49	471.43	1298
B2S2 - H6	D	127.32	4	1.86	1.08	150	54.33	429.60	1186

The results with respect to each orientation are presented in Table 4.16 and Figure 4.10 from which it can be seen that orientation B had the lowest average modulus of rupture and the largest standard of deviation and range. Alternatively, orientation D was the most consistently performing group with the lowest standard of deviation and range. However, this is inclusive of all results for a given orientation and does not consider the defects induced by the printing process.

There were 7, 7, 8, and 7 data points for orientations A, B, C, and D, respectively. In Figure 4.10, the x in the shaded regions indicates the mean value. The median is indicated by the center bar in the shaded regions. The extreme values that are depicted as bars are the maximum and minimum datapoints.

Table 4.16: TPBT results with respect to testing orientation

Orientation	Average Modulus of Rupture	Standard Devation	Range
	psi	*psi*	*%*
A	1290	381	80
B	1014	395	112
C	1285	233	54
D	1214	105	22

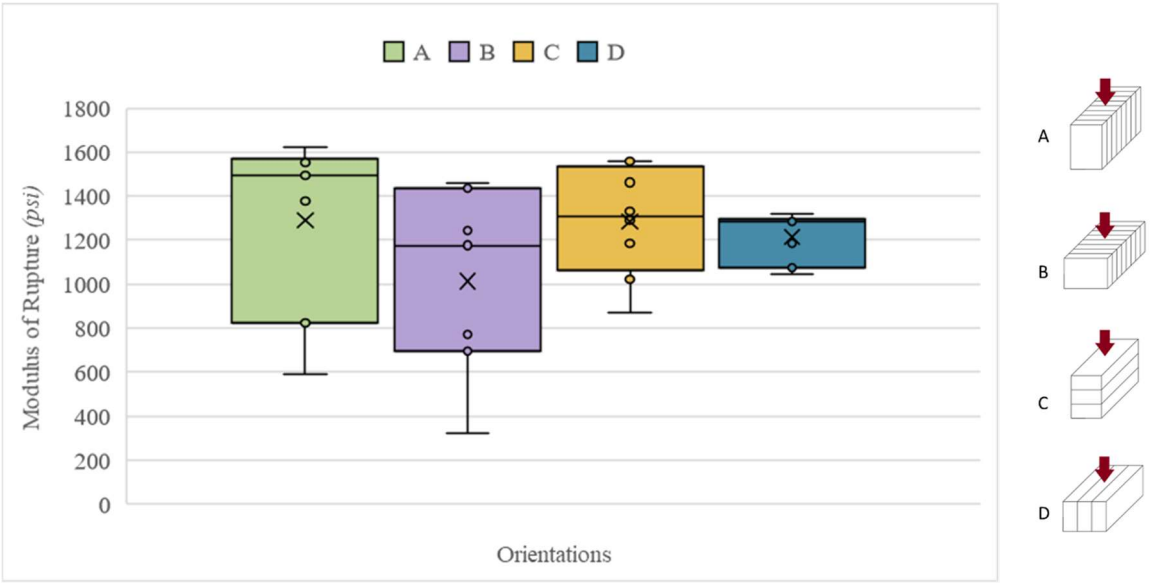

Figure 4.10: Plot of TPBT results with respect to testing orientation

Since 3DCP is not consolidated by a tamping rod or vibration after placement, printed cementitious material could have a lower unit weight than typically cast concrete or mortar. While a common unit weight for conventional concrete is 150 pcf, the mixtures in this study, as a mortar, did not include coarse aggregate. A common unit weight for mortars is on the order of 135 pcf, which agrees well with the values in Table 4.15. Assuming typical specific gravity values, the

estimated unit weight of the mortar from the mix proportions in Table 3.1 predicts 140 pcf, which assumes no air content. Figure 4.11 showed the relationship between unit weight of the printed specimens and the achieved modulus of rupture.

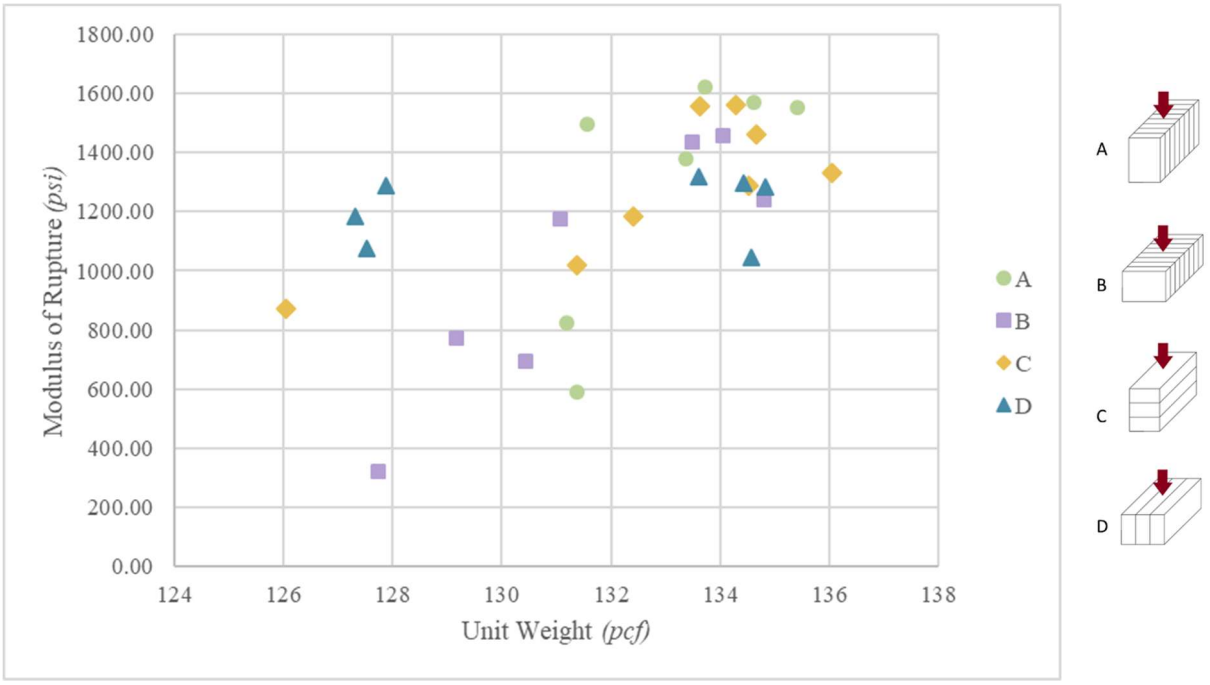

Figure 4.11: Unit weight vs. modulus of rupture with respect to testing orientation

As the unit weight of a printed specimen increased, the modulus of rupture also increased and reduced in variability. This trend makes sense considering the presence of printing defects would reduce both the unit weight and the strength. However, the trends for the individual orientations were not easily visualized from Figure 4.11, so each orientation was plotted separately in Figure 4.12 through Figure 4.15.

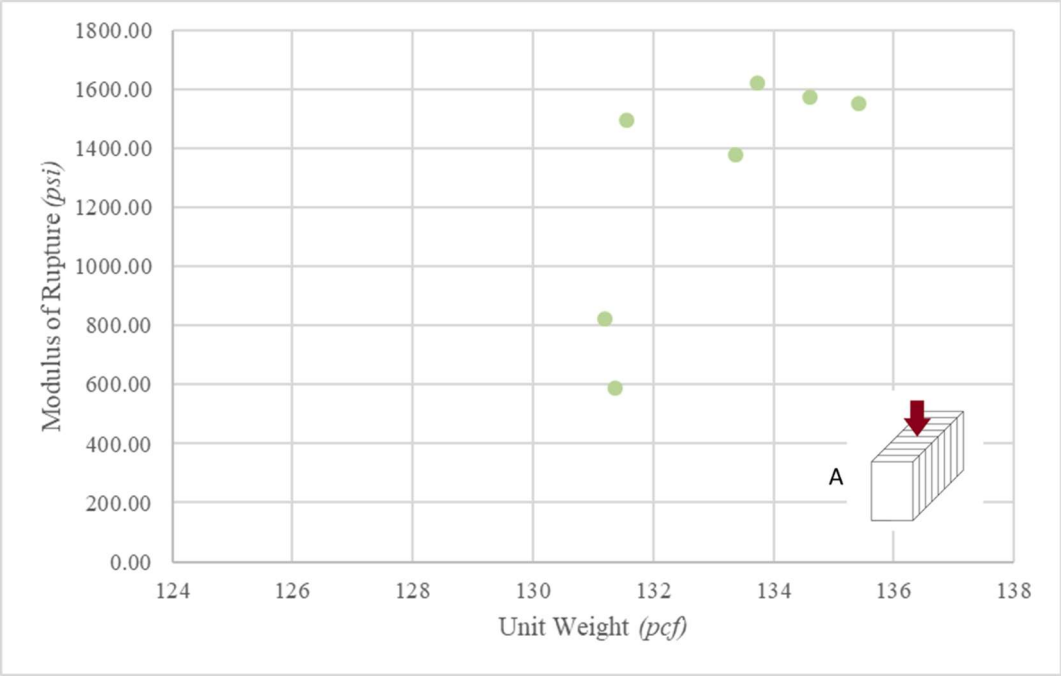

Figure 4.12: Unit weight vs. modulus of rupture for orientation A

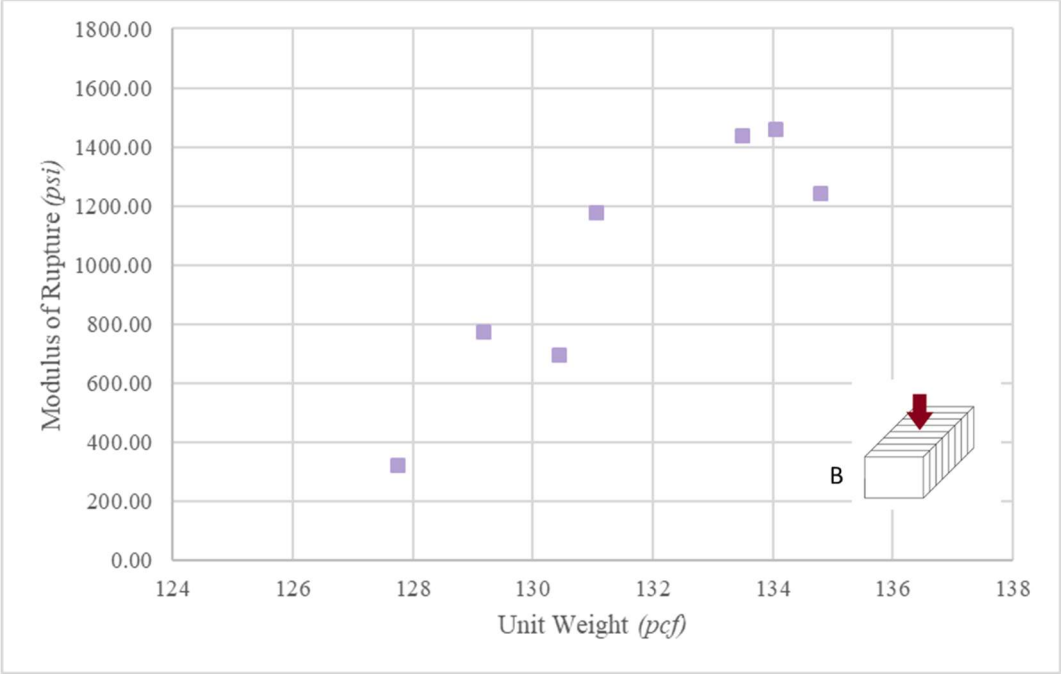

Figure 4.13: Unit weight vs. modulus of rupture for orientation B

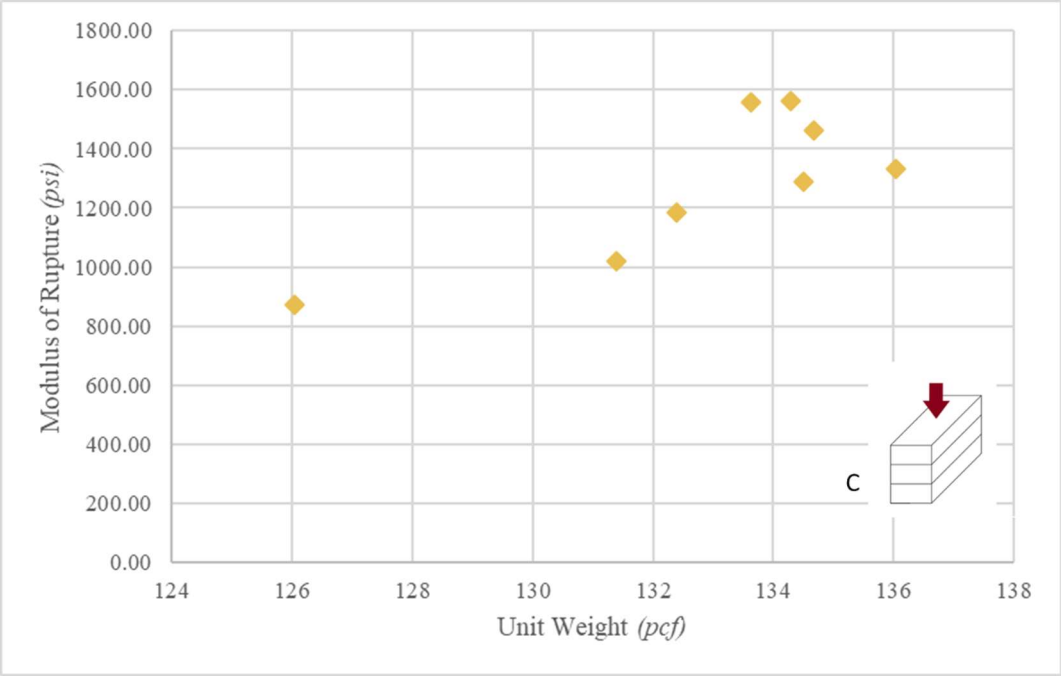

Figure 4.14: Unit weight vs. modulus of rupture for orientation C

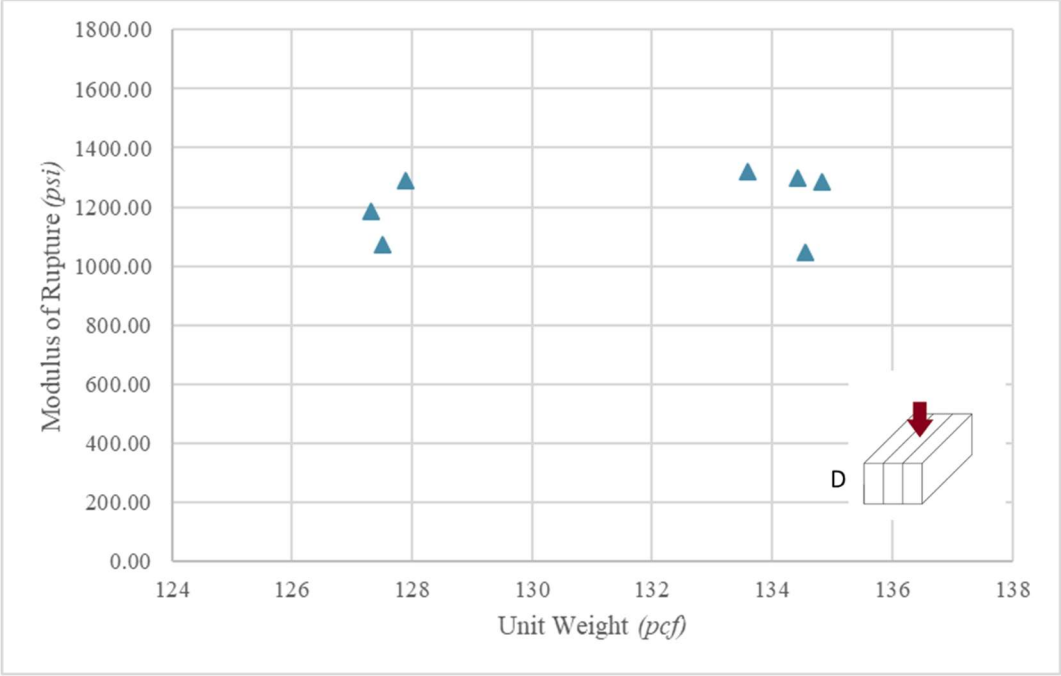

Figure 4.15: Unit weight vs. modulus of rupture for orientation D

When individually analyzing the trends for each orientation, there are more definitive relationships between unit weight and modulus of rupture. The observed lower moduli of rupture at a lower unit weights for orientations A, B, and C, are likely due to printing defects. However, other factors such as the unhydrated slag shown in Figure 3.12 from the Phase I testing could result in a lower modulus of rupture at a normal unit weight. This was corroborated by the visual observations of defects in Appendix C.

There was a strong correlation between the specimens that achieved lower moduli of rupture and had visible defects within the span length for orientations A, B, and C. At a unit weight of approximately 132 pcf, the modulus of rupture for those three orientations began to decrease and the variation between results began to increase. Orientation D demonstrated the most resilience when containing a defect: the modulus of rupture was nearly the same regardless of the unit weight (Figure 4.15). To better determine the anisotropic behavior, the results were further divided into categories for less than or greater than 132 pcf unit weight in Table 4.17. There was significant improvement for orientations A and B when separating the data points with a unit weight of less than 132 pcf. Orientations C and D did not experience a drastic change in the variation of the results, but orientation C did show an increase in average modulus of rupture unlike orientation D.

Table 4.17: Modulus of rupture categorized by orientation and unit weight

Orientation	Less than 132 pcf			Greater than 132 pcf		
	Average Modulus of Rupture	Standard Devation	Range	Average Modulus of Rupture	Standard Devation	Range
	psi	*psi*	*%*	*psi*	*psi*	*%*
A	969	384	94	1531	92	16
B	741	303	115	1379	97	16
C	947	74	16	1398	140	27
D	1182	87	18	1237	110	22

There were 3, 4, 2, and 3 specimens that were less than 132 pcf for orientations A, B, C and D, respectively. The data points that had a unit weight of 132 pcf or lower were excluded and the box and whisker plot was regenerated to demonstrate the difference in performance when the print quality is high and printed parts are "fully dense" in Figure 4.16. Therefore, there were 4, 3, 6, and 4 data points included for orientations A, B, C, and D, respectively. In Figure 4.16, the x in the shaded regions indicates the mean value. The median is indicated by the center bar in the shaded regions. The extreme values that are depicted as bars are the maximum and minimum datapoints.

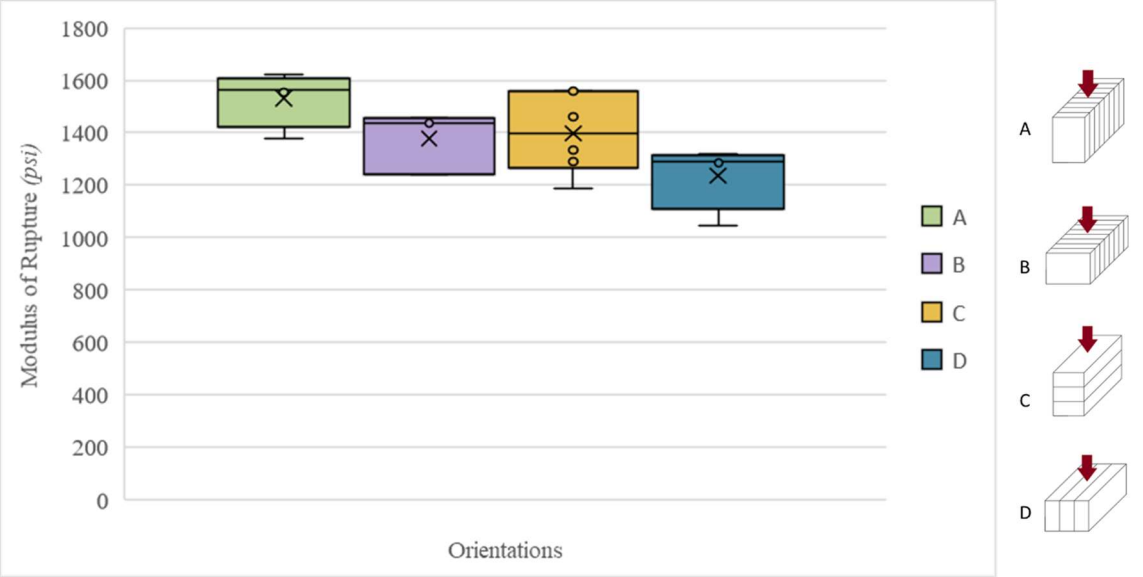

Figure 4.16: TPBT results for specimens with unit weight greater than 132 pcf

Overall, the variations were similar for all orientations; however, orientation A was able to achieve a higher modulus of rupture than B, C, and D. It was also the only orientation to be tested with the load parallel to the print path. The other three orientations were tested with the load perpendicular in some way to the print path. Orientations B and D were tested with the load perpendicular to the print path and parallel to the layer interfaces; orientation C was tested with the load perpendicular to the print path and perpendicular to the layer interfaces. This result

indicated that when the specimens were loaded in the direction of the print path, flexural strength increased.

Then, the data points that were greater 132 pcf were excluded, and a new plot investigated how poor printing and the presence of defects affected each orientation in Figure 4.17. There were 3, 4, 2, and 3 data points included for orientations A, B, C and D, respectively. In Figure 4.17, the x in the shaded regions indicates the mean value. The median is indicated by the center bar in the shaded regions. The extreme values that are depicted as bars are the maximum and minimum datapoints.

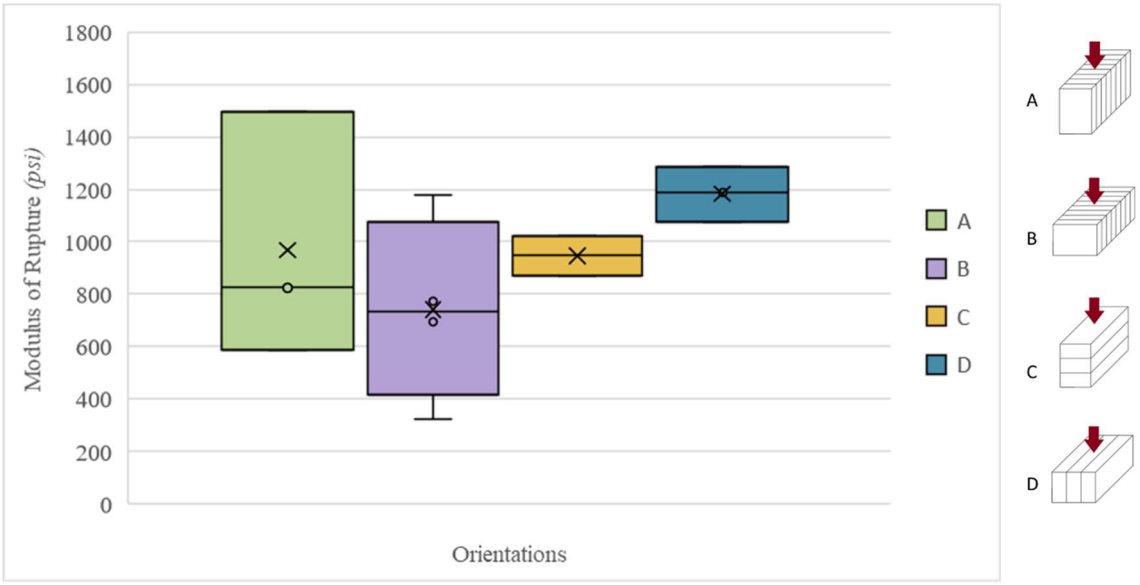

Figure 4.17: TPBT results for specimens with unit weight less than 132 pcf

Based on the results, orientations A and B experienced the most variability when defects were present. This indicated that the vertically-extracted specimens had more uncertainty in their failures than the horizontally-extracted specimens such as in orientations C and D. This behavior can be argued to be attributable to the greater redundancy in the horizontally-extracted specimen since they take advantage of the length of the layers.

To quantify which orientations were most negatively affected by the presence of defects, the range between the two averages was calculated in Table 4.18. As expected, orientation D was the least likely to be negatively affected by the presence of a defect; however, it achieved the lowest modulus of rupture for the higher quality printed specimens (γ > 132 pcf). Orientation B was most negatively affected by decreased unit weight (γ < 132 pcf) which indicated a printing defect. This result makes sense because the specimens for orientation B demonstrated a few larger defects.

Table 4.18: Summary of the range between the averages when unit weight is less than or greater than 132 pcf

Orientation	Average Modulus of Rupture (γ < 132 pcf)	Average Modulus of Rupture (γ > 132 pcf)	Range
	psi	*psi*	*%*
A	969	1531	45
B	741	1379	60
C	947	1398	38
D	1182	1237	5

It was noticed when analyzing the data and results, the DIC and the MTS readings for peak load can differ from one another. There were a few specimens for which the DIC results reported higher peak loads than the MTS reported. This was likely due to the difference in collection frequency between the two systems. The DIC system collected data from an analog input from the MTS machine during loading. This measurement was pulled into the recorded data for each "stage" or photo taken with the DIC system. The analog input that the DIC recorded was fairly close but not exactly the same as the MTS reading. The previous plots all used the peak load from the MTS program. The subsequent plots used the DIC data.

DIC was able to determine the surface strains for each stage recorded. The load and displacement in the Y direction were recorded for the crosshead (Point 1) and the location of crack

initiation just before failure (Point 2). The peak strain and strain at point 2 in the X direction were determined for every specimen. Appendix D contains the DIC exported images at the peak load for every specimen (Figure D-1 through Figure D-31). Load versus displacement plots were generated for each of the four orientations (Figure 4.18 through Figure 4.21).

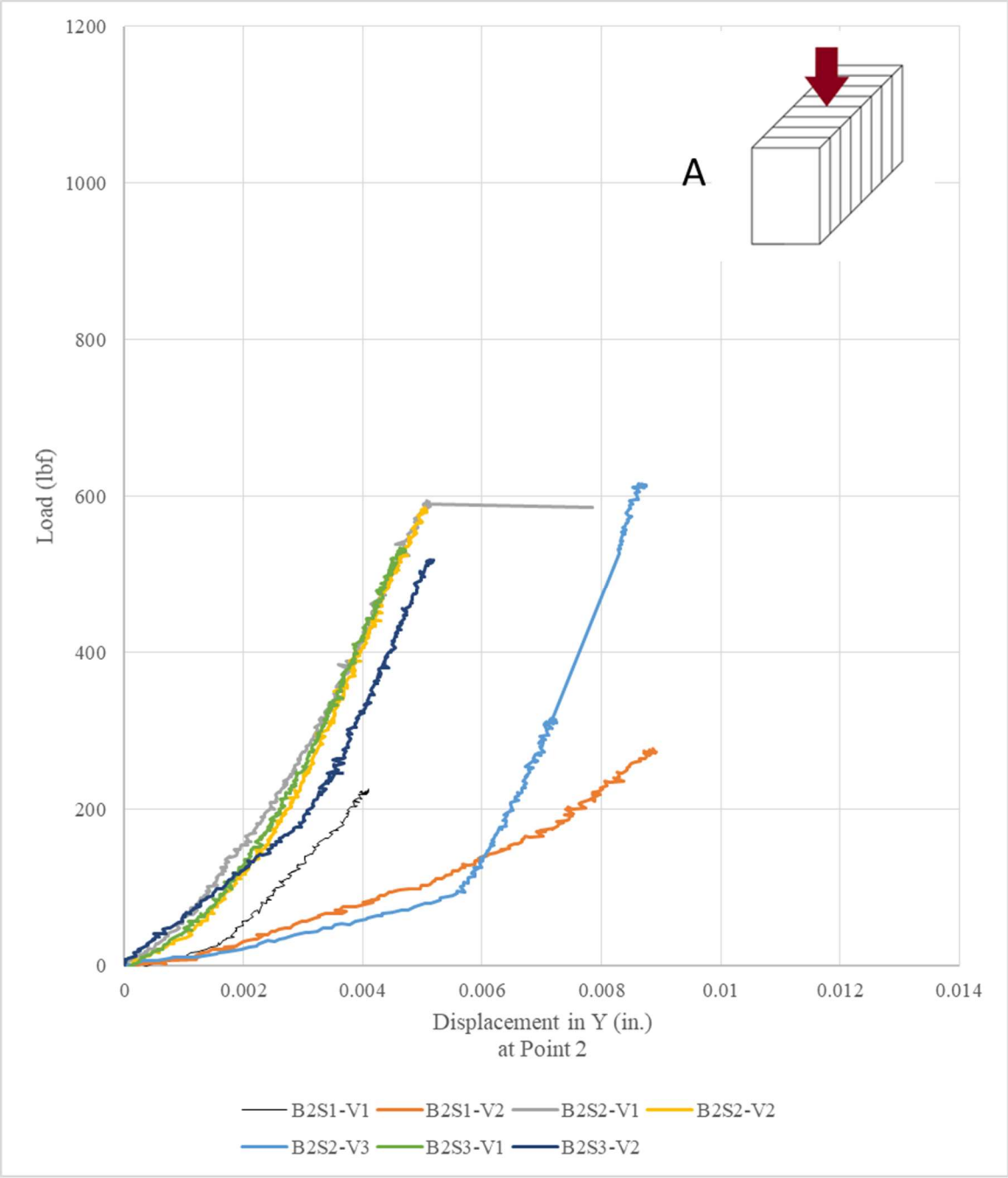

Figure 4.18: Load vs. displacement in the Y direction at Point 2 – Orientation A

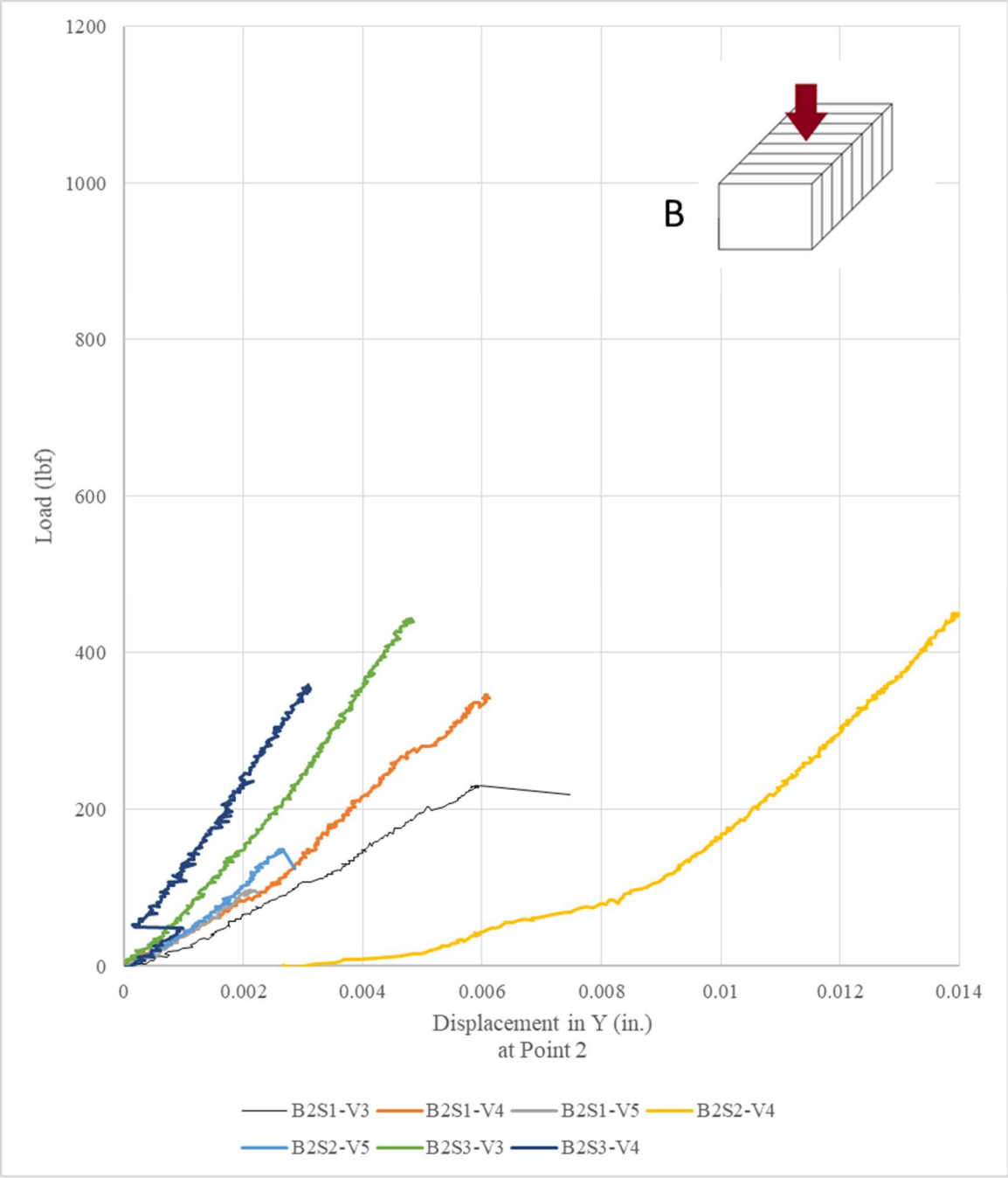

Figure 4.19: Load vs. displacement in the Y direction at Point 2 – Orientation B

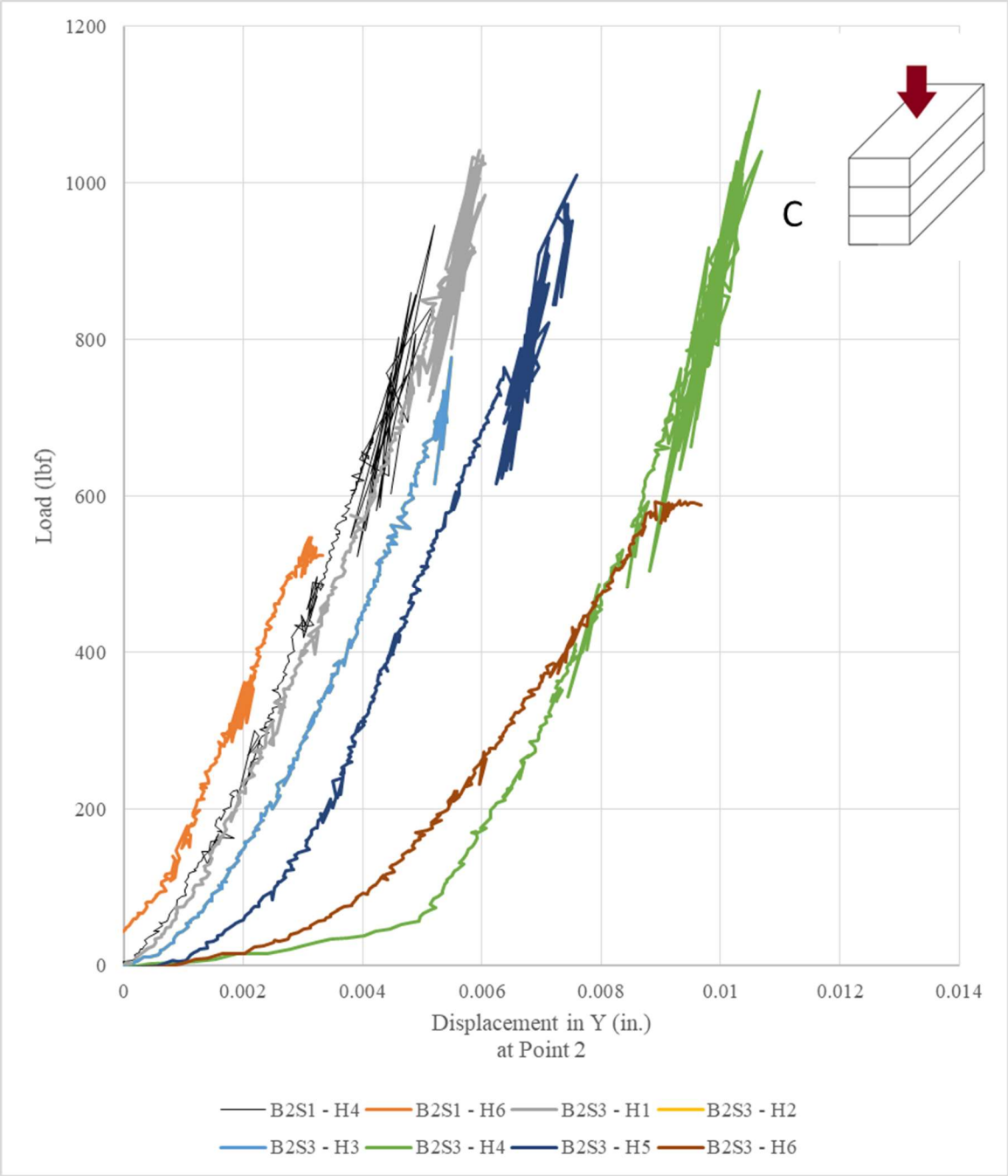

Figure 4.20: Load vs. displacement in the Y direction at Point 2 – Orientation C

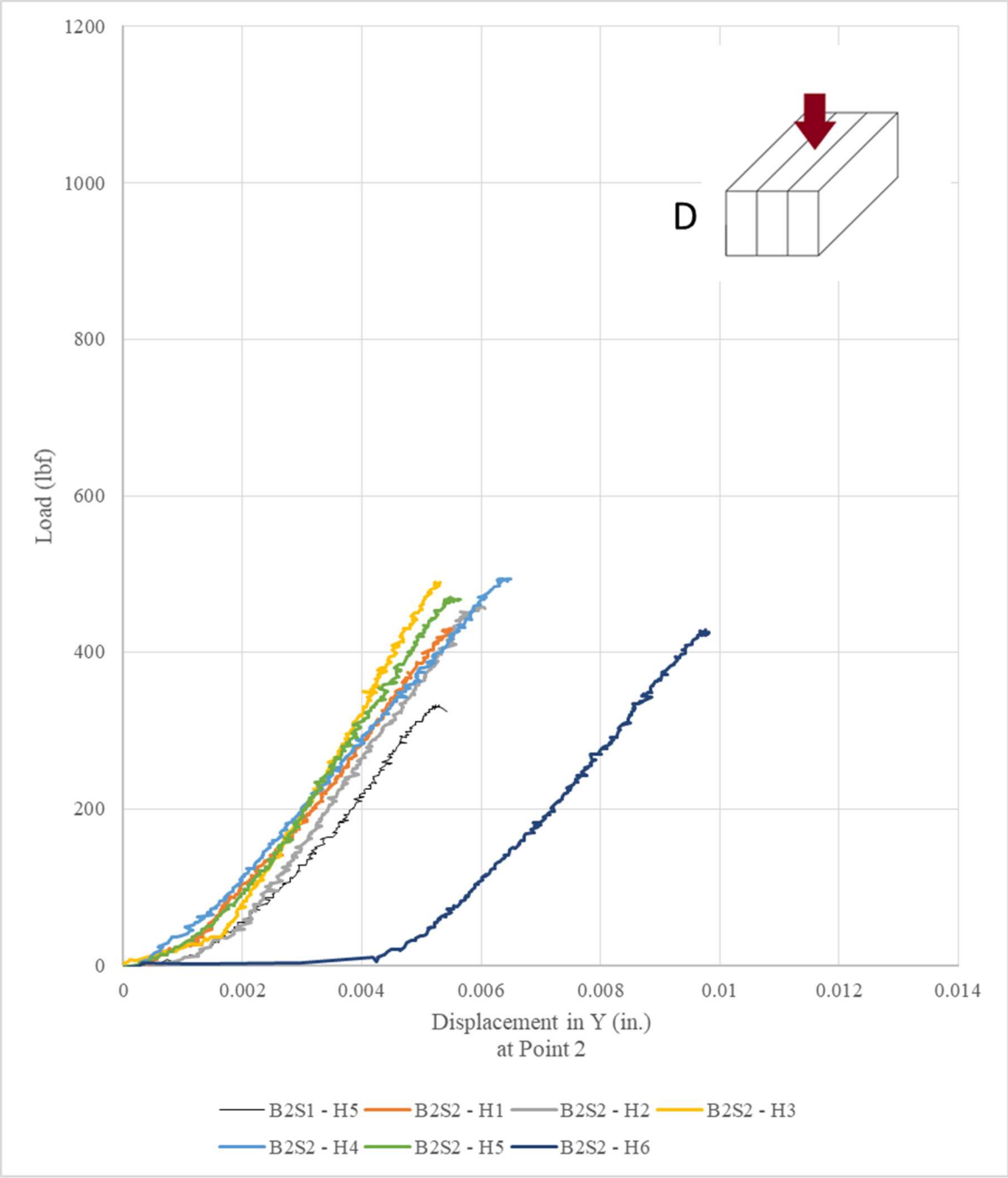

Figure 4.21: Load vs. displacement in the Y direction at Point 2 – Orientation D

Then the flexural stress versus microstrain at Point 2 was plotted for each orientation (Figure 4.22 to Figure 4.25). Some of the specimens were removed from plot(s) due to erroneous strain readings that would occur when their surfaces that were not completely smooth.

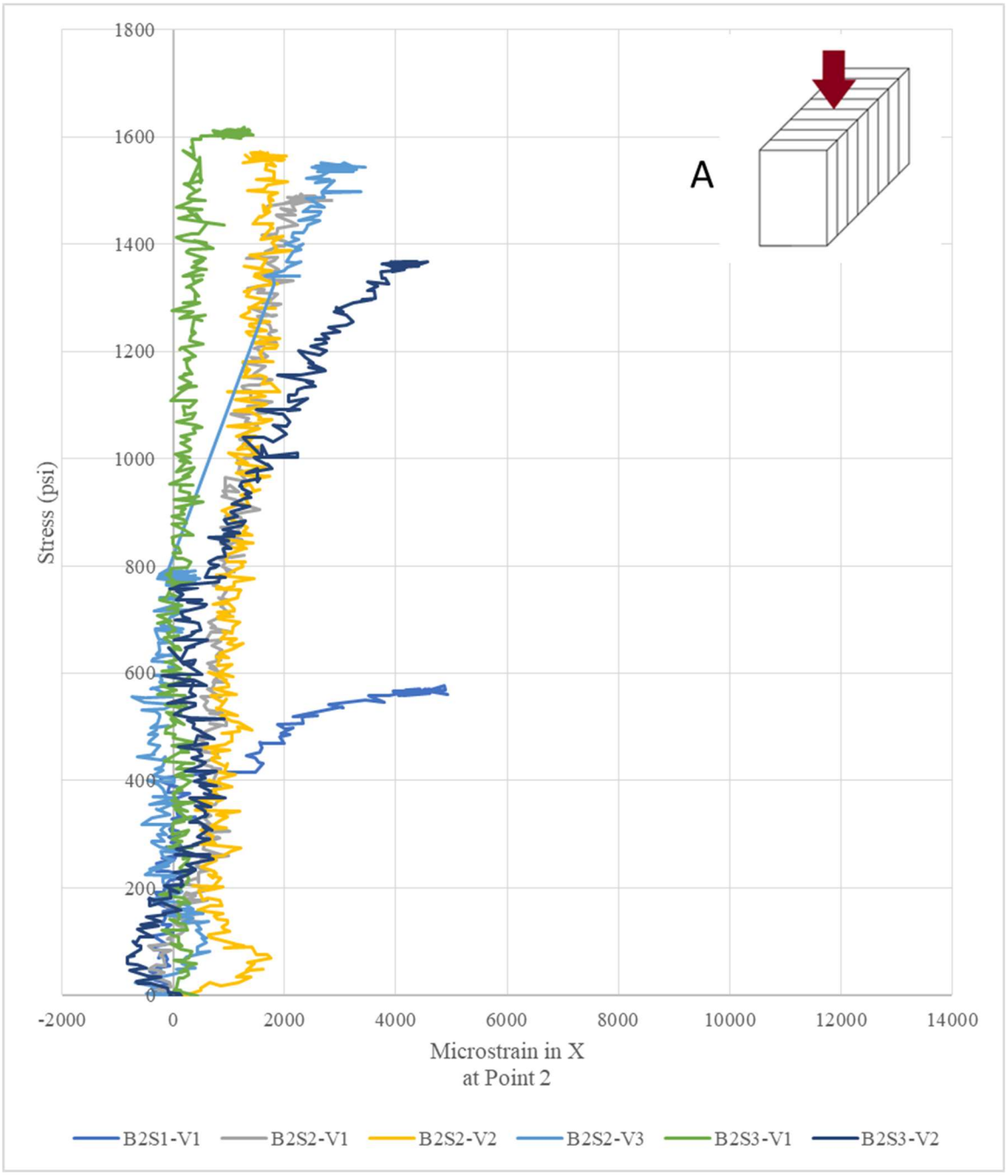

Figure 4.22: Stress vs. microstrain at Point 2 – Orientation A

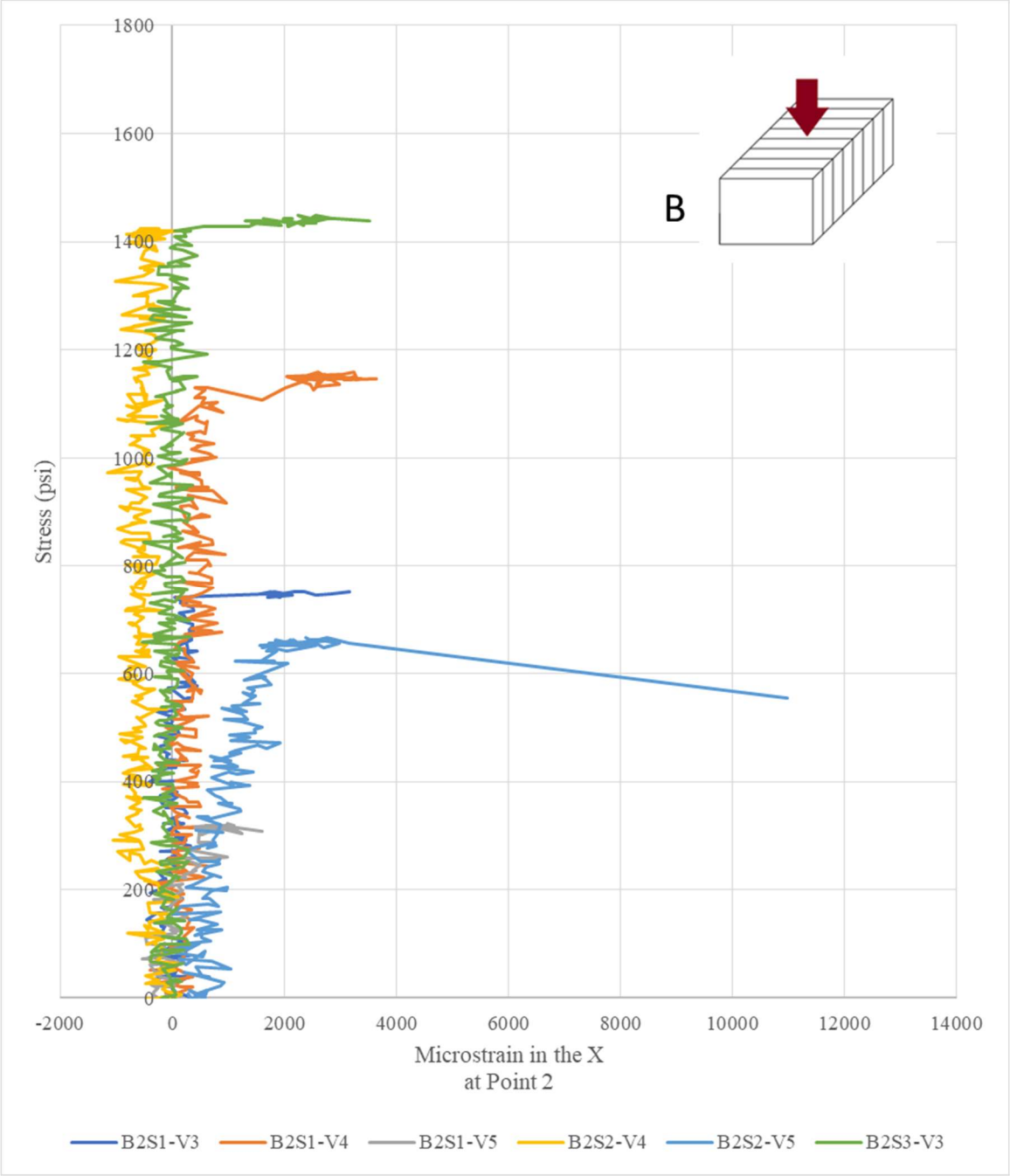

Figure 4.23: Stress vs. microstrain at Point 2 – Orientation B

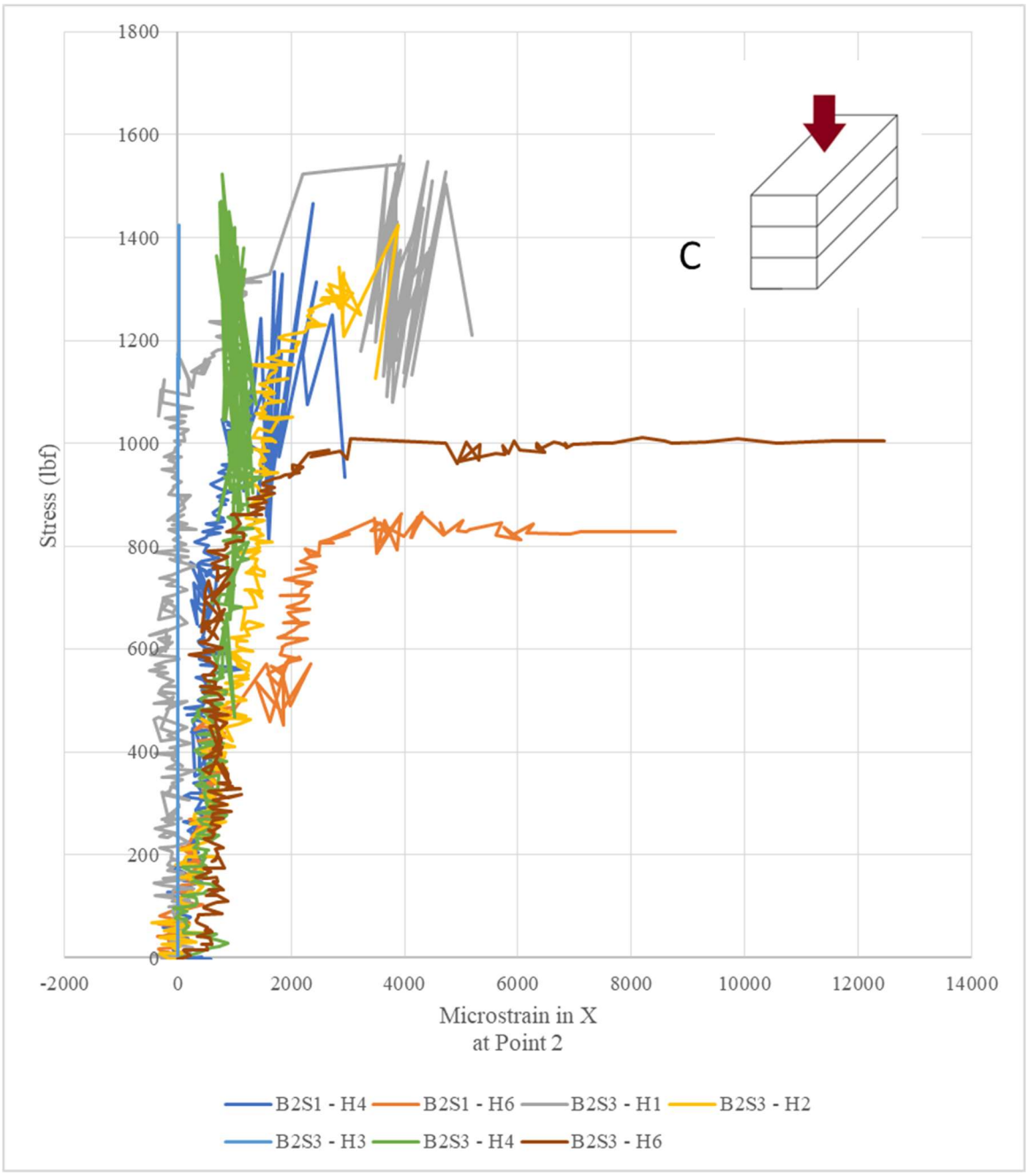

Figure 4.24: Stress vs. microstrain at Point 2 – Orientation C

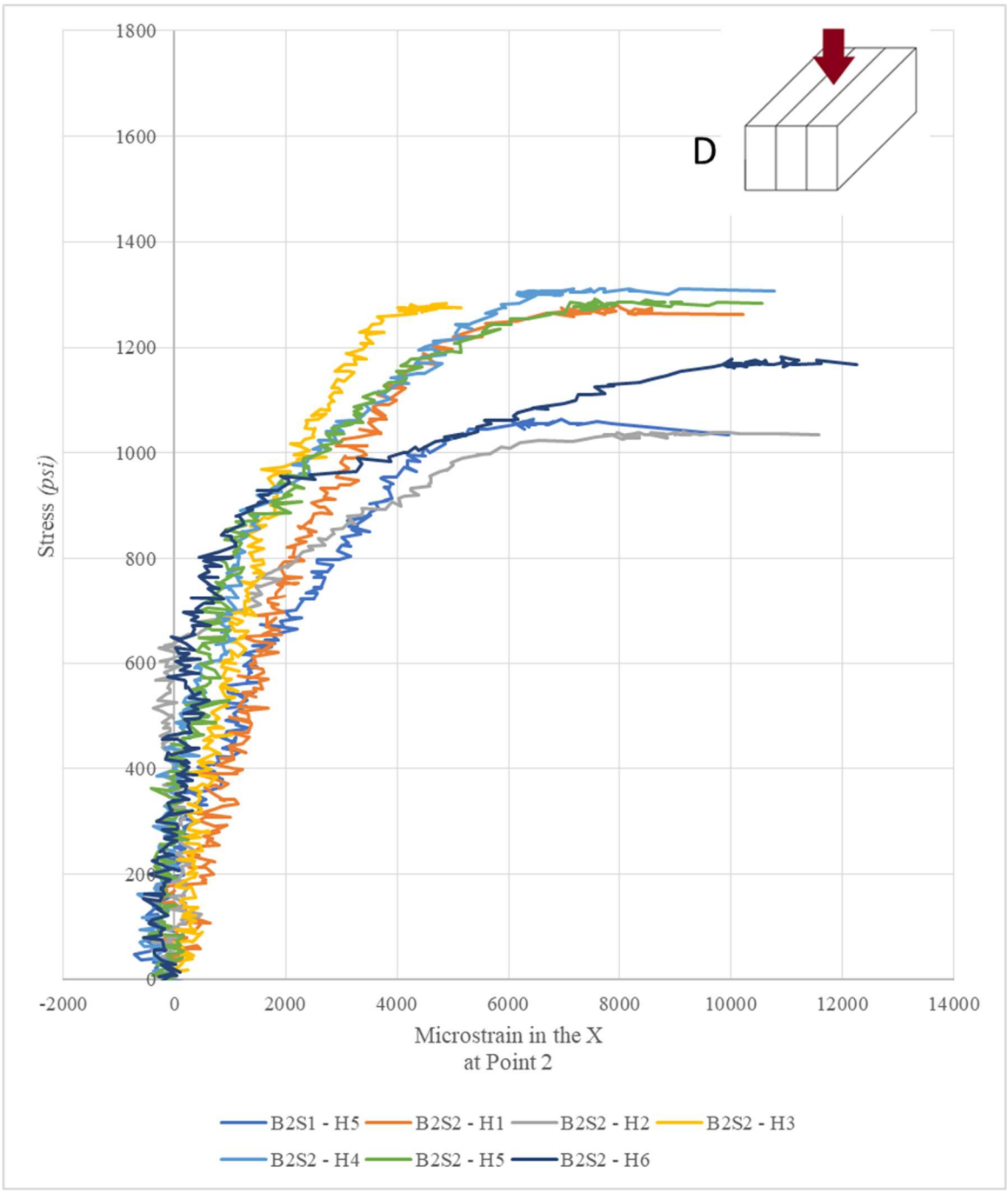

Figure 4.25: Stress vs. microstrain at Point 2 – Orientation D

The difference in the behavior of the stress-strain relationships seen between the different orientations indicated the type of failure experienced. For example, orientations A and B were loaded at a layer interface and experienced brittle failures. Alternatively, orientations C and D experienced quasi-brittle failures. The ultimate strain for traditionally-cast reinforced concrete

used in design is 0.003 or 0.0038, depending on the model used [97]. Orientation D (Figure 4.25) performed much like traditionally cast concrete would and the shape of the curves are clearly defined but were able to achieve higher ultimate strains. Working backwards from there, orientation C (Figure 4.24) showed sporadic differences between the stress-strain relationship for different specimens within the group; some showed significant strain development, but some showed very little. Orientation B shows strain development at the very end of loading (Figure 4.23). Orientation A had the most brittle failures of all (Figure 4.22).

Orientation A and B are loaded at interfaces which are the "weak link" of the composite. Cracks can propagate quickly and easily along the interface plane leading to the observed brittle behavior, thus this is not a material property but rather a geometry-specific property due to anisotropy. Alternatively, orientations C and D are not tested directly at an interface and are oriented such that the results are more representative of actual mortar material properties – thus the behavior is quasi-brittle. Based on this argument, orientation C should give the most reasonable material flexural strength since it relies on a single, continuous layer of concrete on its tension face.

The flexural modulus of elasticity was then calculated two ways for every specimen (if equation was applicable). The first method of calculating the flexural modulus of elasticity was by using the linear region of the stress-strain relationship. The second method was by using the deflection equation:

$$\Delta = \frac{PL^3}{48EI} \tag{6}$$

where Δ is the mid-span deflection, P is the load, L is the span length, E is the modulus of elasticity, and I is the moment of inertia. Note that Equations 6 is *only* applicable at the mid-span. The results are summarized in Table 4.19.

Table 4.19: Flexural modulus of elasticity results

Specimen name	Testing Orientation	Flexural Elastic Modulus (based on stress-strain)	Flexural Elastic Modulus (based on deflection)	Failure at Mid-Span?	Unit Weight	
		psi	*psi*		*pcf*	
B2S1-V1	A	34921	n/a	no	131.4	< 132
B2S1-V2	A	n/a	n/a	no	131.2	< 132
B2S2-V1	A	737638	661883	yes	131.6	< 132
B2S2-V2	A	957581	827640	yes	134.6	
B2S2-V3	A	n/a	885258	yes	135.4	
B2S3-V1	A	1014801	n/a	no	133.7	
B2S3-V2	A	140871	838753	yes	133.4	
B2S1-V3	B	399094	n/a	no	129.2	< 132
B2S1-V4	B	416351	n/a	no	131.1	< 132
B2S1-V5	B	223373	n/a	no	127.7	< 132
B2S2-V4	B	n/a	502278	yes	133.5	
B2S2-V5	B	329504	n/a	no	130.4	< 132
B2S3-V3	B	392981	799730	yes	134.0	
B2S3-V4	B	87679	936526	yes	134.8	
B2S1 - H4	C	541651	448877	yes	134.5	
B2S1 - H6	C	221832	n/a	no	126.0	< 132
B2S3 - H1	C	n/a	403357	yes	133.6	
B2S3 - H2	C	423621	472604	yes	136.0	
B2S3 - H3	C	n/a	442214	yes	132.4	
B2S3 - H4	C	929914	389091	yes	134.7	
B2S3 - H5	C	n/a	427597	yes	134.3	
B2S3 - H6	C	301257	266363	yes	131.4	< 132
B2S1 - H5	D	209205	n/a	no	127.5	<132
B2S2 - H1	D	295807	740374	yes	134.8	
B2S2 - H2	D	n/a	526531	yes	134.6	
B2S2 - H3	D	351060	801159	yes	127.9	<132
B2S2 - H4	D	425247	566336	yes	133.6	
B2S2 - H5	D	486429	743706	yes	134.4	
B2S2 - H6	D	600373	588512	yes	127.3	<132

There is some agreement between the flexural modulus when calculated using the two different methods, but it is not consistent. For example, specimen B2S3-H2 failed at the midspan, so the deflection equation is applicable; the flexural elastic modulus based on stress-strain was 423621 psi whereas based on deflection it was 472604 psi. However, when looking at specimen B2S3-H4 which also failed at midspan, the flexural elastic modulus based on stress-strain was 929914 psi whereas based on deflection it was 389091 psi. The deflection equation assumes a linear elastic material which may not be applicable to 3DCP based on the effect of the layers on

deflection. Furthermore, the presence of defects may also influence these calculations, especially if the defects act as localized stress concentrations. Finally, some of the DIC was somewhat noisy, which may also influence the results. As the surface of the AM specimens was not always flat or smooth, often owing to the presence of defects, the DIC calculations may not be reliable.

4.2.4. Conclusions

Applying the loading rate from ASTM C293 provided more consistent loading and comparisons between the extracted 3DCP specimens. Using the three-point bending tests allowed for a good comparison between the four different orientations which demonstrated anisotropic behavior. This anisotropic behavior was corroborated with the DIC data showing the stress-strain relationships. Orientation A and B were brittle while orientations C and D were quasi-brittle. Furthermore, it can be seen in the differences in achieved modulus of rupture. For example, the highest achieved average modulus of rupture for the denser specimens ($\gamma > 132$ pcf) was for orientation A at 1531 psi and the lowest at 1237 psi for orientation D. For a one-tailed two sample t-test assuming unequal variances with $p=0.006$, the means ($\gamma > 132$ pcf) for orientations A and D are statistically different thus demonstrating anisotropic behavior.

The equation using deflection to calculate flexural modulus of rupture may not be applicable to 3DCP since it does not behave as a linear elastic material. The agreement based on the flexural elastic modulus determined from the stress-strain relationship and determined from the deflection equation (eqn. 6) is not consistent (Table 4.19). This difference could also be due to the "noise" in the DIC data collection and strains recorded (Figure 4.22 through Figure 4.25).

Unit weight can be a good indicator of reduction of capacity for most cases (except for D). A required minimum unit weight could ensure printed parts are "fully dense" and avoid defects.

This is important because predictability in performance is important, and denser printed specimens performed more consistently and reliably than the less dense specimens. For this study, using a minimum unity weight of 132 pcf was able to differentiate between specimens that had significant defects that correlated well with the observations and notes prior to testing. For example, between the group with unit weights less than 132 pcf and the group with unit weights greater than 132 pcf, there was an 86 percent increase in the modulus of rupture and a 68 percent decrease in the standard deviation for orientation B. This further demonstrated a need for QA/QC measures to be implemented; however, 132 pcf may not be the same cutoff point for other mortars, and it may be subject to change for each different 3DCP system based on extrusion technique.

The higher modulus of rupture achieved for orientation A could indicate that loading parallel to the print path can increase the flexural resistance; however, this could be due to the applied pressure from extrusion causing better mechanical interlock at the layer interface or porosity in filaments from elongation/compression from printing. This may not still be true for concrete that printed by "placing" (i.e. no pressure applied during extrusion).

5. DISCUSSION AND CONCLUSIONS

Quality assurance and quality control methods via standard testing methods are of utmost importance to ensure the safety, health, and welfare of the public and tackle the outlined challenges (Figure 2.5) as 3DCP emerges in civil infrastructure applications. This thesis aimed to better implement existing ASTM standards to characterize 3DCP and gather better information on how to tackle these challenges.

This project applied existing ASTM standards for fresh mix mortars to measure setting time, flow, and early compressive strength as qualitative indicators of printability, pumpability, and buildability. Furthermore, these tests are relatively affordable, are not labor-intensive, and are fairly straightforward to complete. As mentioned previously, setting time could be correlated to yield stress [68], and flow could be correlated to viscosity [69]. A relationship between these test methods and open time could predict how different mortars will perform for potential 3D printing applications; however, these tests would need to first be applied to printing process to be able to suggest recommended values.

The need for properly accounting for the moisture content, absorption, and sand type in the mix design was shown in the differences between results for Group 1 and Group 2. The results for setting time and compressive strength demonstrated that there was less variability in the properties when the moisture condition of the aggregate was measured and accounted. For example, this was demonstrated by a 55 percent decrease in the standard deviation for early compressive strength for natural sand and a 63 percent decrease for manufactured sand after properly accounting for moisture. Similarly, the setting time for natural sand had a 67 percent reduction in the standard deviation between Groups 1 and 2, and the manufactured sand had a 71 percent reduction. Therefore, *it is recommended that mixtures used in 3D printing of cementitious composites should*

design and accommodate the moisture condition of the aggregate to optimize the predictability of the fresh and early-age properties.

Existing ASTM standards also were applied to the flexural testing; ASTM C348 was modified and applied to testing orientations A and B. Based on the preliminary results from Phase I, the load rate was determined to be too high and more information was needed about how the load was distributed or transferred between layers. Orientation A and B each achieved a mean modulus of rupture (when removing the defective specimen) of 907 psi and 1146 psi, respectively. The standard deviation for orientation A and B was 223 psi and 147 psi, respectively. A two sample one-tailed t-test with unequal variances yielded $p = 0.135$ indicating that the means were not statistically different at 95% confidence. However, further testing was necessary since the loading rate needed to be revised.

Applying the loading rate from ASTM C293 provided more consistent loading and comparisons between the extracted 3DCP specimens. Using unit weight to filter the data allowed for simple exclusion of specimens with significant defects induced by the printing process. Unit weight was shown to be a good indicator of reduction of capacity for most cases (except for D) which can be valuable when determining how to effectively model, design, and inspect 3D printed structures in the future. Based on the results, a required minimum unit weight could ensure printed parts are "fully dense" and avoid defects. For this study, using a minimum unity weight of 132 pcf was able to qualitatively differentiate between specimens that had significant defects that correlated well with the observations and notes prior to testing. For example, between the group with unit weights less than 132 pcf and the group with unit weights greater than 132 pcf, there was an 86 percent increase in the modulus of rupture and a 68 percent decrease in the standard deviation for orientation B. This further demonstrated a need for QA/QC measures to be implemented;

however, 132 pcf may not be the same cutoff point for other mortars, and it may be subject to change for each different 3DCP system based on extrusion technique.

Furthermore, using the three-point bending demonstrated anisotropic behavior among the different orientations. For example, the highest achieved average modulus of rupture for the denser specimens ($\gamma > 132$ pcf) was for orientation A at 1531 psi and the lowest at 1237 psi for orientation D. For a one-tailed two sample t-test assuming unequal variances with $p=0.006$, the means ($\gamma >$ 132 pcf) for orientations A and D are statistically different thus demonstrating anisotropic behavior. It could be argued that orientation A performed the best when excluding defects from results because it was the only orientation loaded parallel to the print path. The higher modulus of rupture achieved for orientation A could indicate that loading parallel to the print path can increase the flexural resistance; however, this could be due to the applied pressure from extrusion causing better mechanical interlock at the layer interface or porosity in filaments from elongation/compression from printing. This may not still be true for concrete that printed by "placing" (*i.e.* no pressure applied during extrusion).

Orientation D was least affected by defects because it had range of 5 percent between the mean modulus of rupture for the two-unit weight categories. The other orientations reached much higher ranges (Table 4.18). It could be argued that this was because the layers for orientation D were not stacked; they were side-by-side which allowed them to act more independently from one another with some redundancy. This could suggest that failure is less critical when the loading is distributed among other layers and the capacity is not reliant on the strength of a single interface.

The observed anisotropic behavior was corroborated with the DIC data showing the stress-strain relationships. Orientation A and B experienced brittle behavior while orientations C and D experienced quasi-brittle behavior. The observed lower strain development for higher achieved

modulus of rupture could be indicative of the failure type such as brittle failure at the interfaces for orientations A (Figure 4.22) and B (Figure 4.23). *For implementation of 3D printed concrete structures, it is highly recommended that the design is a function of loading orientation due to the anisotropic properties of the composite*.

6. FUTURE WORK

Based on the results of the testing from this project, there are several suggestions and recommendations for improving these methods for future work.

- Increase span length for future testing to ensure the applicability of assuming the Euler-Bernoulli beam theory equation (no shear effects included). The length was limited by the printed height in this study. Alternatively, some other flexural strength test would need to be developed for 3DCP that can accommodate this issue.
- Use DIC to investigate slip between layers and inform how to model the materials.
- Use DIC with the same three-point bending setup but with fracture testing to monitor crack initiation and crack propagation.
- Consider varying printing parameters and their effects such as how the interface bond is affected by pressure applied during extrusion or how the modulus of rupture changes for varying aspect ratios of filaments.
- Determine how fiber inclusion affects anisotropic properties. Since literature suggests that layer bond may decrease [50] with the inclusion of fibers, investigate how that affects the resistance to defects for orientations A through D. Based on the literature, it is predicted that A and B will perform similarly or worse than for plain mortar, but C and D will improve
- Compare three-point bending tests and four-point bending tests. The three-point bending test setup in this study imposed a maximum moment at a specific point, but failure patterns when there is a maximum moment zone should be explored. How do cracks initiate when there is a maximum moment zone, and how does that affect the criticality of defects?

- Create a database to compile published results with information about printing methods including printing parameters, AM method (i.e. extrusion, binder jetting), specimen preparation and geometry, test method, etc.
- Develop (or modify existing) ASTM standards specific to 3DCP applications including fresh mix properties and hardened material properties. These testing standards should provide QA/QC measures to ensure predictability of the performance of 3D printed structures.

REFERENCES

1. ASTM F2792-12a. *Standard Terminology for Additive Manufacturing Technologies (Withdrawn 2015)*. ASTM International. https://doi.org/10.1520/F2792-12A
2. World Trade Organization Technical Barriers to Trade (TBT) Committee. (2015). *Standard Terminology for Additive Manufacturing – General Principles – Terminology*. ISO/ASTM International. https://doi.org/10.1520/ISOASTM52900-15
3. Kazemian, A., Yuan, X., Cochran, E., & Khoshnevis, B. (2017). Cementitious materials for construction-scale 3D printing: Laboratory testing of fresh printing mixture. *Construction and Building Materials*, *145*, 639–647. http://dx.doi.org/10.1016/j.conbuildmat.2017.04.015
4. Ma, G., & Wang, L. (2018). A critical review of preparation design and workability measurement of concrete material for largescale 3D printing. *Frontiers of Structural and Civil Engineering*, *12*(3), 382–400. https://doi.org/10.1007/s11709-017-0430-x
5. Buswell, R. A., Leal de Silva, W. R., Jones, S. Z., & Dirrenberger, J. (2018). 3D printing using concrete extrusion: A roadmap for research. *Cement and Concrete Research*, *112*, 37–49. https://doi.org/10.1016/j.cemconres.2018.05.006
6. Wangler, T., Lloret, E., Reiter, L., Hack, N., Gramazio, F., Kohler, M., Bernhard, M., Dillenburger, B., Buchli, J., Roussel, N., Flatt, R. (2016). Digital Concrete: Opportunities and Challenges. *RILEM Technical Letters*, *1*, 67. https://doi.org/10.21809/rilemtechlett.2016.16
7. Gosselin, C., Duballet, R., Roux, P., Gaudillière, N., Dirrenberger, J., & Morel, P. (2016). Large-scale 3D printing of ultra-high performance concrete – a new processing route for architects and builders. *Materials and Design*, *100*, 102–109. http://dx.doi.org/10.1016/j.matdes.2016.03.097

8. Lim, S., Buswell, R. A., Le, T. T., Austin, S. A., Gibb, A. G. F., & Thorpe, T. (2012). Developments in construction-scale additive manufacturing processes. *Automation in Construction*, *21*, 262–268. https://doi.org/10.1016/j.autcon.2011.06.010

9. Khoshnevis, B. (2004). Automated construction by contour crafting—related robotics and information technologies. *Automation in Construction*, *13*(1), 5–19. https://doi.org/10.1016/j.autcon.2003.08.012

10. Khoshnevis, B., & Dutton, R. (1998). Innovative Rapid Prototyping Process Makes Large Sized, Smooth Surfaced Complex Shapes in a Wide Variety of Materials. *Materials Technology*, *13*(2), 53–56. https://doi.org/10.1080/10667857.1998.11752766

11. Pegna, J. (1997). Exploratory investigation of solid freeform construction. *Automation in Construction*, *5*(5), 427–437. https://doi.org/10.1016/S0926-5805(96)00166-5

12. Khoshnevis, B. (1999). Contour Crafting - State of Development. In *Solid Freeform Fabrication Symposium* (pp. 743–750).

13. Zhang, J., & Khoshnevis, B. (2013). Optimal machine operation planning for construction by Contour Crafting. *Automation in Construction*, *29*, 50–67. https://doi.org/10.1016/j.autcon.2012.08.006

14. Buswell, R. A., Soar, R. C., Gibb, A. G. F., & Thorpe, A. (2007). Freeform Construction: Mega-scale Rapid Manufacturing for construction. *Automation in Construction*, *16*(2), 224–231. https://doi.org/10.1016/j.autcon.2006.05.002

15. Le, T. T., Austin, S. A., Lim, S., Buswell, R. A., Law, R., Gibb, A. G. F., & Thorpe, T. (2012). Hardened properties of high-performance printing concrete. *Cement and Concrete Research*, *42*(3), 558–566. https://doi.org/10.1016/j.cemconres.2011.12.003

16. Le, T. T., Austin, S. A., Lim, S., Buswell, R. A., Gibb, A. G. F., & Thorpe, T. (2012). Mix design and fresh properties for high-performance printing concrete. *Materials and Structures*, *45*(8), 1221–1232. https://doi.org/10.1617/s11527-012-9828-z

17. Gagg, C. R. (2014). Cement and concrete as an engineering material: An historic appraisal and case study analysis. *Engineering Failure Analysis*, *40*, 114–140. https://doi.org/10.1016/j.engfailanal.2014.02.004

18. Wangler, T., Roussel, N., Bos, F. P., Salet, T. A. M., & Flatt, R. J. (2019). Digital Concrete: A Review. *Cement and Concrete Research*, *123*, 105780. https://doi.org/10.1016/j.cemconres.2019.105780

19. Andrew, R. M. (2018). Global CO2 emissions from cement production. *Earth Syst. Sci. Data, 10*, 195–217, 2018 https://doi.org/10.5194/essd-10-195-2018

20. Environmental Sciences Division, O. R. N. L. (2010). Global, Regional, and National Fossil-Fuel CO2 Emissions. Carbon Dioxide Information Analysis Center (CDIAC). https://doi.org/10.3334/CDIAC/00001_V2010

21. Bos, F., Wolfs, R., Ahmed, Z., & Salet, T. (2016). Additive manufacturing of concrete in construction: potentials and challenges of 3D concrete printing. *Virtual and Physical Prototyping*, *11*(3), 209–205. https://doi.org/10.1080/17452759.2016.1209867

22. Chen, Y., Veer, F., & Çopuro, O. (2017). A critical review of 3D concrete printing as a low CO2 concrete approach. *Heron*, *62*(3), 167–194.

23. Sanjayan, J., Nazari, A., & Nematollahi, B. (2019). *3D concrete printing technology* (1st edition.). Waltham, MA: Elsevier.

24. Zhang, J. (2019). A review of the current progress and application of 3D printed concrete. *Composites Part A*, *125*(105533), 13. https://doi.org/10.1016/j.compositesa.2019.105533

25. Wu, P., Wang, J., & Wang, X. (2016). A critical review of the use of 3-D printing in the construction industry. *Automation in Construction*, *68*, 21–31. http://dx.doi.org/10.1016/j.autcon.2016.04.005

26. Wangler, T., & Flatt, R. J. (Eds.). (2019). *First RILEM International Conference on Concrete and Digital Fabrication – Digital Concrete 2018* (Vol. 19). Cham: Springer International Publishing. https://doi.org/10.1007/978-3-319-99519-9

27. Shakor, P., Nejadi, S., Paul, G., & Malek, S. (2019). Review of Emerging Additive Manufacturing Technologies in 3D Printing of Cementitious Materials in the Construction Industry. *Frontiers in Built Environment*, *4*, 17. https://doi.org/10.3389/fbuil.2018.00085

28. Panda, B., Tay, Y. W. D., Paul, S. C., & Tan, M. J. (2018). Current challenges and future potential of 3D concrete printing: Aktuelle Herausforderungen und Zukunftspotenziale des 3D-Druckens bei Beton. *Materialwissenschaft und Werkstofftechnik*, *49*(5), 666–673. https://doi.org/10.1002/mawe.201700279

29. Ngo, T. D., Kashani, A., Imbalzano, G., Nguyen, K. T. Q., & Hui, D. (2018). Additive manufacturing (3D printing): A review of materials, methods, applications and challenges. *Composites Part B: Engineering*, *143*, 172–196. https://doi.org/10.1016/j.compositesb.2018.02.012

30. Lu, B., Weng, Y., Li, M., Qian, Y., Fai Leong, K., & Jen Tan, M. (2019). A systematical review of 3D printable cementitious materials. *Construction and Building Materials*, *207*, 477–490. https://doi.org/10.1016/j.conbuildmat.2019.02.144

31. Liu, J., & Li, G. (2018). Research on the Development of 3D Printing Construction Industry Based on Diamond Model. In *ICCREM* (pp. 164–176). Presented at the International

Conference on Construction and Real Estate Management. https://doi.org/10.1061/9780784481721.020

32. Lee, D., Kim, H., Sim, J., Lee, D., Cho, H., & Hong, D. (2019). Trends in 3D Printing Technology for Construction Automation Using Text Mining. *International Journal of Precision Engineering and Manufacturing*, *20*, 871–882. https://doi.org/10.1007/s12541-019-00117-w

33. Jassmi, H. A., Najjar, F. A., & Mourad, A.-H. I. (2018). Large-Scale 3D Printing: The Way Forward. In *IOP Conference Series: Materials Science and Engineering* (Vol. 324, p. 16). https://doi.org/10.1088/1757-899x/324/1/012088

34. Hamidi, F., & Aslani, F. (2019). Additive manufacturing of cementitious composites: Materials, methods, potentials, and challenges. *Construction and Building Materials*, *218*, 582–609. https://doi.org/10.1016/j.conbuildmat.2019.05.140

35. Camacho, D. D., Clayton, P., O'Brien, W. J., Seepersad, C., Juenger, M., Ferron, R., & Salamone, S. (2018). Applications of additive manufacturing in the construction industry – A forward-looking review. *Automation in Construction*, *89*, 110–119. https://doi.org/10.1016/j.autcon.2017.12.031

36. Bhardwaj, A., Jones, S. Z., Kalantar, N., Pei, Z., Vickers, J., Wangler, T., Zavattieri, P., Zou, N. (2019). Additive Manufacturing Processes for Infrastructure Construction: A Review. *Journal of Manufacturing Science and Engineering*, *141*, 13. https://doi.org/10.1115/1.4044106

37. Bentz, D. P., Jones, S. Z., Bentz, I. R., & Peltz, M. A. (2018). Towards the formulation of robust and sustainable cementitious binders for 3-D additive construction by extrusion.

Construction and Building Materials, *175*, 215–224. https://doi.org/10.1016/j.conbuildmat.2018.04.167

38. Panda, B., Paul, S. C., Mohamed, N. A. N., Tay, Y. W. D., & Tan, M. J. (2018). Measurement of tensile bond strength of 3D printed geopolymer mortar. *Measurement*, *113*, 108–116. https://doi.org/10.1016/j.measurement.2017.08.051
39. Zareiyan, B., & Khoshnevis, B. (2017). Interlayer adhesion and strength of structures in Contour Crafting - Effects of aggregate size, extrusion rate, and layer thickness. *Automation in Construction*, *81*, 112–121. https://doi.org/10.1016/j.autcon.2017.06.013
40. Nerella, V. N., Hempel, S., & Mechtcherine, V. (2017). Micro- and macroscopic investigations on the interface between layers of 3D-printed cementitious elements. In *International Conference on Advances in Construction Materials and Systems* (Vol. 3, pp. 3–8).
41. Lim, S., Buswell, R. A., Valentine, P. J., Piker, D., Austin, S. A., & De Kestelier, X. (2016). Modelling curved-layered printing paths for fabricating large-scale construction components. *Additive Manufacturing*, *12*, 216–230. https://doi.org/10.1016/j.addma.2016.06.004
42. Hegger, J., Curbach, M., Stark, A., Wilhelm, S., & Farwig, K. (2018). Innovative design concepts: Application of textile reinforced concrete to shell structures. *Structural Concrete*, *19*(3), 637–646. https://doi.org/10.1002/suco.201700157
43. Asprone, D., Menna, C., Bos, F. P., Salet, T. A. M., Mata-Falcón, J., & Kaufmann, W. (2018). Rethinking reinforcement for digital fabrication with concrete. *Cement and Concrete Research*, *112*, 111–121. https://doi.org/10.1016/j.cemconres.2018.05.020
44. Mechtcherine, V., Grafe, J., Nerella, V. N., Spaniol, E., Hertel, M., & Füssel, U. (2018). 3D-printed steel reinforcement for digital concrete construction – Manufacture, mechanical

properties and bond behaviour. *Construction and Building Materials*, *179*, 125–137. https://doi.org/10.1016/j.conbuildmat.2018.05.202

45. Hambach, M., & Volkmer, D. (2017). Properties of 3D-printed fiber-reinforced Portland cement paste. *Cement and Concrete Composites*, *79*, 62–70. https://doi.org/10.1016/j.cemconcomp.2017.02.001
46. Soltan, D. G., & Li, V. C. (2018). A self-reinforced cementitious composite for building-scale 3D printing. *Cement and Concrete Composites*, *90*, 1–13. https://doi.org/10.1016/j.cemconcomp.2018.03.017
47. Ogura, H., Nerella, V., & Mechtcherine, V. (2018). Developing and Testing of Strain-Hardening Cement-Based Composites (SHCC) in the Context of 3D-Printing. *Materials*, *11*(8), 1375. https://doi.org/10.3390/ma11081375
48. Hambach, M., Möller, H., Neumann, T., & Volkmer, D. (2016). Portland cement paste with aligned carbon fibers exhibiting exceptionally high flexural strength (> 100 MPa). *Cement and Concrete Research*, *89*, 80–86. https://doi.org/10.1016/j.cemconres.2016.08.011
49. Panda, B., Chandra Paul, S., & Jen Tan, M. (2017). Anisotropic mechanical performance of 3D printed fiber reinforced sustainable construction material. *Materials Letters*, *209*, 146–149. https://doi.org/10.1016/j.matlet.2017.07.123
50. Al-Qutaifi, S., Nazari, A., & Bagheri, A. (2018). Mechanical properties of layered geopolymer structures applicable in concrete 3D-printing. *Construction and Building Materials*, *176*, 690–699. https://doi.org/10.1016/j.conbuildmat.2018.04.195
51. Bos, F. P., Bosco, E., & Salet, T. A. M. (2019). Ductility of 3D printed concrete reinforced with short straight steel fibers. *Virtual and Physical Prototyping*, *14*(2), 160–174. https://doi.org/10.1080/17452759.2018.1548069

52. Farina, I., Fabbrocino, F., Carpentieri, G., Modano, M., Amendola, A., Goodall, R., Feo, L., Fraternali, F. (2016). On the reinforcement of cement mortars through 3D printed polymeric and metallic fibers. *Composites Part B: Engineering*, *90*, 76–85. https://doi.org/10.1016/j.compositesb.2015.12.006

53. Han, B., Zhang, L., Zhang, C., Wang, Y., Yu, X., & Ou, J. (2016). Reinforcement effect and mechanism of carbon fibers to mechanical and electrically conductive properties of cement-based materials. *Construction and Building Materials*, *125*, 479–489. http://dx.doi.org/10.1016/j.conbuildmat.2016.08.063

54. Šahmenko, G., & Krasnikovs, A. (2015). Ultra High Performance Concrete Reinforced with Short Steel and Carbon Fibers. In *Proceedings of the 10th International Scientific and Practical Conference* (Vol. 1, pp. 193–199). https://doi.org/10.17770/etr2015vol1.196

55. Shakor, P., Nejadi, S., & Paul, G. (2019). A Study into the Effect of Different Nozzles Shapes and Fibre-Reinforcement in 3D Printed Mortar. *Materials*, *12*(10), 1708. https://doi.org/10.3390/ma12101708

56. Bentz, D. P., & Weiss, W. J. (2011). *Internal curing: a 2010 state-of-the-art review* (No. NIST IR 7765). Gaithersburg, MD: National Institute of Standards and Technology. https://doi.org/10.6028/NIST.IR.7765

57. Marchon, D., Kawashima, S., Bessaies-Bey, H., Mantellato, S., & Ng, S. (2018). Hydration and rheology control of concrete for digital fabrication: Potential admixtures and cement chemistry. *Cement and Concrete Research*, *112*, 96–110. https://doi.org/10.1016/j.cemconres.2018.05.014

58. Wolfs, R. J. M., Bos, F. P., & Salet, T. A. M. (2019). Hardened properties of 3D printed concrete: The influence of process parameters on interlayer adhesion. *Cement and Concrete Research*, *119*, 132–140. https://doi.org/10.1016/j.cemconres.2019.02.017

59. Park, S.-I., Rosen, D. W., Choi, S., & Duty, C. E. (2014). Effective mechanical properties of lattice material fabricated by material extrusion additive manufacturing. *Additive Manufacturing*, *1–4*, 12–23. https://doi.org/10.1016/j.addma.2014.07.002

60. Okamura, H., & Ouchi, M. (2003). Self-Compacting Concrete. *Journal of Advanced Concrete Technology*, *1*(1), 5–15. https://doi.org/10.3151/jact.1.5

61. Secrieru, E., Fataei, S., Schrofl, C., & Mechtcherine, V. (2017). Study on concrete pumpability combining different laboratory tools and linkage to rheology. *Construction and Building Materials*, *144*, 451–461. https://doi.org/10.1016/j.conbuildmat.2017.03.199

62. Papachristoforou, M., Mitsopoulos, V., & Stefanidou, M. (2018). Evaluation of workability parameters in 3D printing concrete. *Procedia Structural Integrity*, *10*, 155–162. https://doi.org/10.1016/j.prostr.2018.09.023

63. Panda, B., Ruan, S., Unluer, C., & Jen Tan, M. (2019). Improving the 3D printability of high volume fly ash mixtures via the use of nano attapulgite clay. *Composites Part B*, *165*, 75–83. https://doi.org/10.1016/j.compositesb.2018.11.109

64. Panda, B., Unluer, C., & Jen Tan, M. (2018). Investigation of the rheology and strength of geopolymer mixtures for extrusion-based 3D printing. *Cement and Concrete Composites*, *94*, 307–314. https://doi.org/10.1016/j.cemconcomp.2018.10.002

65. Alghamdi, H., Nair, S. A. O., & Neithalath, N. (2019). Insights into material design, extrusion rheology, and properties of 3D-printable alkali-activated fly ash-based binders. *Materials and Design*, *167*, 13. https://doi.org/10.1016/j.matdes.2019.107634

66. Nair, S. A. O., Alghamdi, H., Arora, A., Mehdipour, I., Sant, G., & Neithalath, N. (2019). Linking fresh paste microstructure, rheology and extrusion characteristics of cementitious binders for 3D printing. *Journal of the American Ceramic Society*, *102*(7), 3951–3964. https://doi.org/10.1111/jace.16305

67. Ji, G., Ding, T., Xiao, J., Du, S., Li, J., & Duan, Z. (2019). A 3D Printed Ready-Mixed Concrete Power Distribution Substation: Materials and Construction Technology. *Materials*, *12*(9), 1540. https://doi.org/10.3390/ma12091540

68. Lootens, D., Jousset, P., Martinie, L., Roussel, N., & Flatt, R. J. (2009). Yield stress during setting of cement pastes from penetration tests. *Cement and Concrete Research*, *39*(5), 401–408. https://doi.org/10.1016/j.cemconres.2009.01.012

69. Tregger, N., Ferrara, L., & Shah, S. P. (2008). Identifying Viscosity of Cement Paste from Mini-Slump-Flow Test. *ACI Materials Journal*, *105*(6). https://doi.org/10.14359/20197

68. ASTM C78 / C78M-18, *Test Method for Flexural Strength of Concrete (Using Simple Beam with Third-Point Loading)*. ASTM International. https://doi.org/10.1520/C0078_C0078M-18

69. ASTM C293 / C293M-16. *Test Method for Flexural Strength of Concrete (Using Simple Beam With Center-Point Loading)*. ASTM International. https://doi.org/10.1520/C0293_C0293M-16

70. ASTM C39 / C39M-18. *Test Method for Compressive Strength of Cylindrical Concrete Specimens*. ASTM International. https://doi.org/10.1520/C0039_C0039M-18

71. ASTM C873 / 873M-15. *Test Method for Compressive Strength of Concrete Cylinders Cast in Place in Cylindrical Molds*. ASTM International. https://doi.org/10.1520/C0873_C0873M-15

72. ASTM C348-18. *Test Method for Flexural Strength of Hydraulic-Cement Mortars*. ASTM International. https://doi.org/10.1520/C0348-18

73. ASTM C109 / C109M-16a. *Test Method for Compressive Strength of Hydraulic Cement Mortars (Using 2-in. or [50-mm] Cube Specimens)*. ASTM International. https://doi.org/10.1520/C0109_C0109M-16A

76. Forster, A. M. (2015). *Materials Testing Standards for Additive Manufacturing of Polymer Materials: State of the Art and Standards Applicability* (No. NIST IR 8059) (p. NIST IR 8059). National Institute of Standards and Technology. https://doi.org/10.6028/NIST.IR.8059

77. Sanjayan, J. G., Nematollahi, B., Xia, M., & Marchment, T. (2018). Effect of surface moisture on inter-layer strength of 3D printed concrete. *Construction and Building Materials*, *172*, 468–475. https://doi.org/10.1016/j.conbuildmat.2018.03.232

78. Zareiyan, B., & Khoshnevis, B. (2017). Effects of interlocking on interlayer adhesion and strength of structures in 3D printing of concrete. *Automation in Construction*, *83*, 212–221. http://dx.doi.org/10.1016/j.autcon.2017.08.019

79. Jie, G., Jie, B., & Hongxue, J. (2019). Experimental study on layer bonding property of 3D printing building materials. In *IOP Conference Series: Earth and Environmental Science* (Vol. 267, p. 7). https://doi.org/10.1088/1755-1315/267/2/022005

80. Paul, S. C., Tay, Y. W. D., Panda, B., & Tan, M. J. (2018). Fresh and hardened properties of 3D printable cementitious materials for building and construction. *archives of civil and mechanical engineering*, *18*, 311–319. http://dx.doi.org/10.1016/j.acme.2017.02.008

81. Pan, B. (2018). Digital image correlation for surface deformation measurement: historical developments, recent advances and future goals. *Measurement Science and Technology*, *29*(8), 082001. https://doi.org/10.1088/1361-6501/aac55b

82. Hamrat, M., Boulekbache, B., Chemrouk, M., & Amziane, S. (2016). Flexural cracking behavior of normal strength, high strength and high strength fiber concrete beams, using Digital Image Correlation technique. *Construction and Building Materials*, *106*, 678–692. https://doi.org/10.1016/j.conbuildmat.2015.12.166

83. Pan, B., Wang, Z., & Lu, Z. (2010). Genuine full-field deformation measurement of an object with complex shape using reliability-guided digital image correlation. *Optics Express*, *18*(2), 1011–1023. https://doi.org/10.1364/OE.18.001011

84. Krawczyk, Ł., Gołdyn, M., & Urban, T. (2019). Digital Image Correlation Systems in the Experimental Investigations: Capabilities and Limitations. *Archives of Civil Engineering*, *65*(1), 171–180. https://doi.org/10.2478/ace-2019-0012

85. Chesser, P. C., Post, B. K., Roschli, A., Lind, R. F., Boulger, A. M., & Gaul, K. T. (2018). Fieldable platform for large-scale deposition of concrete structures. In *Solid Freeform Fabrication 2018* (pp. 2020–2032). Presented at the International Solid Freeform Fabrication Symposium – An Additive Manufacturing Conference.

83. ASTM C136 / C136M-14. *Test Method for Sieve Analysis of Fine and Coarse Aggregates*. ASTM International. https://doi.org/10.1520/C0136_C0136M-14

84. ASTM C128-15. *Test Method for Relative Density (Specific Gravity) and Absorption of Fine Aggregate*. ASTM International. https://doi.org/10.1520/C0128-15

85. ASTM C566-19. *Test Method for Total Evaporable Moisture Content of Aggregate by Drying*. ASTM International. https://doi.org/10.1520/C0566-19

89. Brand, A. S., Roesler, J. R., & Salas, A. (2015). Initial moisture and mixing effects on higher quality recycled coarse aggregate concrete. *Construction and Building Materials*, *79*, 83–89. https://doi.org/10.1016/j.conbuildmat.2015.01.047

90. Mefteh, H., Kebaïli, O., Oucief, H., Berredjem, L., & Arabi, N. (2013). Influence of moisture conditioning of recycled aggregates on the properties of fresh and hardened concrete. *Journal of Cleaner Production*, *54*, 282–288. https://doi.org/10.1016/j.jclepro.2013.05.009

91. Brand, A. S., & Roesler, J. (2018). Interfacial Transition Zone of Cement Composites with Recycled Concrete Aggregate of Different Moisture States. *Advances in Civil Engineering Materials*, *7*(1), 20170090. https://doi.org/10.1520/ACEM20170090

89. ASTM C305-14. *Practice for Mechanical Mixing of Hydraulic Cement Pastes and Mortars of Plastic Consistency*. ASTM International. https://doi.org/10.1520/C0305-14

90. ASTM C1437-15. *Standard Test Method for Flow of Hydraulic Cement Mortar*. ASTM International. https://doi.org/10.1520/C1437-15

91. ASTM C807-18. *Test Method for Time of Setting of Hydraulic Cement Mortar by Modified Vicat Needle*. ASTM International. https://doi.org/10.1520/C0807-18

95. Sri Ravindrarajah, R., Loo, Y. H., & Tam, C. T. (1987). Recycled concrete as fine and coarse aggregates in concrete. *Magazine of Concrete Research*, *39*(141), 214–220. https://doi.org/10.1680/macr.1987.39.141.214

96. de Oliveira, M. B., & Vazquez, E. (1996). The influence of retained moisture in aggregates from recycling on the properties of new hardened concrete. *Waste Management*, *16*(1–3), 113–117. https://doi.org/10.1016/S0956-053X(96)00033-5

97. Wight, J. K. (2015). *Reinforced Concrete Mechanics and Design* (7th ed.). Pearson.

Appendix A

Specimen B1S1-V2 observations:

- Orientation A
- Defect between layers 1 and 2
- A diagonal break through one layer (Figure A-2)

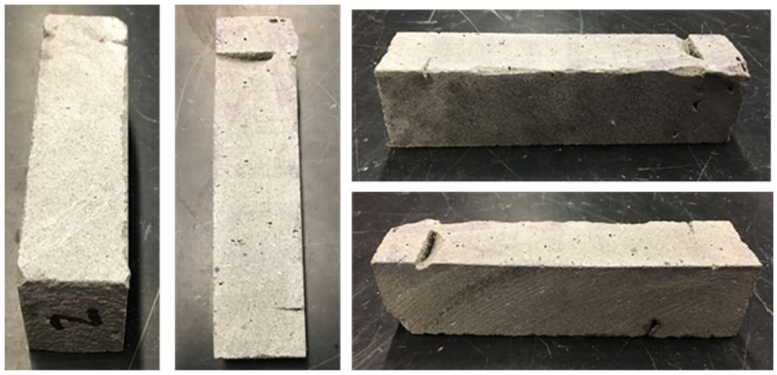

Figure A-1: B1S1-V2 prior to testing

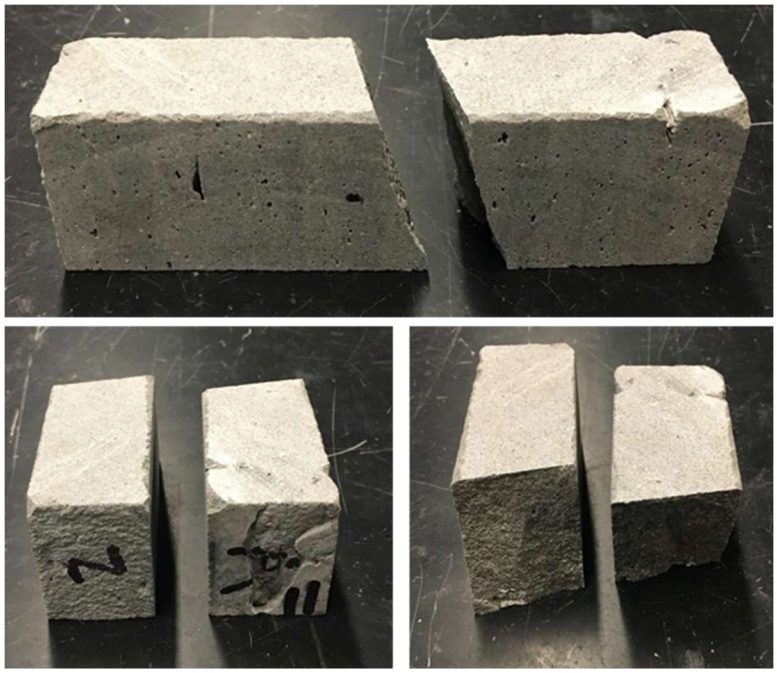

Figure A-2: B1S1-V2 after failure

Specimen B1S1-V6 observations:

- Orientation A
- Defect between layers 1 and 2
- The specimen had another defect as seen in photos (Figure A-5), which may have been unhydrated slag and likely affected the modulus of rupture.
- Lowest flexural strength of all 8 tests.

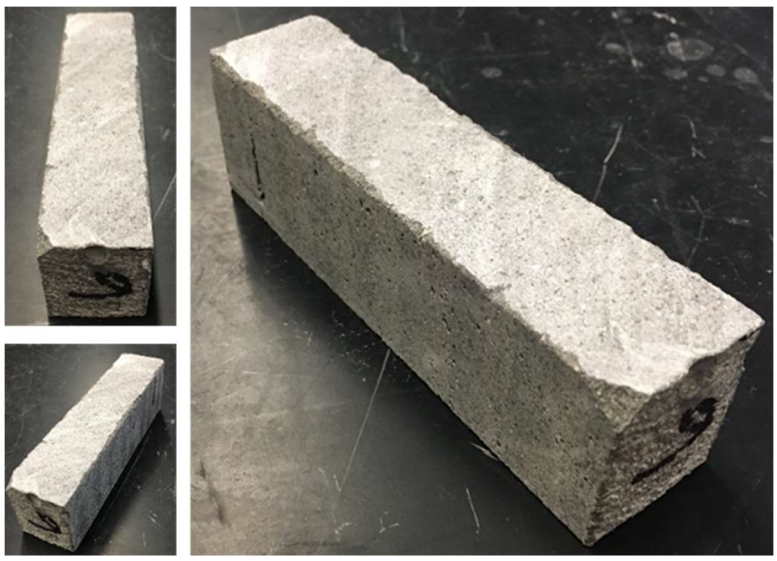

Figure A-3: B1S1-V6 prior to testing

Figure A-4: B1S1-V6 after failure

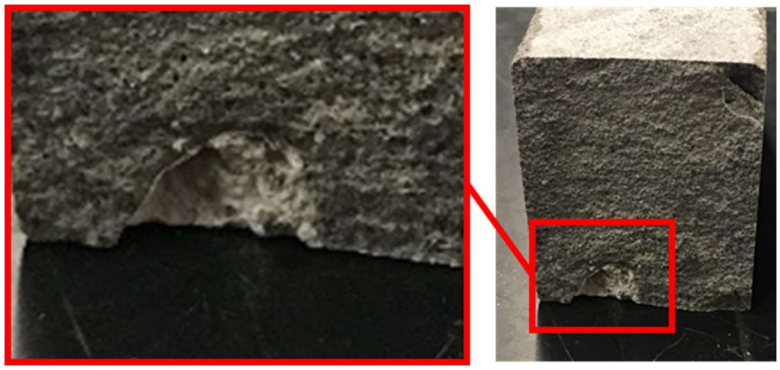

Figure A-5: Detailed view of defect in B1S1-V6

Specimen B1S1-V7 observations:

- Orientation A
- Defect between layers 1 and 2
- Slight diagonal in the break at ending at an interface (Figure A-7)

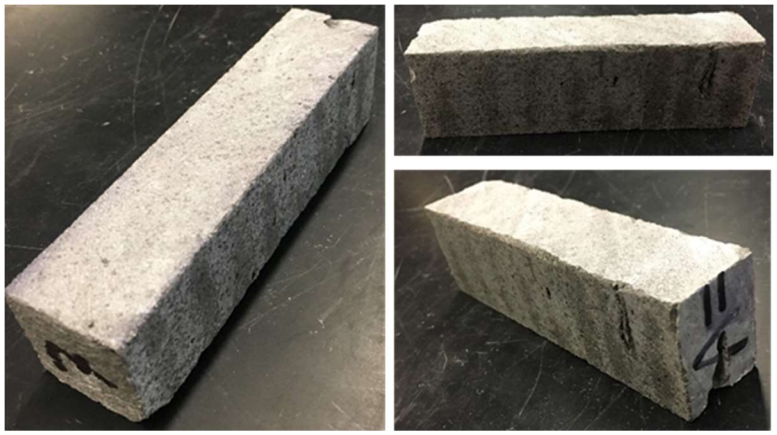

Figure A-6: B1S1-V7 prior to testing

Figure A-7: B1S1-V7 after failure

Specimen B1S1-V8 observations:

- Orientation A
- Defect between layers 1 and 2
- Clean break at interface (Figure A-9)

Figure A-8: B1S1-V8 prior to testing

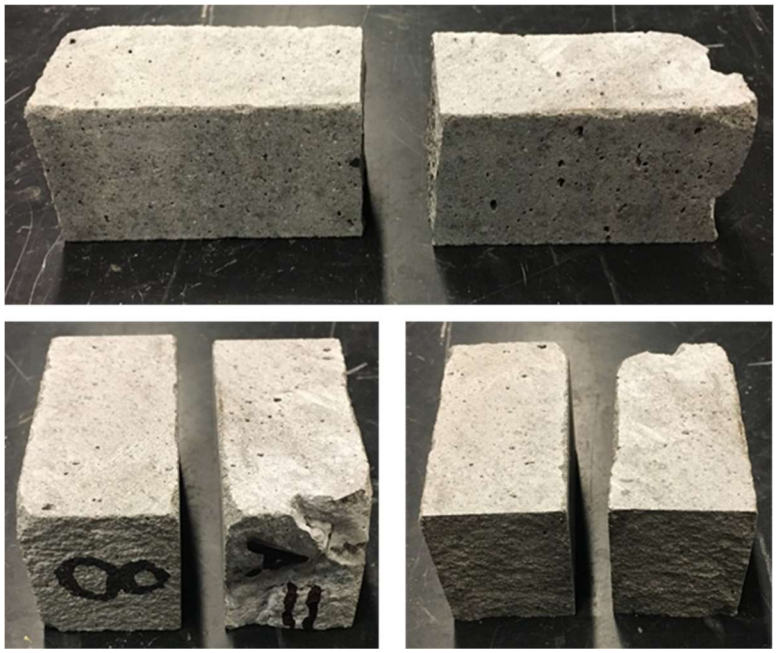

Figure A-9: B1S1-V8 after failure

Specimen B1S1-V1 observations:

- Orientation B
- Defect between layers 1 and 2 (numbered ascending from bottom to top)
- The failure occurred in the middle at the interface (Figure A-11)
- Clean break at interface

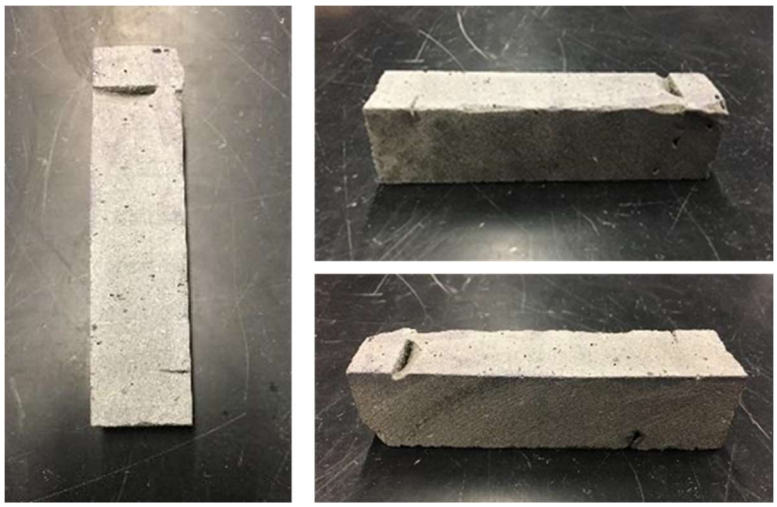

Figure A-10: B1S1-V1 prior to testing

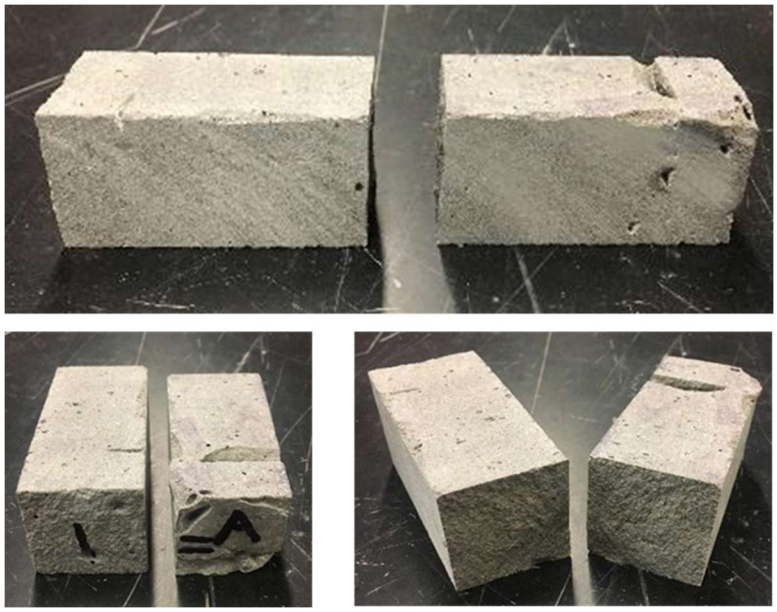

Figure A-11: B1S1-V1 after failure

Specimen B1S1-V3 observations:

- Orientation B
- Defect between layers 1 and 2
- The failure occurred in the middle at the interface (Figure A-13)
- Clean break at interface

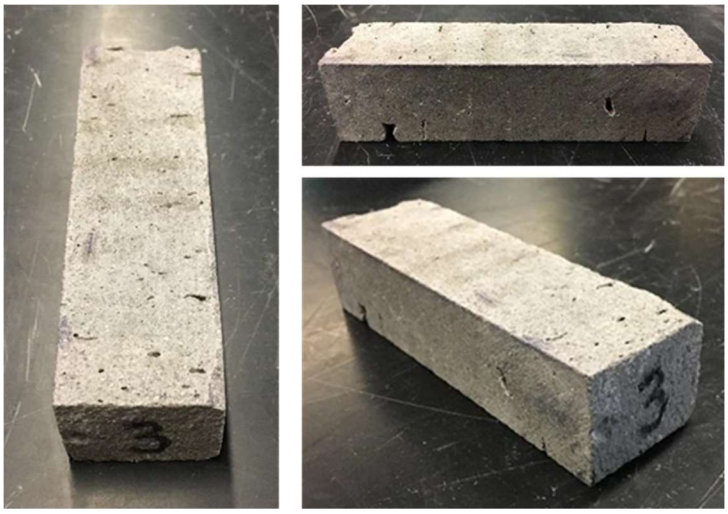

Figure A-12: B1S1-V3 prior to testing

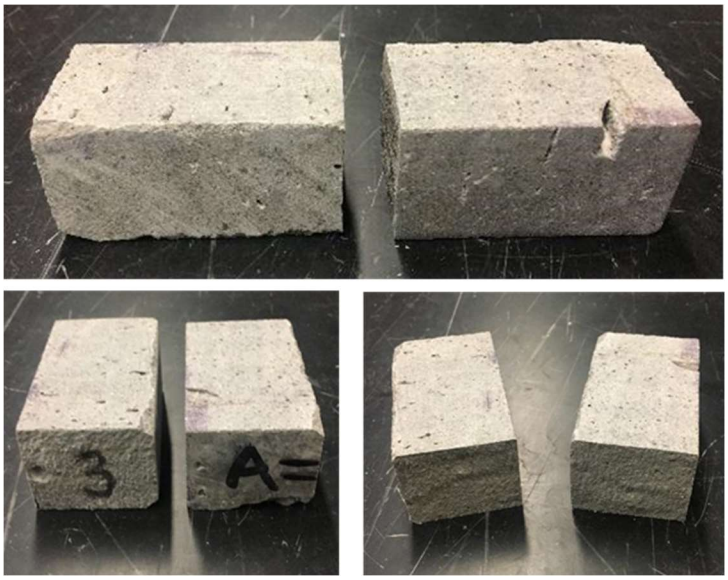

Figure A-13: B1S1-V3 after failure

Specimen B1S1-V4 observations:

- Orientation B
- Defect between layers 1 and 2
- Did not break in the center. Failure occurred at a layer interface, but closer to the bottom of the printed part. (Figure A-15)
- Different failure than all other specimens tested in the perpendicular direction (but not the lowest flexural strength)

Figure A-14: B1S1-V4 prior to testing

Figure A-15: B1S1-V4 after failure

Specimen B1S1-V5 observations:

- Orientation B
- Defect between layers 1 and 2
- The failure occurred in the middle at the interface (Figure A-17)
- Clean break at interface
- Lowest flexural strength of the perpendicular tests

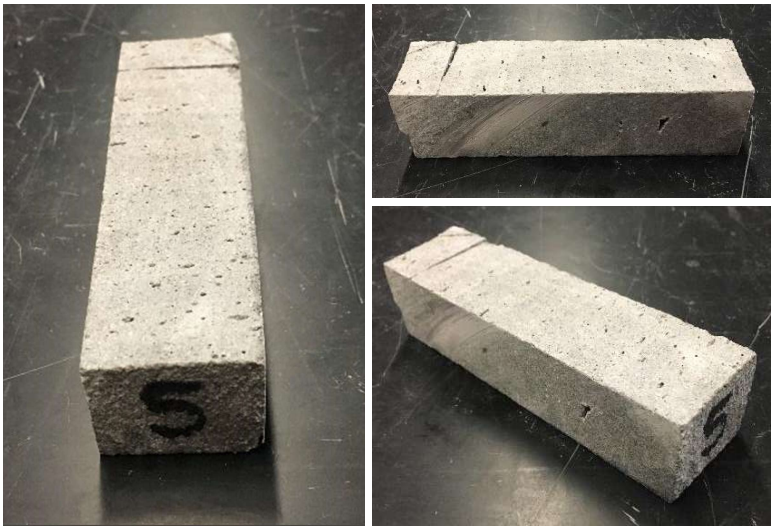

Figure A-16: B1S1-V5 prior to testing

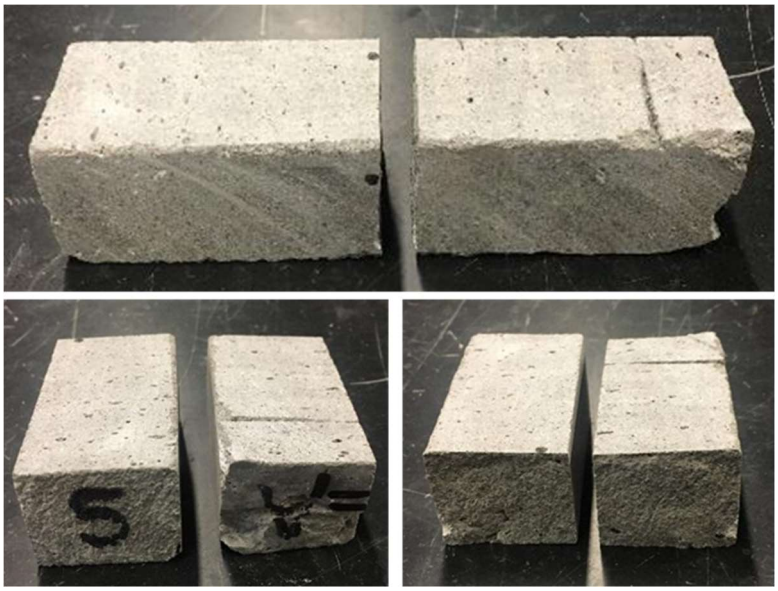

Figure A-17: B1S1-V5 after failure

Appendix B

Table B-1: Mortar 7 mix design

Design w/c ratio	0.375			Required volume	45.21	in^3
Design s/c ratio	1.5			Planned excess	20%	
				Batching volume	54.25	in^3
Total cementitious	689.59	g		Batching volume	888.95	cm^3
Design water	258.60	g				
Design sand (SSD)	1034.39	g				
Batching cement	413.76	g				
Batching fly ash	0.00	g				
Batching GGBFS	206.88	g				
Batching silica fume	68.96	g				
Batching water	269.65	g				
Batching Sand	1023.34	g				
Glenium	3.71	mL				
Cement SG	3.15					
Sand SG (SSD)	2.61					
Fly ash SG	2.3					
GGBFS SG	2.9					
Silica fume SG	2.2					
Cementitious Design (by weight)						
Cement	60%					
Fly Ash	0%					
GGBFS	30%					
Silica fume	10%					
	100%					
Sand Corrections						
Sand absorption	1.08%					
Sand moisture content	0.00%					

Table B-2: Mortar 8 mix design

Design w/c ratio	0.375			Required volume	45.21	in^3
Design s/c ratio	1.5			Planned excess	20%	
				Batching volume	54.25	in^3
Total cementitious	713.27	g		Batching volume	888.95	cm^3
Design water	267.48	g				
Design sand (SSD)	1069.91	g				
Batching cement	427.96	g				
Batching fly ash	0.00	g				
Batching GGBFS	213.98	g				
Batching silica fume	71.33	g				
Batching water	272.48	g				
Batching Sand	1064.90	g				
Glenium	3.83	mL				
Cement SG	3.15					
Sand SG (SSD)	2.82					
Fly ash SG	2.3					
GGBFS SG	2.9					
Silica fume SG	2.2					
Cementitious Design (by weight)						
Cement	60%					
Fly Ash	0%					
GGBFS	30%					
Silica fume	10%					
	100%					
Sand Corrections						
Sand absorption	0.47%					
Sand moisture content	0.00%					

Table B-3: Mortar 9 mix design

Design w/c ratio	0.375			Required volume	45.20575	in^3
Design s/c ratio	1.5			Planned excess	20%	
				Batching volume	54.25	in^3
Total cementitious	689.59	g		Batching volume	888.95	cm^3
Design water	258.60	g				
Design sand (SSD)	1034.39	g				
Batching cement	413.76	g				
Batching fly ash	0.00	g				
Batching GGBFS	206.88	g				
Batching silica fume	68.96	g				
Batching water	268.11	g				
Batching Sand	1024.87	g				
Glenium	3.71	mL				
Cement SG	3.15					
Sand SG (SSD)	2.61					
Fly ash SG	2.3					
GGBFS SG	2.9					
Silica fume SG	2.2					
Cementitious Design (by weight)						
Cement	60%					
Fly Ash	0%					
GGBFS	30%					
Silica fume	10%					
	100%					
Sand Corrections						
Sand absorption	1.08%					
Sand moisture content	0.15%					

Table B-4: Mortar 10 mix design

Design w/c ratio	0.375			Required volume	45.21	in^3
Design s/c ratio	1.5			Planned excess	20%	
				Batching volume	54.25	in^3
Total cementitious	713.27	g		Batching volume	888.95	cm^3
Design water	267.48	g				
Design sand (SSD)	1069.91	g				
Batching cement	427.96	g				
Batching fly ash	0.00	g				
Batching GGBFS	213.98	g				
Batching silica fume	71.33	g				
Batching water	272.16	g				
Batching Sand	1065.22	g				
Glenium	3.83	mL				
Cement SG	3.15					
Sand SG (SSD)	2.82					
Fly ash SG	2.3					
GGBFS SG	2.9					
Silica fume SG	2.2					
Cementitious Design (by weight)						
Cement	60%					
Fly Ash	0%					
GGBFS	30%					
Silica fume	10%					
	100%					
Sand Corrections						
Sand absorption	0.47%					
Sand moisture content	0.03%					

Table B-5: Mortar 11 mix design

Design w/c ratio	0.375			Required volume	45.21	in^3
Design s/c ratio	1.5			Planned excess	20%	
				Batching volume	54.25	in^3
Total cementitious	689.59	g		Batching volume	888.95	cm^3
Design water	258.60	g				
Design sand (SSD)	1034.39	g				
Batching cement	413.76	g				
Batching fly ash	0.00	g				
Batching GGBFS	206.88	g				
Batching silica fume	68.96	g				
Batching water	258.60	g				
Batching Sand	1034.39	g				
Glenium	3.71	mL				
Cement SG	3.15					
Sand SG (SSD)	2.61					
Fly ash SG	2.3					
GGBFS SG	2.9					
Silica fume SG	2.2					
Cementitious Design (by weight)						
Cement	60%					
Fly Ash	0%					
GGBFS	30%					
Silica fume	10%					
	100%					
Sand Corrections						
Sand absorption	1.08%					
Sand moisture content	1.08%					

Table B-6: Mortar 12 mix design

Design w/c ratio	0.375			Required volume	45.21	in^3
Design s/c ratio	1.5			Planned excess	20%	
				Batching volume	54.25	in^3
Total cementitious	713.27	g		Batching volume	888.95	cm^3
Design water	267.48	g				
Design sand (SSD)	1069.91	g				
Batching cement	427.96	g				
Batching fly ash	0.00	g				
Batching GGBFS	213.98	g				
Batching silica fume	71.33	g				
Batching water	267.48	g				
Batching Sand	1069.91	g				
Glenium	3.83	mL				
Cement SG	3.15					
Sand SG (SSD)	2.82					
Fly ash SG	2.3					
GGBFS SG	2.9					
Silica fume SG	2.2					
Cementitious Design (by weight)						
Cement	60%					
Fly Ash	0%					
GGBFS	30%					
Silica fume	10%					
	100%					
Sand Corrections						
Sand absorption	0.47%					
Sand moisture content	0.47%					

Appendix C

Specimen B2S1-V1 observations

- Orientation A
- Visual defects between layers (Figure C-1)
- Unit weight = 131.4 pcf (γ < 132 pcf)
- Failed at defect; not at midspan

Figure C-1: B2S1-V1 prior to testing

Specimen B2S1-V2 observations

- Orientation A
- Visual defects between layers (Figure C-2)
- Unit weight = 131.2 pcf (γ < 132 pcf)
- Failed at defect; not at midspan

Figure C-2: B2S1-V2 prior to testing

Specimen B2S2-V1 observations

- Orientation A
- Minor visual defects between layers, but they are small, very few, and not near midspan (Figure C-3)
- Unit weight = 131.6 pcf (γ < 132 pcf)
- Failed at midspan at interface

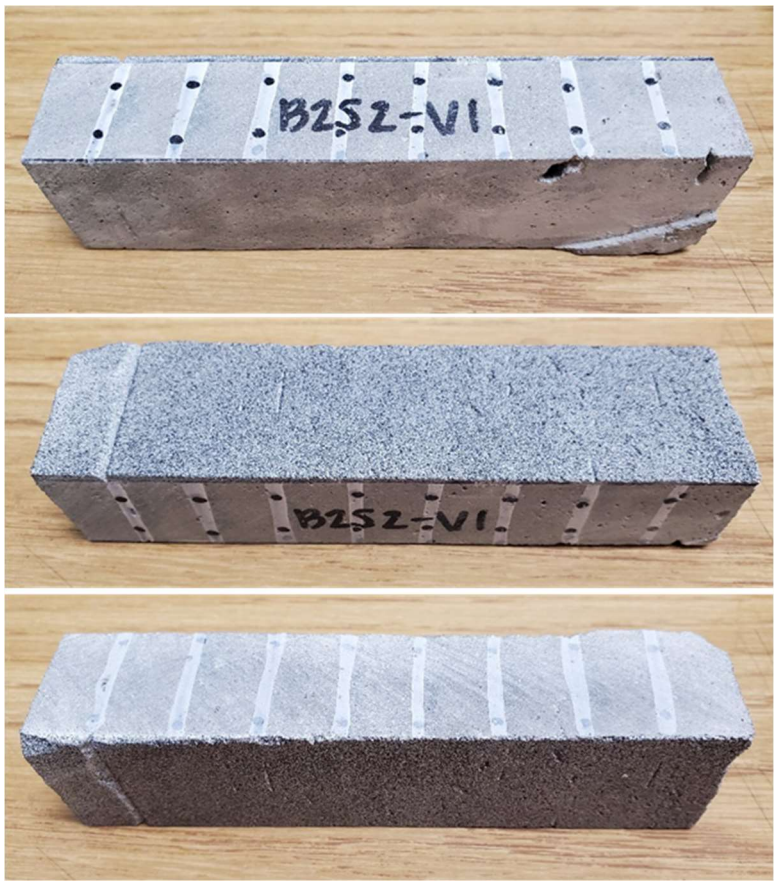

Figure C-3: B2S2-V1 prior to testing

Specimen B2S2-V2 observations

- Orientation A
- No obvious visual defects before testing. The lines on the speckled face are from residual excess bead width from the rounded edges (Figure C-4)
- Unit weight = 134.6 pcf (γ > 132 pcf)
- Failed at midspan at interface

Figure C-4: B2S2-V2 prior to testing

Specimen B2S2-V3 observations

- Orientation A
- No obvious visual defects before testing (Figure C-5)
- Unit weight = 135.4 pcf (γ > 132 pcf)
- Failed at midspan at interface

Figure C-5: B2S2-V3 prior to testing

Specimen B2S3-V1 observations

- Orientation A
- No obvious visual defects before testing (Figure C-6)
- Unit weight = 133.7 pcf (γ > 132 pcf)
- Failure originated at another interface; diagonal failure surface

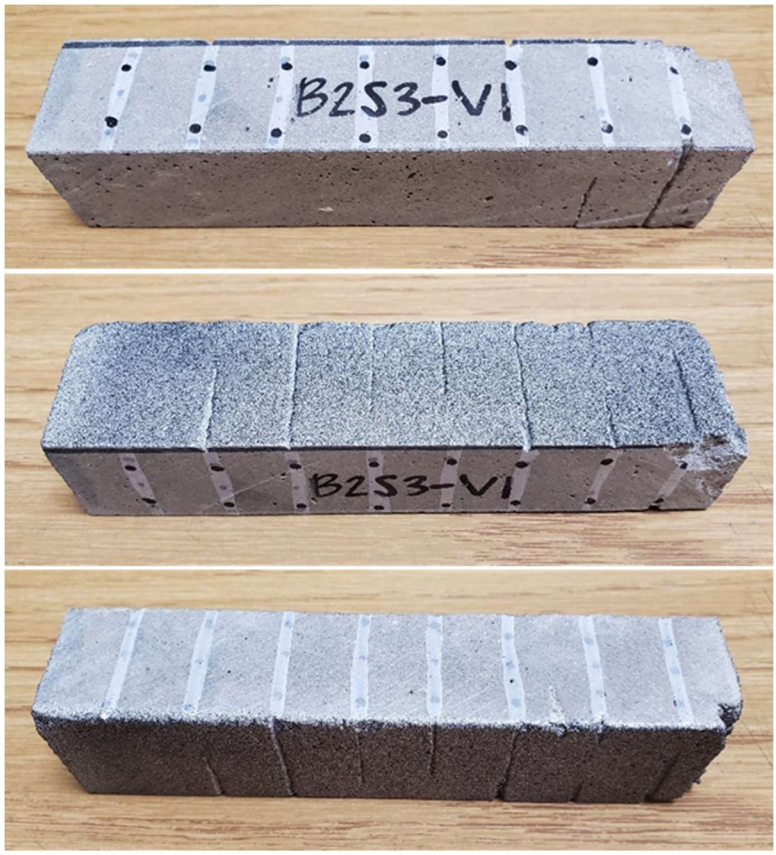

Figure C-6: B2S3-V1 prior to testing

Specimen B2S3-V2 observations

- Orientation A
- Minor visual defects before testing at right end on speckled face (Figure C-7)
- Unit weight = 133.4 pcf (γ > 132 pcf)
- Failed at midspan at interface

Figure C-7: B2S3-V2 prior to testing

Specimen B2S1-V3 observations

- Orientation B
- Visual defects between layers (Figure C-8)
- Unit weight = 129.2 pcf (γ < 132 pcf)
- Failed at defect; started at midspan

Figure C-8: B2S1-V3 prior to testing

Specimen B2S1-V4 observations

- Orientation B
- Minor visual defects between layers (Figure C-9)
- Unit weight = 131.1 pcf (γ < 132 pcf)
- Failed at defect; not at midspan

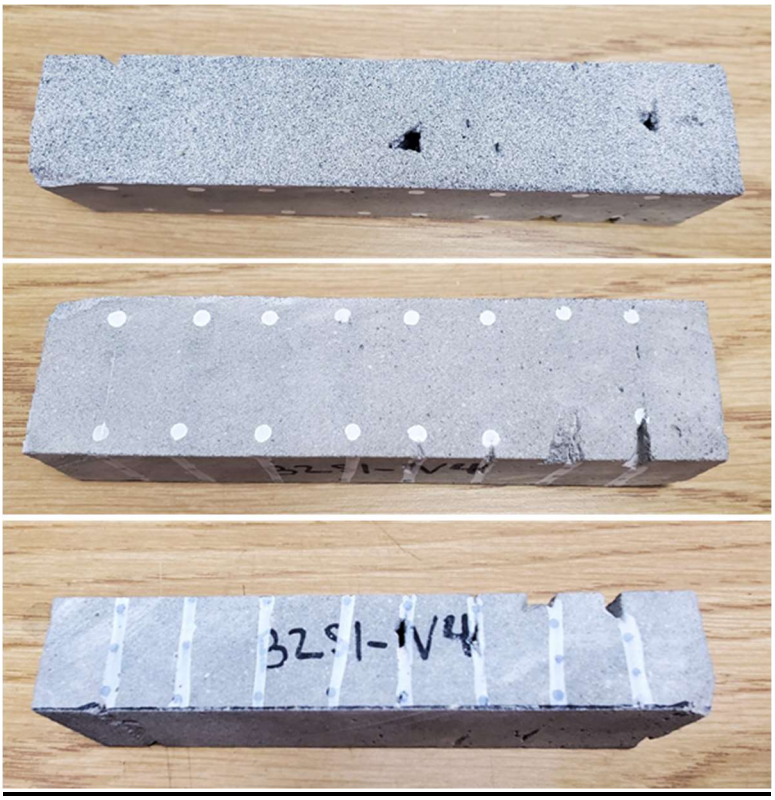

Figure C-9: B2S1-V4 prior to testing

Specimen B2S1-V5 observations

- Orientation B
- Visual defects between layers; large defect near midspan (Figure C-10)
- Unit weight = 127.8 pcf (γ < 132 pcf)
- Failed at large defect; not at midspan

Figure C-10: B2S1-V5 prior to testing

Specimen B2S2-V4 observations

- Orientation B
- Visual defects between layers on one side; seem superficial (Figure C-11)
- Unit weight = 133.5 pcf (γ > 132 pcf)
- Failure originated at midspan interface but was diagonal

Figure C-11: B2S2-V4 prior to testing

Specimen B2S2-V5 observations

- Orientation B
- Visual defects between layers on one side (Figure C-12)
- Unit weight = 130.4 pcf (γ < 132 pcf)
- Failed at defect; not midspan

Figure C-12: B2S2-V5 prior to testing

Specimen B2S3-V3 observations

- Orientation B
- No obvious visual defects before testing (Figure C-13)
- Unit weight = 134.1 pcf (γ > 132 pcf)
- Failed at midspan

Figure C-13: B2S3-V3 prior to testing

Specimen B2S3-V4 observations

- Orientation B
- No obvious visual defects before testing (Figure C-14)
- Unit weight = 134.8 pcf (γ > 132 pcf)
- Failed at midspan at interface

Figure C-14: B2S3-V4 prior to testing

Specimen B2S1 - H4 observations

- Orientation C
- No obvious visual defects before testing (Figure C-15)
- Unit weight = 134.5 pcf (γ > 132 pcf)
- Failed at midspan

Figure C-15: B2S1-H4 prior to testing

Specimen B2S1 - H6 observations

- Orientation C
- Visual defects before testing (Figure C-16)
- Unit weight = 126.1 pcf (γ < 132 pcf)
- Failed close to midspan; competing flexural cracks seen in DIC results

Figure C-16: B2S1-H6 prior to testing

Specimen B2S3 - H1 observations

- Orientation C
- No obvious visual defects before testing (Figure C-17)
- Unit weight = 133.6 pcf (γ > 132 pcf)
- Failed at midspan

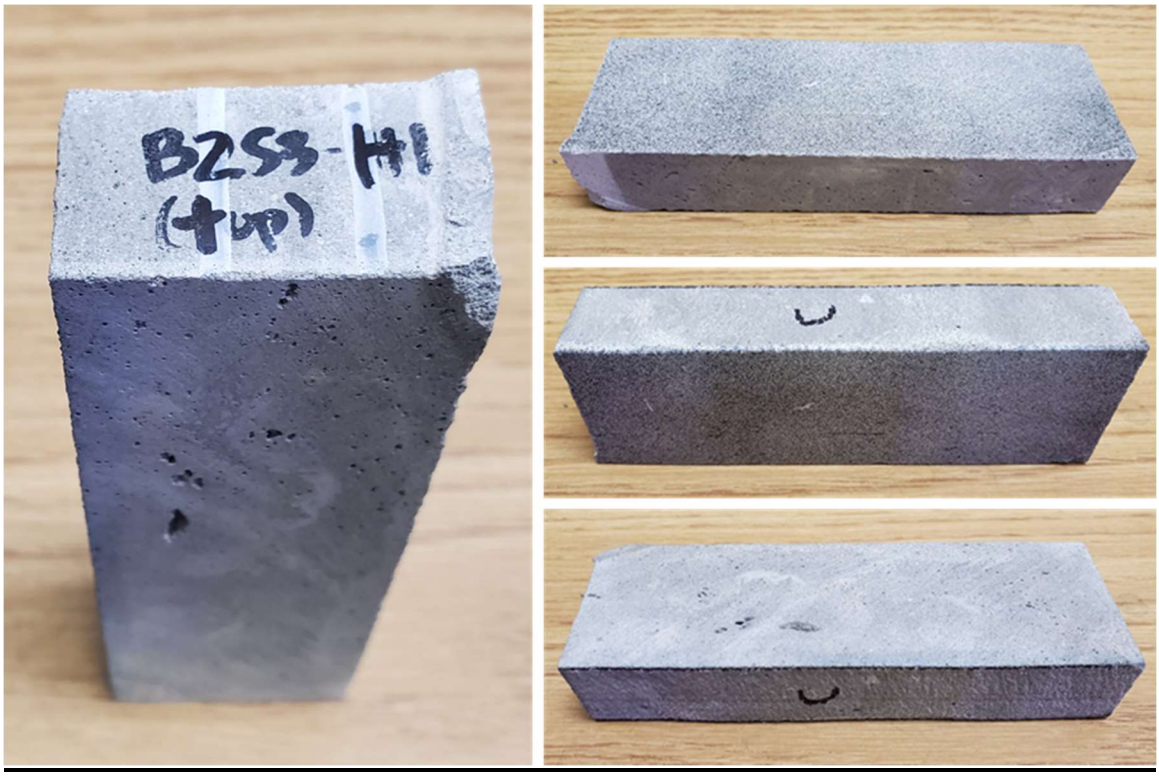

Figure C-17: B2S3-H1 prior to testing

Specimen B2S3 - H2 observations

- Orientation C
- No obvious visual defects before testing (Figure C-18)
- Unit weight = 136.0 pcf (γ > 132 pcf)
- Failed at midspan

Figure C-18: B2S3-H2 prior to testing

Specimen B2S3 - H3 observations

- Orientation C
- Visual defects between layers (Figure C-19)
- Unit weight = 132.4 pcf (γ > 132 pcf)
    - This barely makes the cutoff
- Failed at midspan

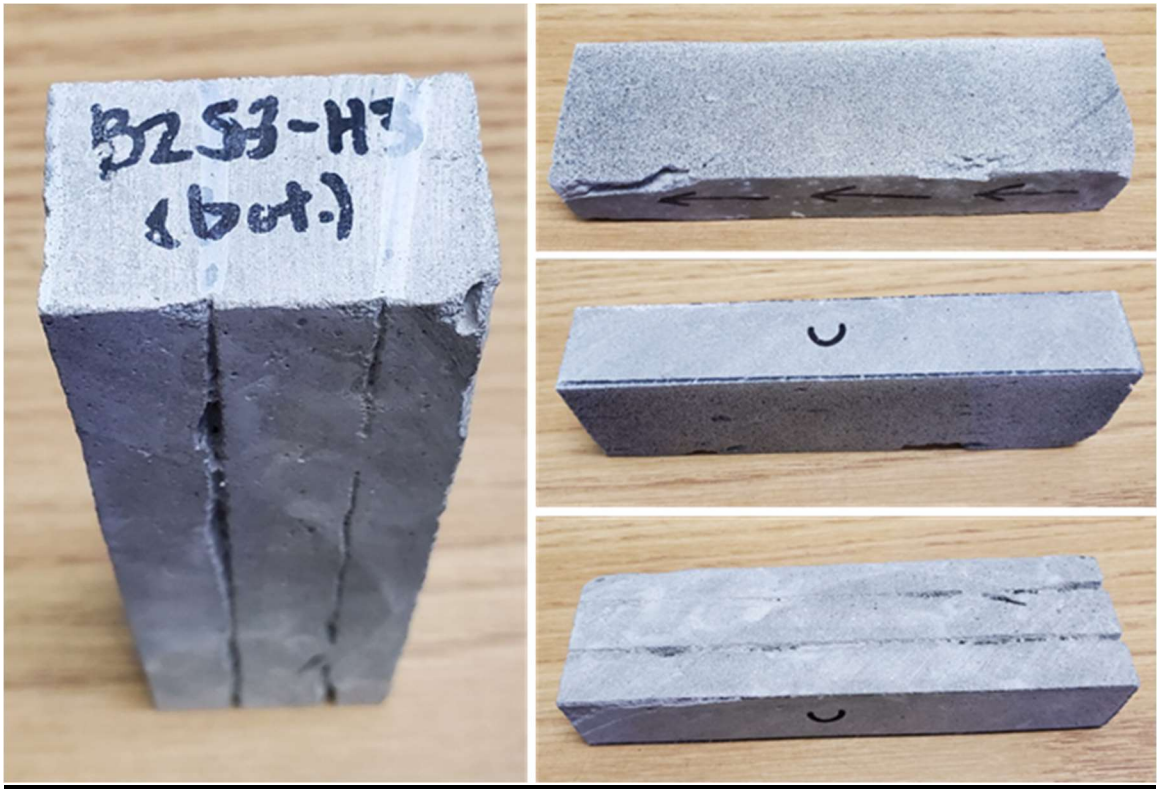

Figure C-19: B2S3-H3 prior to testing

Specimen B2S3 - H4 observations

- Orientation C
- No obvious visual defects before testing (Figure C-20)
- Unit weight = 134.7 pcf (γ > 132 pcf)
- Failed at midspan

Figure C-20: B2S3-H4 prior to testing

Specimen B2S3 - H5 observations

- Orientation C
- No obvious visual defects before testing (Figure C-21)
- Unit weight = 134.3 pcf (γ > 132 pcf)
- Failed at midspan

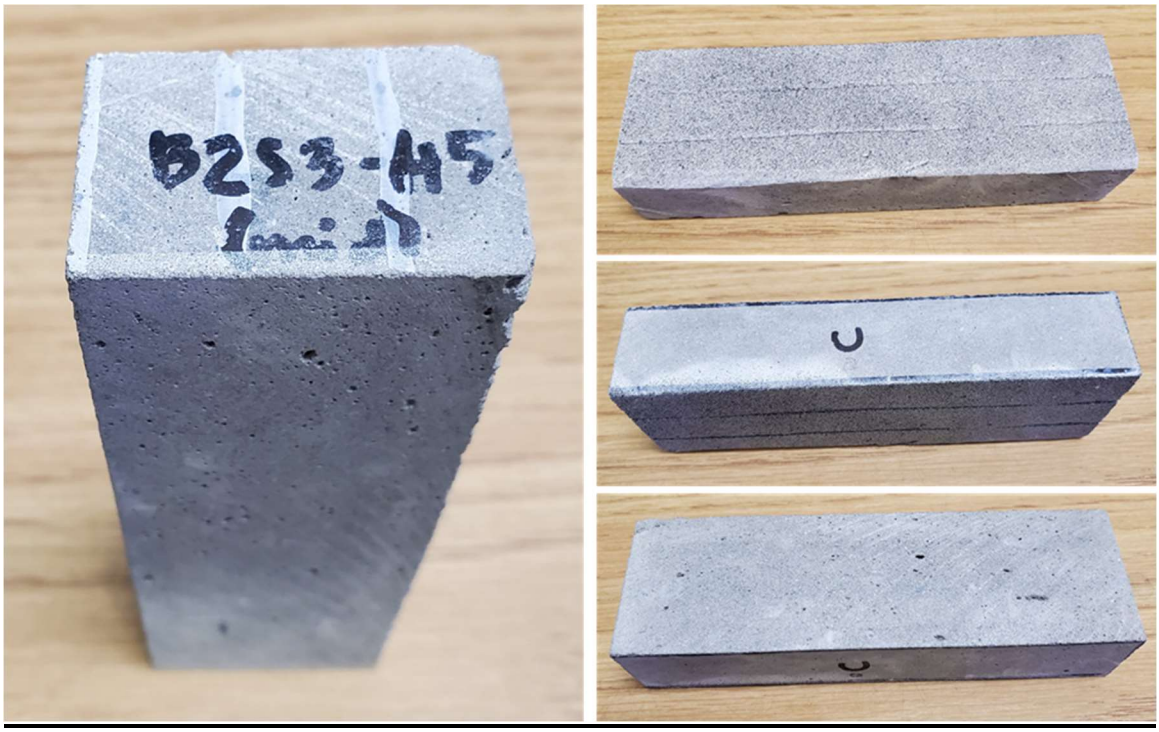

Figure C-21: B2S3-H5 prior to testing

Specimen B2S3 - H6 observations

- Orientation C
- Visual defects between layers (Figure C-22)
- Unit weight = 131.4 pcf (γ < 132 pcf)
- Failed at midspan

Figure C-22: B2S3-H6 prior to testing

Specimen B2S1 - H5 observations

- Orientation D
- Visual defects before testing (Figure C-23)
- Unit weight = 127.5.3 pcf (γ < 132 pcf)
- Diagonal failure; close to midspan though

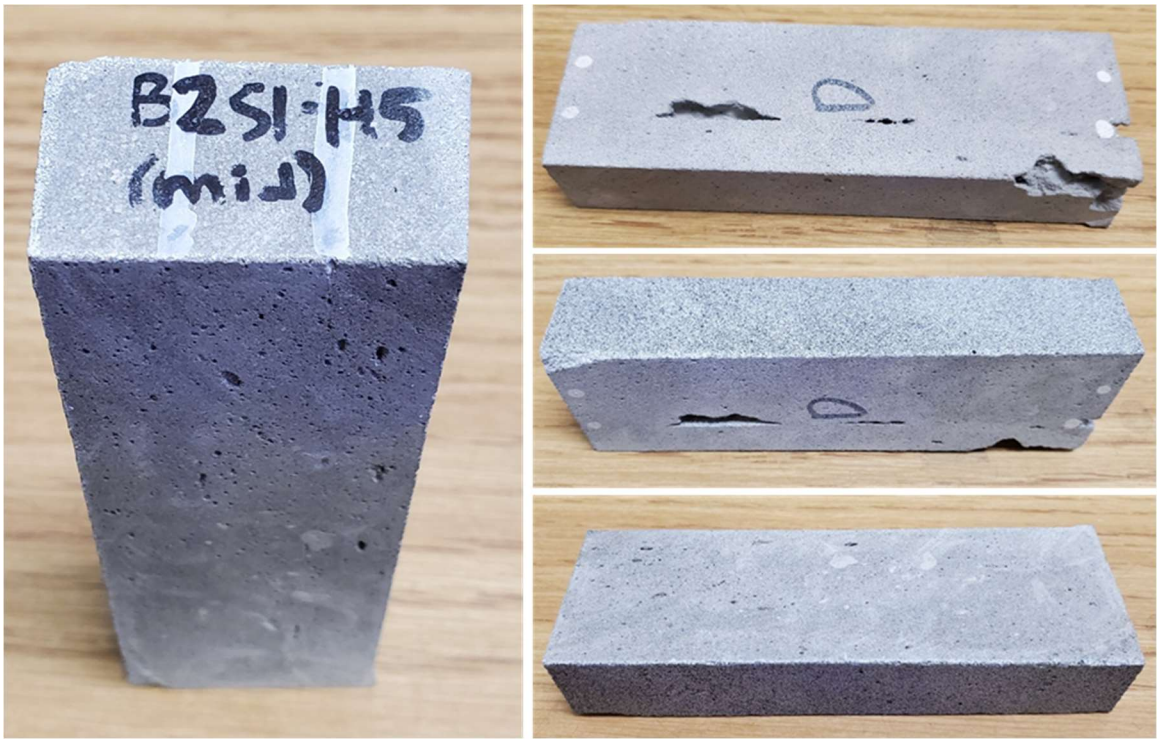

Figure C-23: B2S1-H5 prior to testing

Specimen B2S2 - H1 observations

- Orientation D
- Minor visual defects before testing; due to excess bead with overhang (Figure C-24)
- Unit weight = 134.8 pcf (γ > 132 pcf)
- Failed at midspan

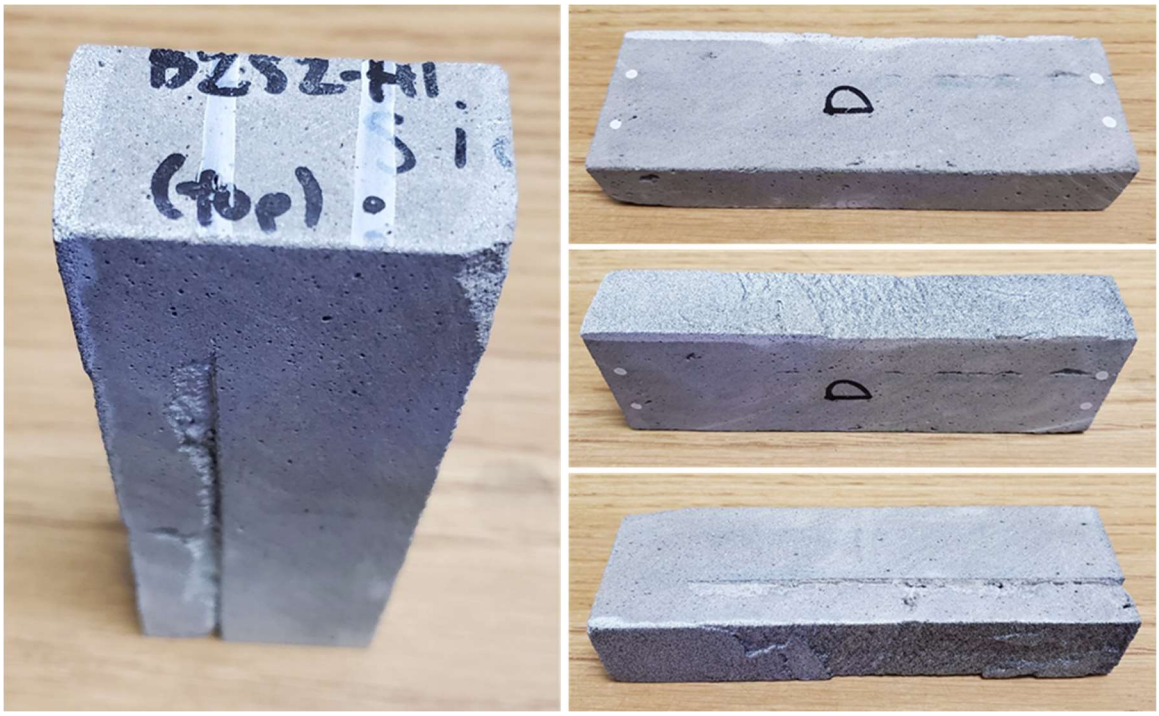

Figure C-24: B2S2-H1 prior to testing

Specimen B2S2 - H2 observations

- Orientation D
- Visual defects before testing (Figure C-25)
- Unit weight = 134.6 pcf (γ > 132 pcf)
    - Defect looks isolated to one location and near midspan. Although higher unit weight, this defect could still cause lower achieved modulus of rupture
- Failed at midspan

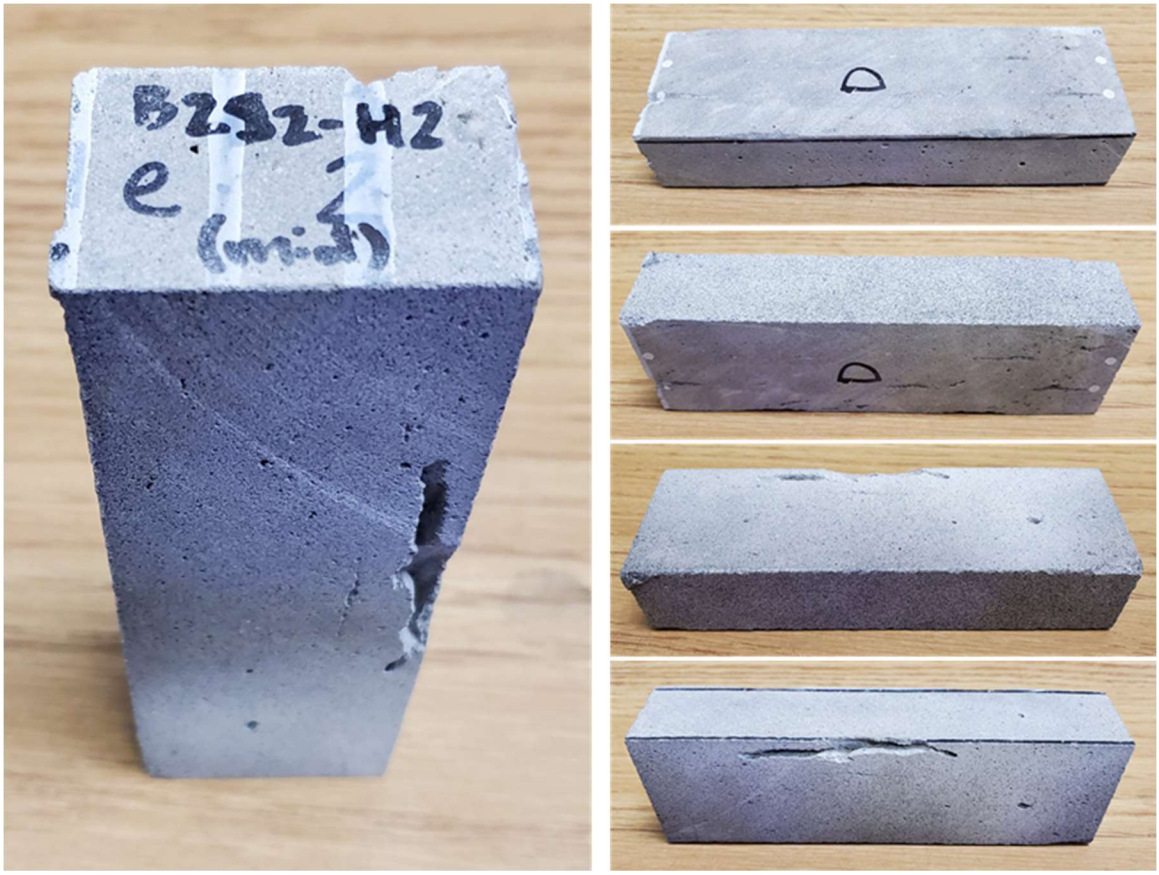

Figure C-25: B2S2-H2 prior to testing

Specimen B2S2 - H3 observations

- Orientation D
- Visual defects before testing; large defect in midspan (Figure C-26)
- Unit weight = 127.9 pcf (γ < 132 pcf)
- Failed at midspan

Figure C-26: B2S2-H3 prior to testing

Specimen B2S2 - H4 observations

- Orientation D
- Minor visual defects before testing (Figure C-27)
- Unit weight = 133.6 pcf (γ > 132 pcf)
- Failed at midspan

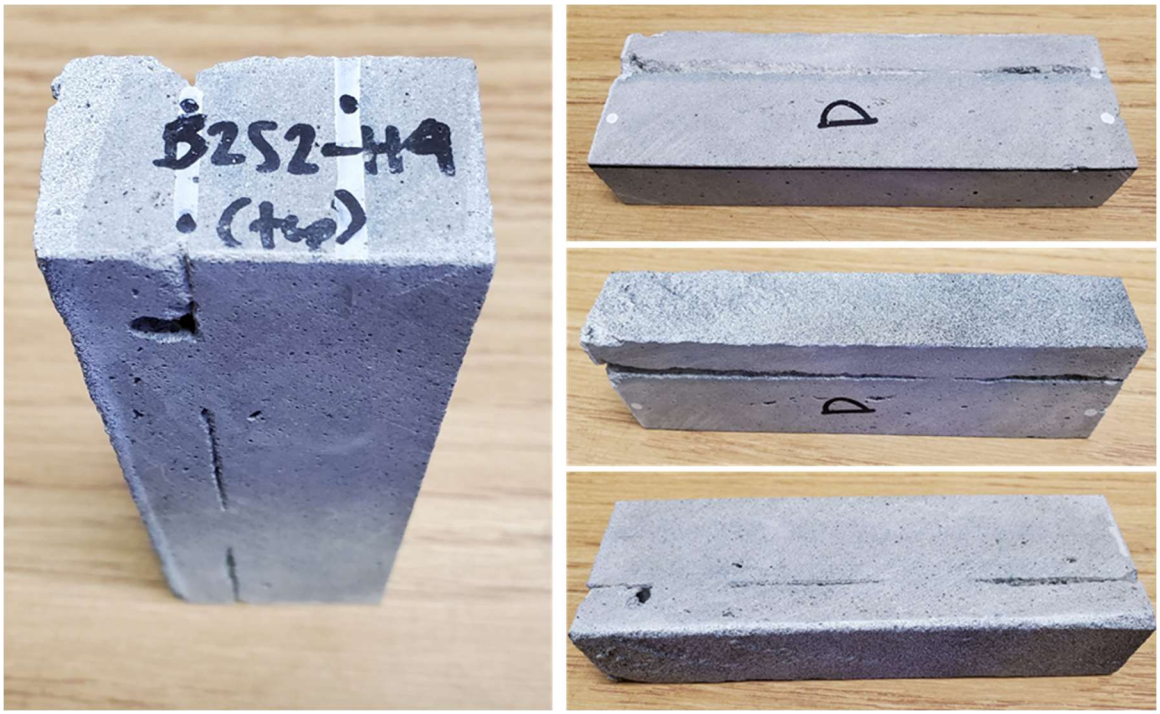

Figure C-27: B2S2-H4 prior to testing

Specimen B2S2 - H5 observations

- Orientation D
- No obvious visual defects before testing (Figure C-28)
- Unit weight = 134.4 pcf (γ > 132 pcf)
- Failed at midspan

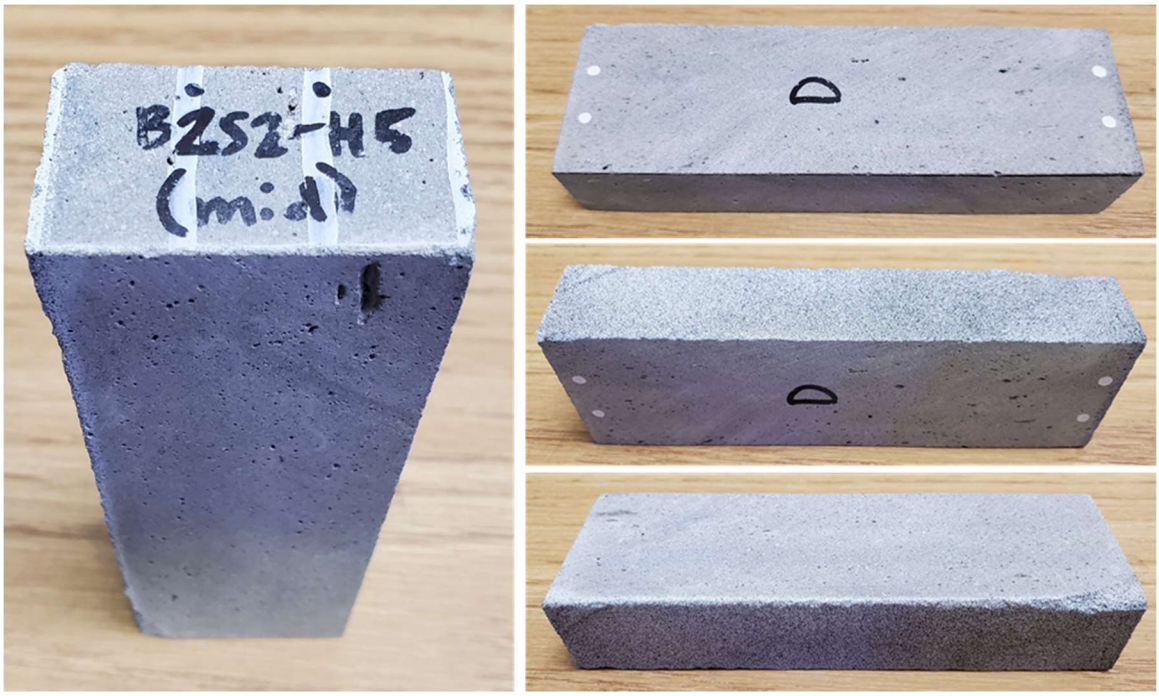

Figure C-28: B2S2-H5 prior to testing

Specimen B2S2 - H6 observations

- Orientation D
- Visual defects before testing; large defect in midspan (Figure C-29)
- Unit weight = 127.3 pcf (γ < 132 pcf)
- Failed at midspan

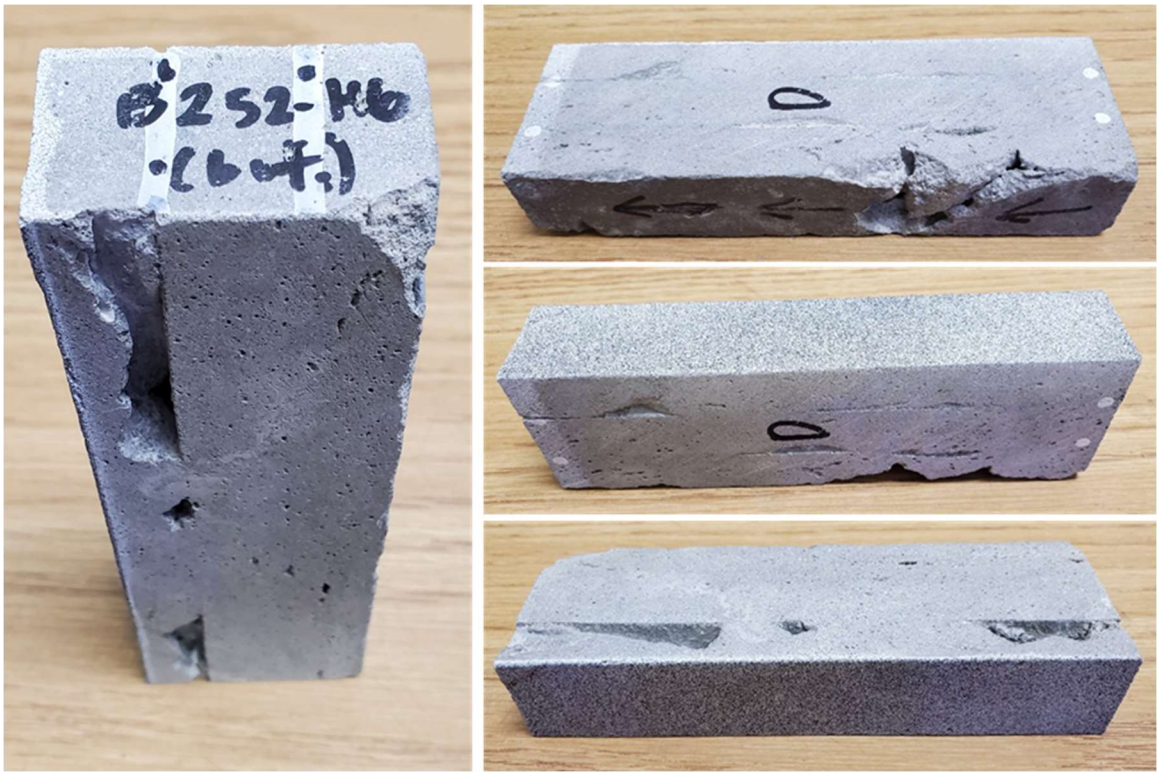

Figure C-29: B2S2-H6 prior to testing

Appendix D

The images enclosed in this appendix represent the conditions at the peak load just before failure for each respective specimen. The photos are being presented through the left camera for the DIC.

Figure D-1: B2S1-V1

Figure D-2: B2S1-V2

B2S1-V3

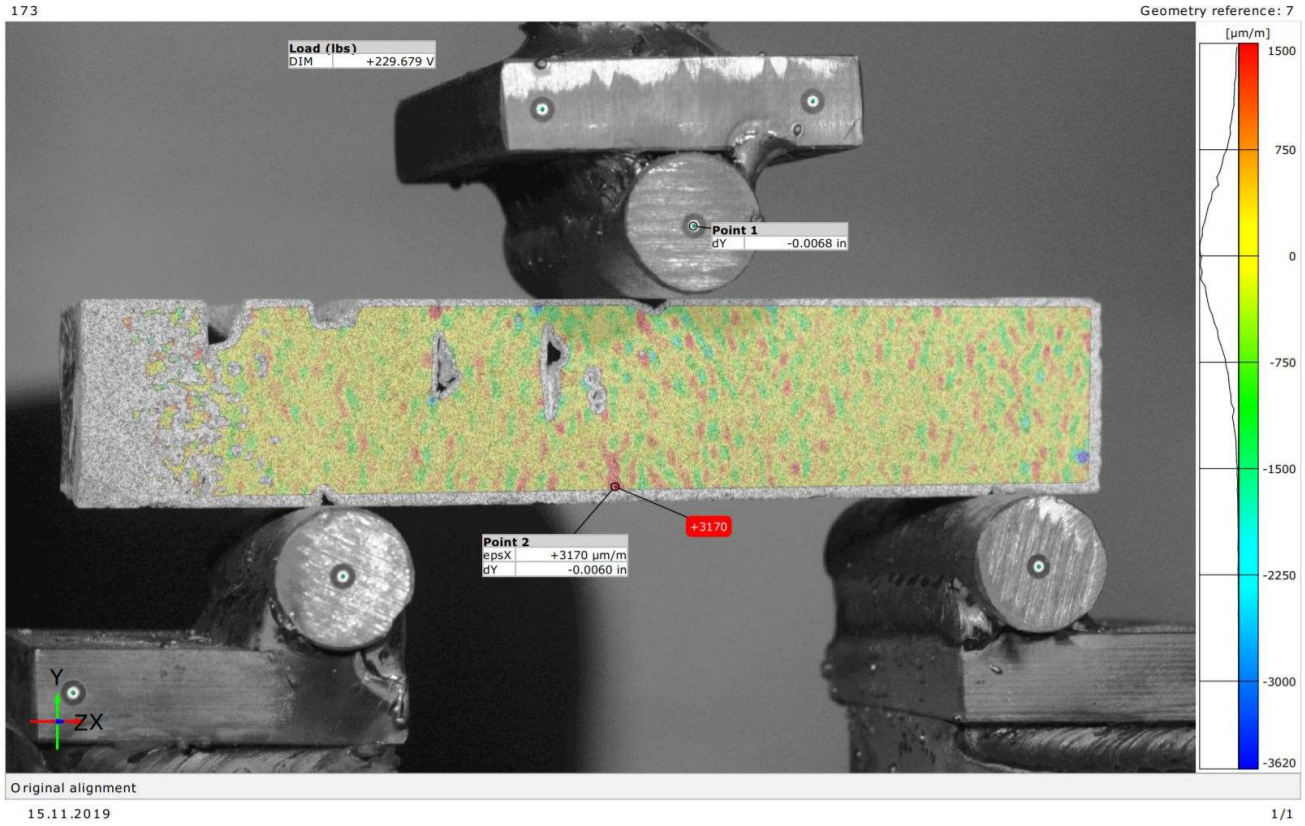

Figure D-3: B2S1-V3

Figure D-4: B2S1-V4

Figure D-5: B2S1-V5

Figure D-6: B2S2-V1

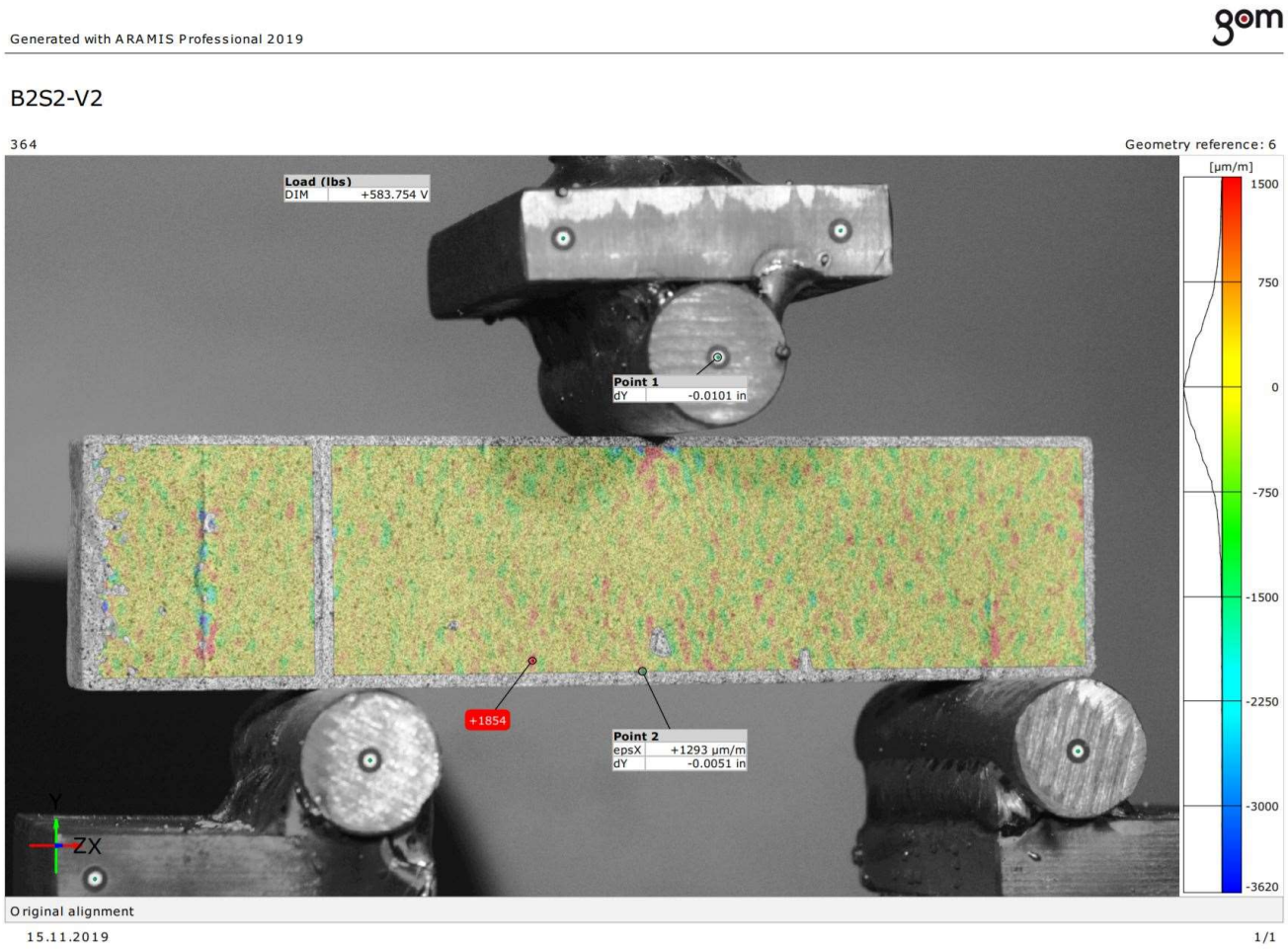

Figure D-7: B2S2-V2

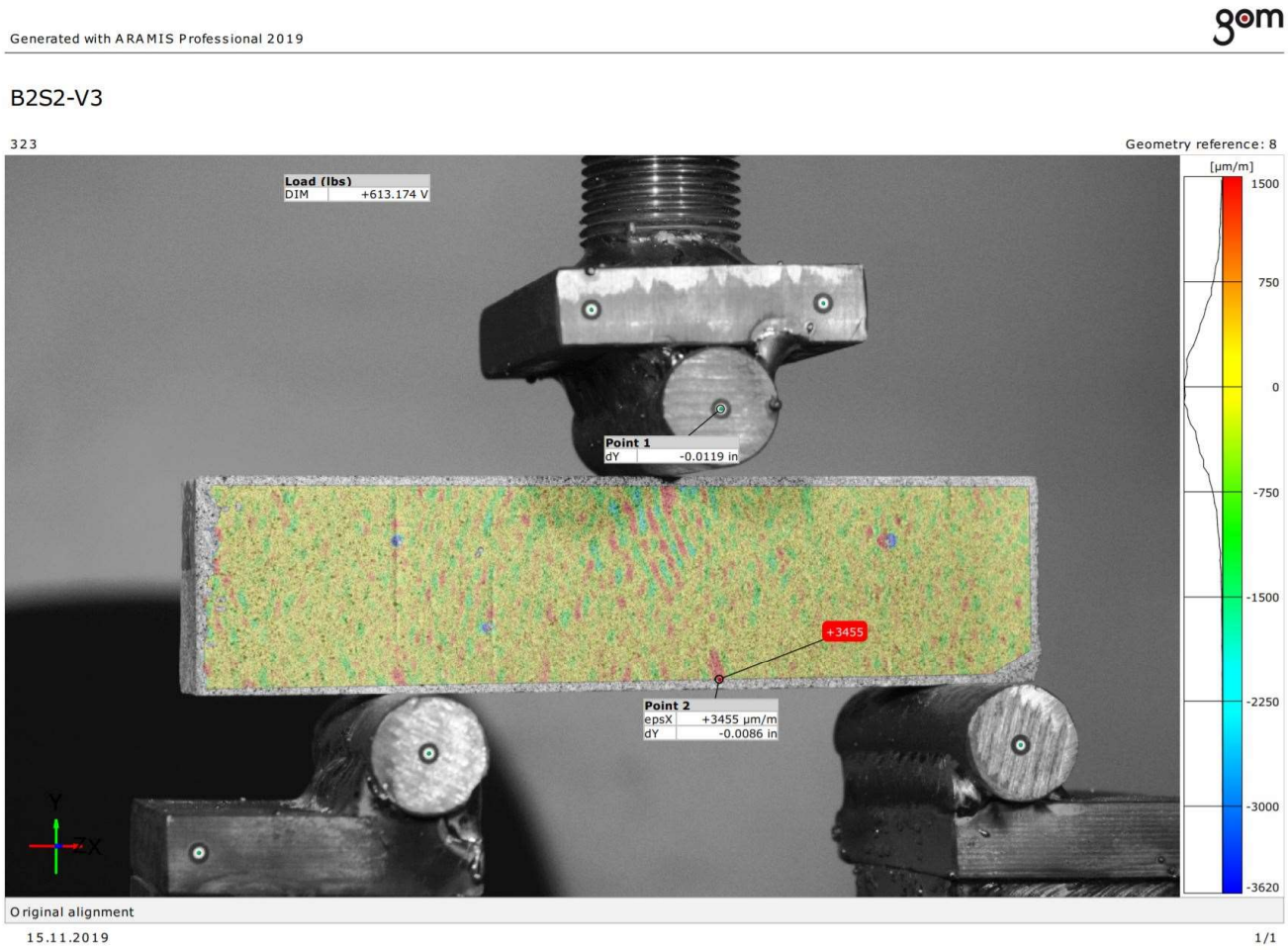

Figure D-8: B2S2-V3

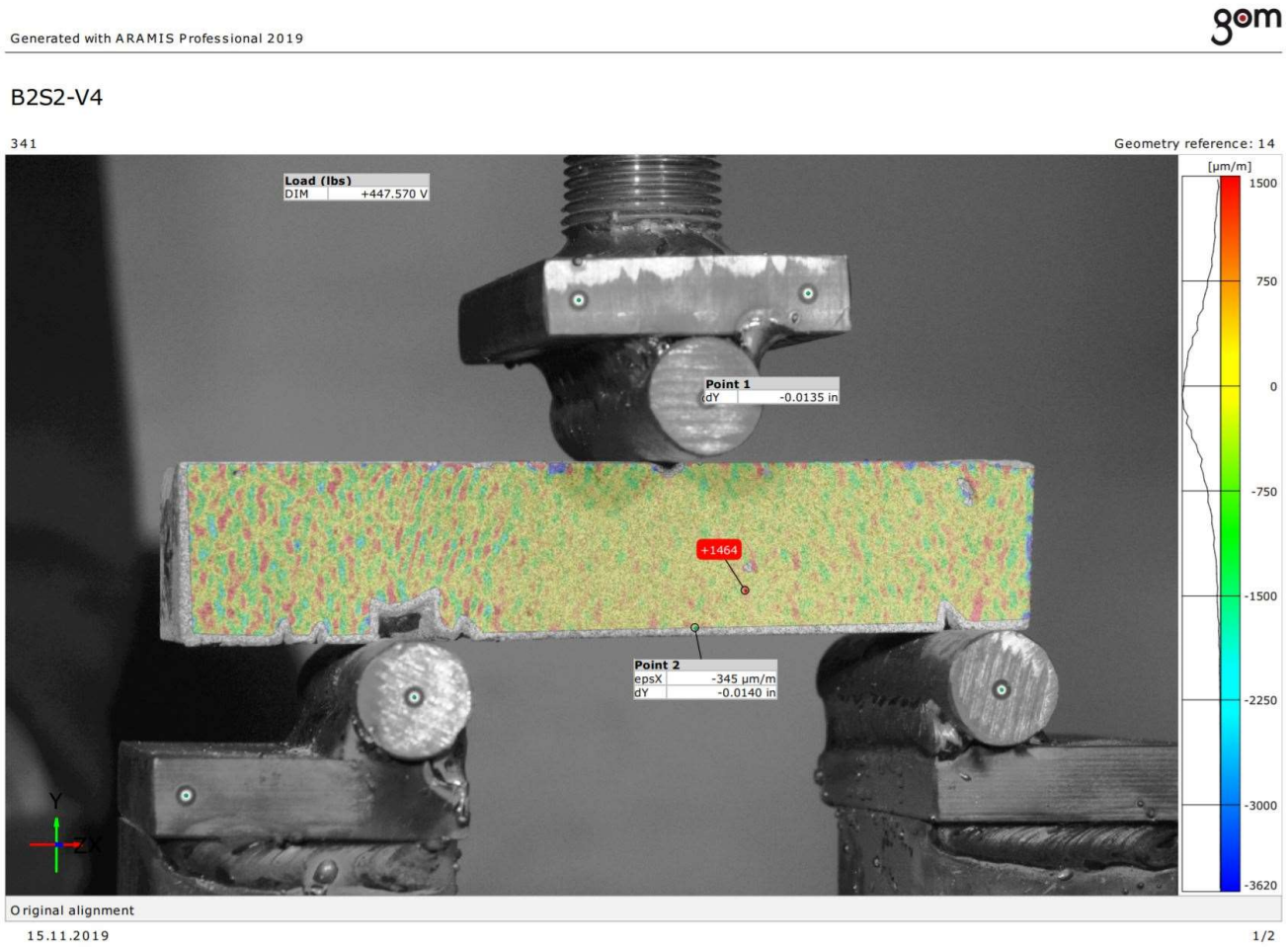

Figure D-9: B2S2-V4

Figure D-10: B2S2-V4 at failure

Figure D-11: B2S2-V5

Figure D-12: B2S2-V5 at failure

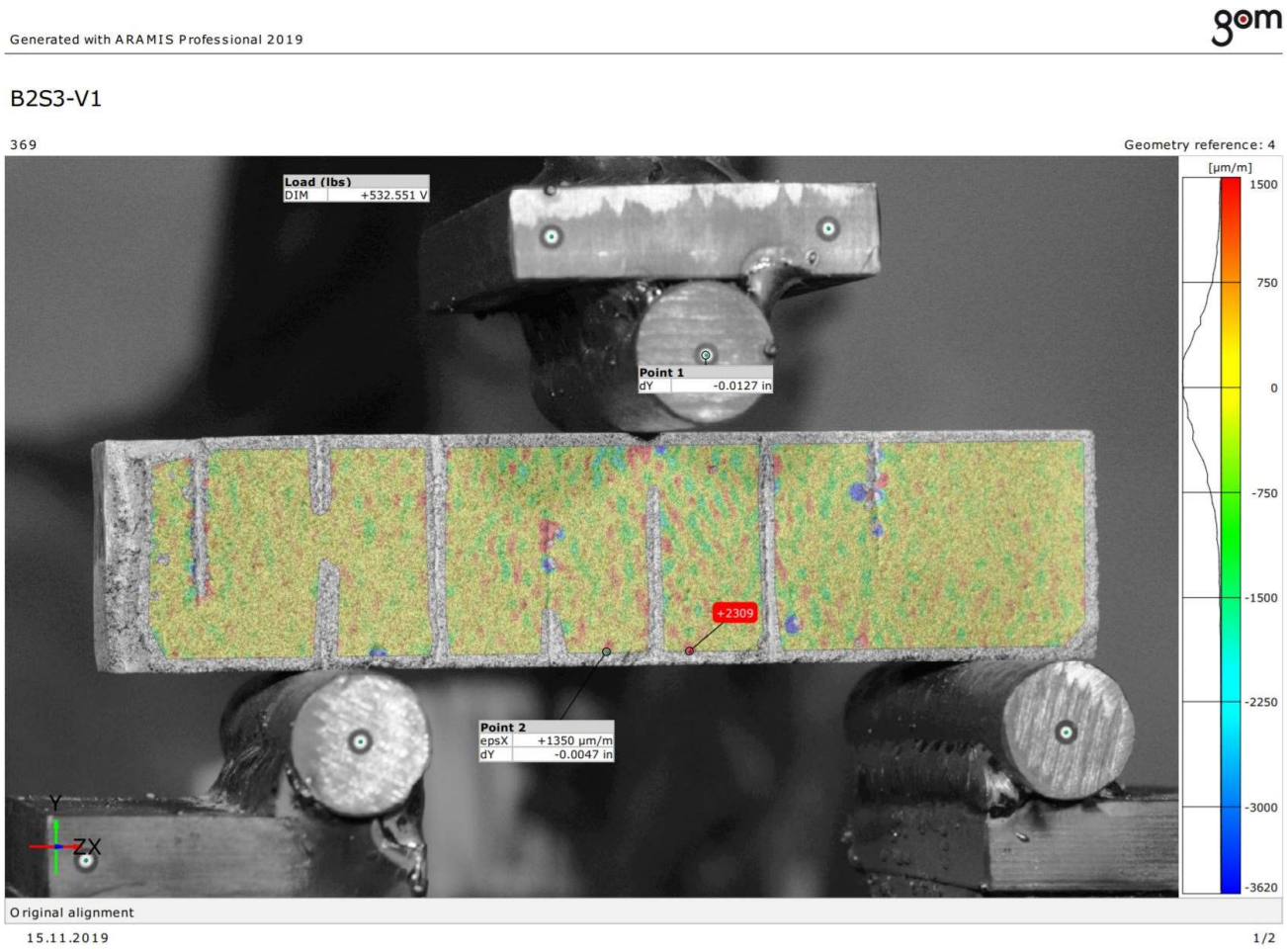

Figure D-13: B2S3-V1

Figure D-14: B2S3-V2

Figure D-15: B2S3-V3

Figure D-16: B2S3-V4

B2S1-H4

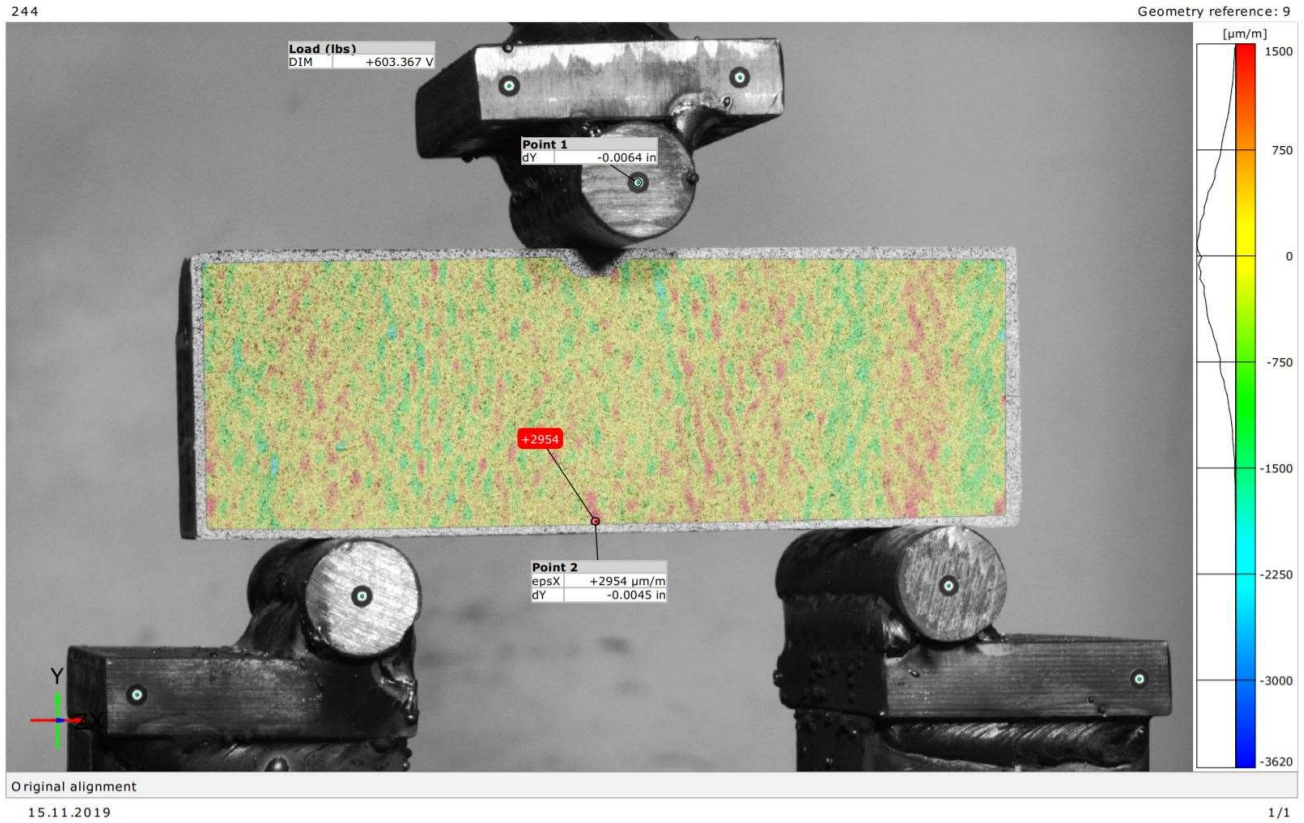

Figure D-17: B2S1-H4

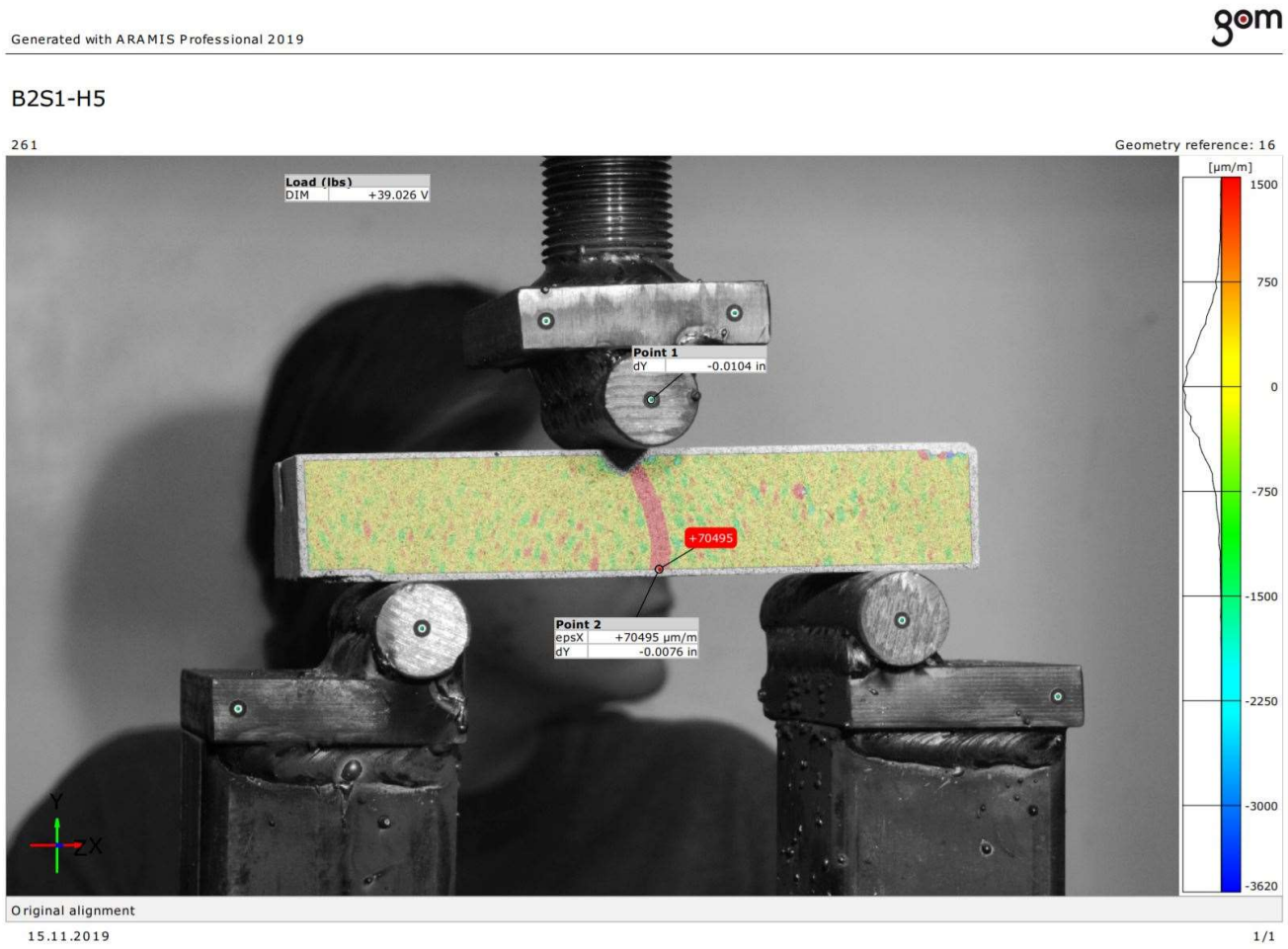

Figure D-18: B2S1-H5

Figure D-19: B2S1-H6

Figure D-20: B2S2-H1

Figure D-21: B2S2-H2

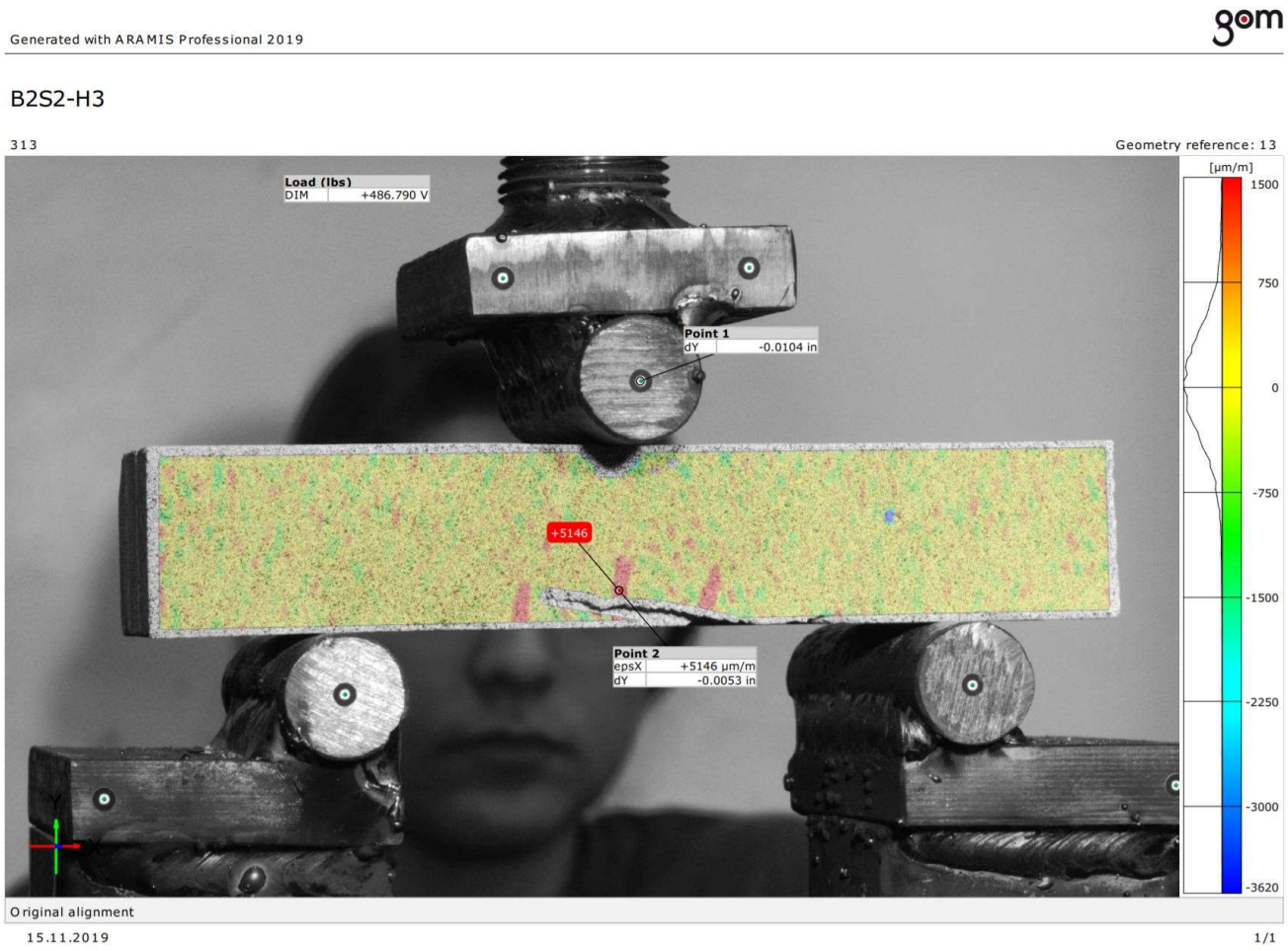

Figure D-22: B2S2-H3

Figure D-23: B2S2-H4

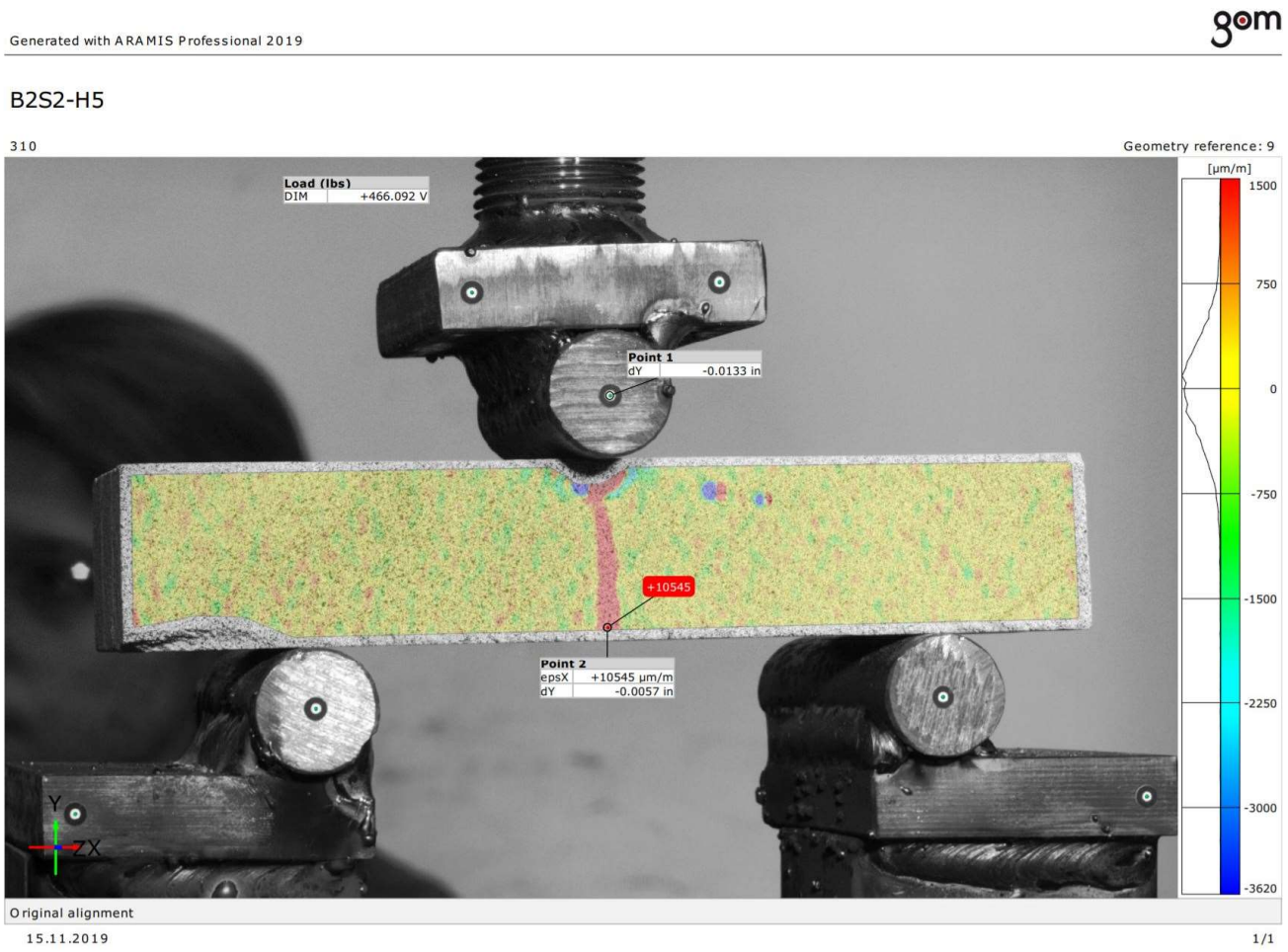

Figure D-24: B2S2-H5

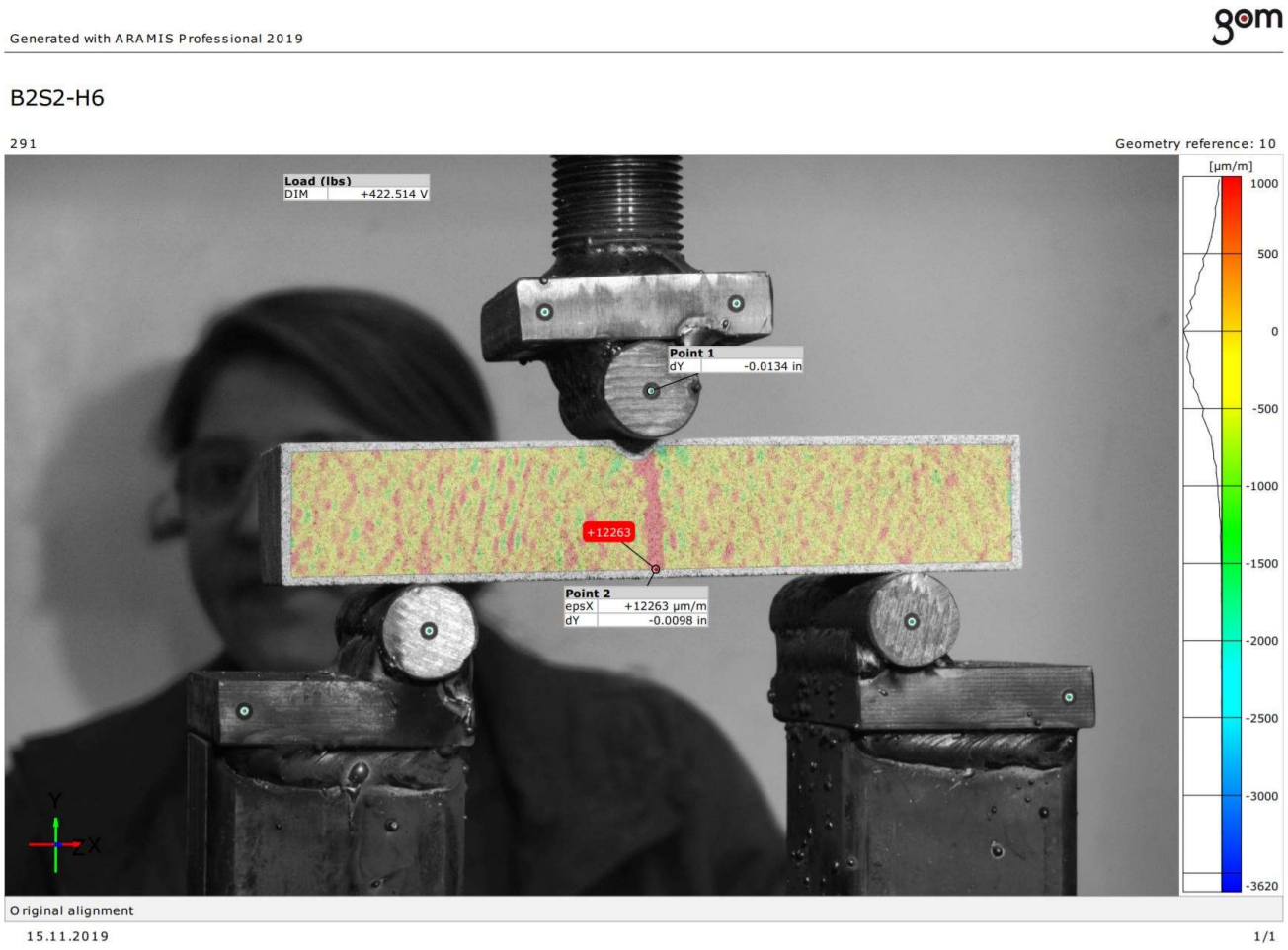

Figure D-25: B2S2-H6

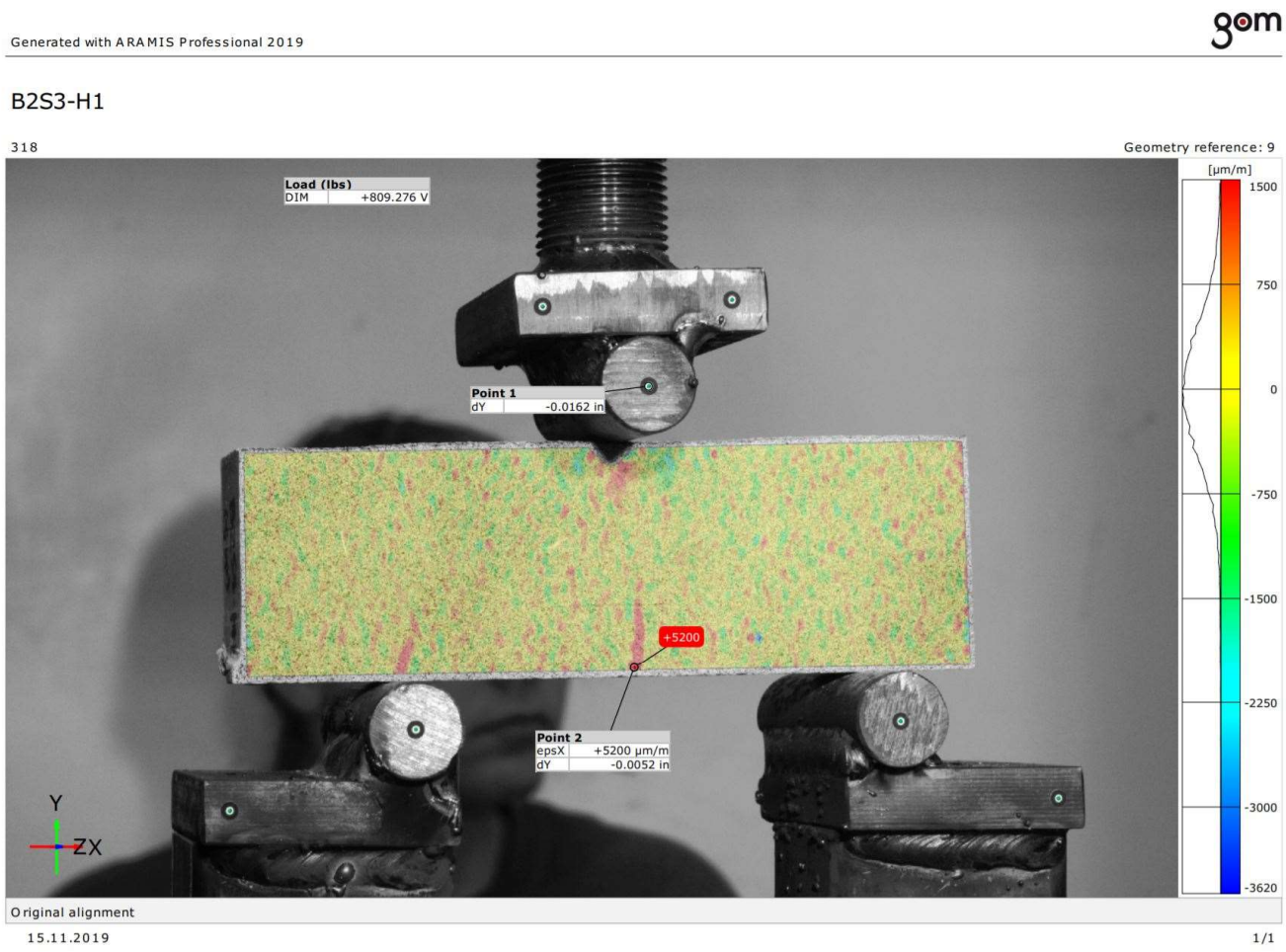

Figure D-26: B2S3-H1

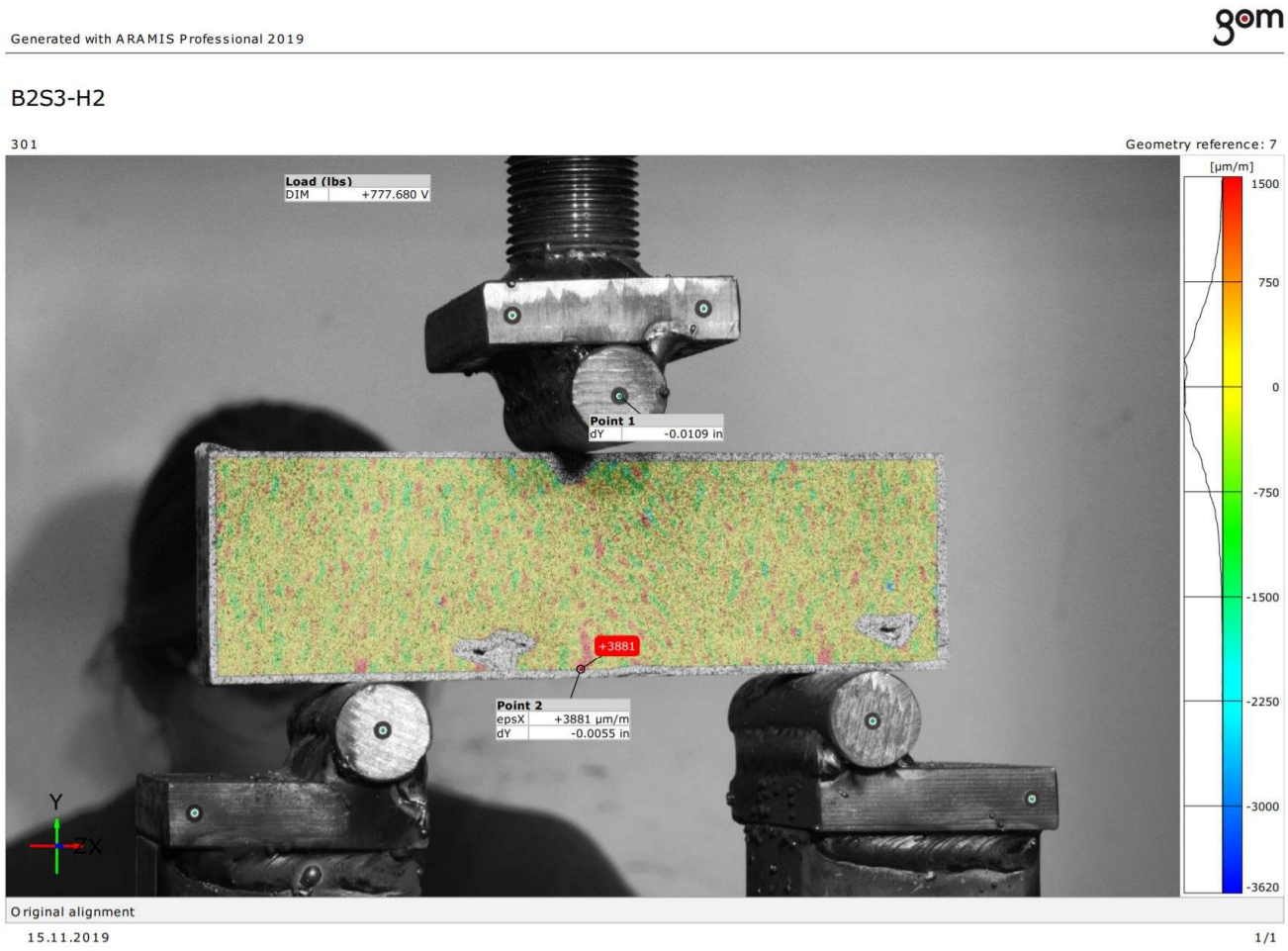

Figure D-27: B2S3-H2

Figure D-28: B2S3-H3

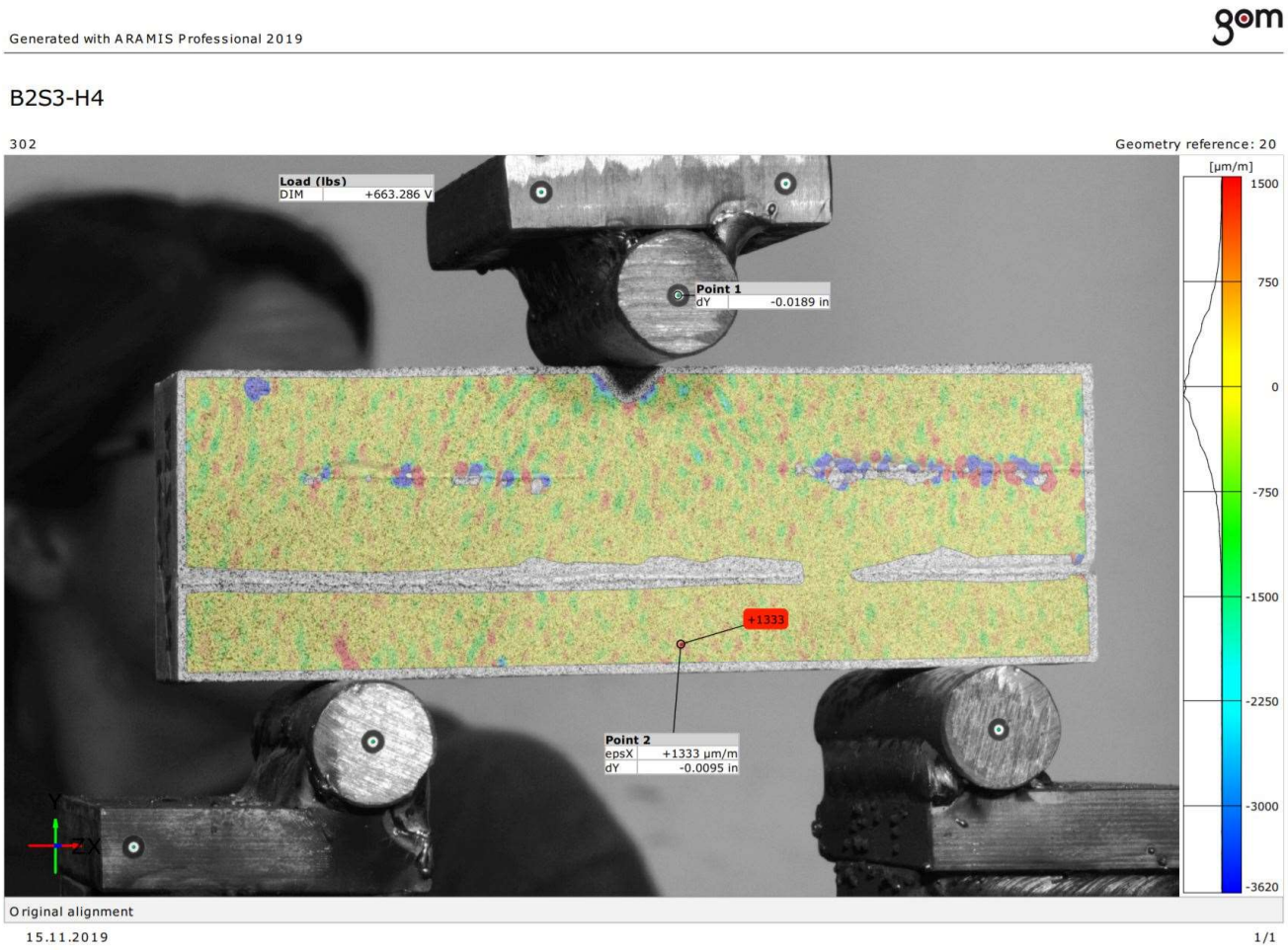

Figure D-29: B2S3-H4

Figure D-30: B2S3-H5

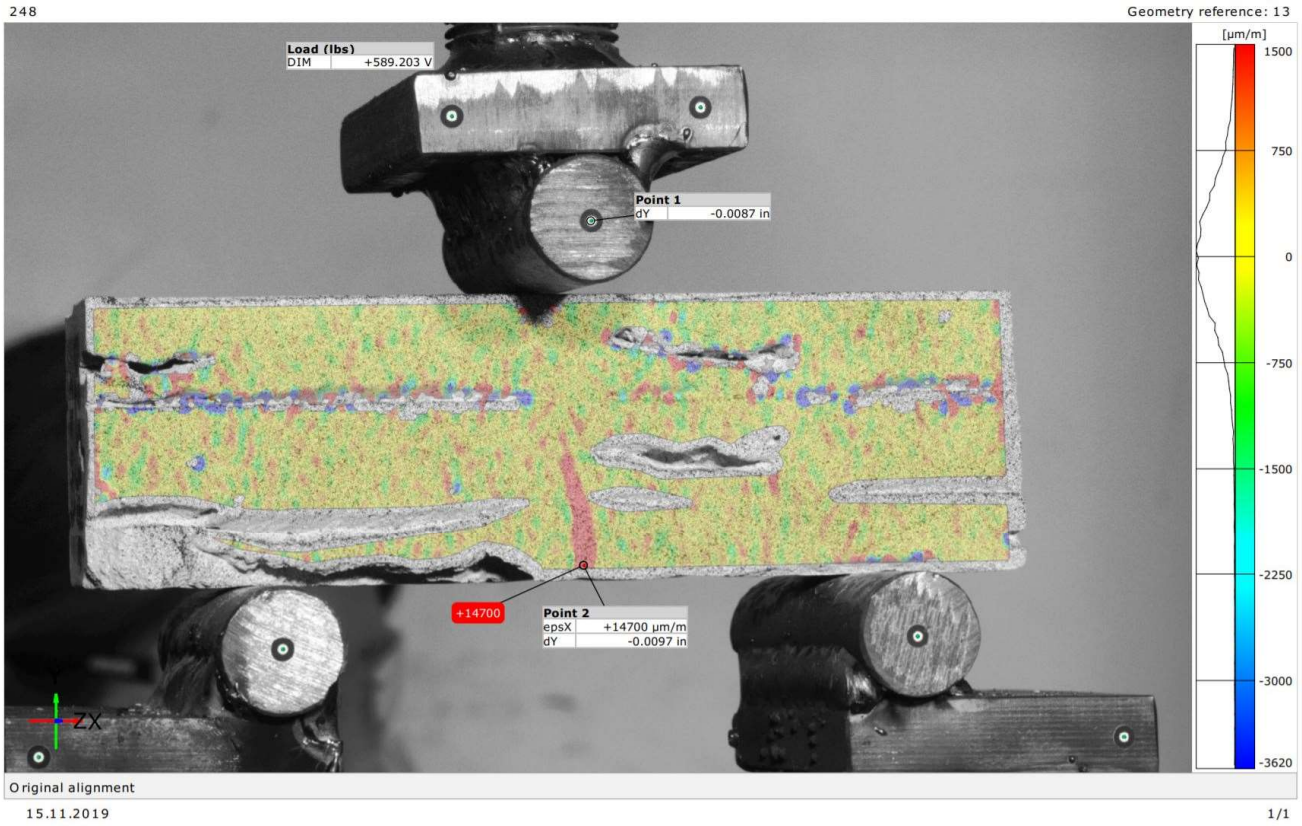

Figure D-31: B2S3-H6